AN INTELLIGENT MONITORING SYSTEM

FOR

ONLINE INDUCTION MOTOR FAULT DIAGNOSTICS

by

Peter Luong

A thesis submitted to Lakehead University
in partial fulfillment of the requirements for the
Degree of

Doctor of Philosophy in Electrical and Computer Engineering

LAKEHEAD UNIVERSITY
DEPARTMENT OF ELECTRICAL ENGINEERING
2019

ABSTRACT

For more than a century, the induction motor (IM) has been the powerhouse industrial applications such as machine tools, manufacturing facilities, pumping stations, and more recently, in electric vehicles. In addition, IMs account for approximately 40%-45% of the annual global electricity consumption. Therefore it is a critical issue to improve IM operation efficiency and reliability. In applications, unexpected failures of IMs can result in extensive production loss and increased costs. The classical preventive maintenance procedures involve periodic stoppages of IMs for inspection. If such procedures result in no faults found in the machine, as is common in practice, the unnecessary downtimes will increase operational costs significantly. This inefficiency can be addressed by condition monitoring, whereby sensors relay information about the IM in real-time, allowing for incipient IM fault diagnosis. Such a process involves three general stages:

- **Data acquisition:** A process to collect data using appropriate sensors.
- **Fault detection:** A means to process collected data, extract representative fault features, and determine the condition of the motor components.
- **Fault classification:** A means to automatically classify fault data to allow decision-making on whether or not the motor is healthy or damaged.

However, there are challenges with the above stages that are at present, barriers to the industrial adoption of condition monitoring, such as:

- Implementation limitations of traditional wired sensors in industrial plants.
- The restrictive memory and range capabilities of existing commercial wireless sensors.
- Challenges related to misleading representative fault signals and means to quantify the fault features.
- A means to adaptively classify the data without prior knowledge given to a fault classification system.

To address these challenges, the objective of this work is to develop a smart sensor-based IM fault diagnostic system targeted for real industrial applications. Specific projects pertaining to this objective include the following:

- **Smart sensor-based wireless data acquisition systems**: A smart sensor network including current and vibration sensors, which are compact, inexpensive, low-power, and longer-range wireless transmission.
- **Fault detection**: A new method to more reliably extract the representative fault features, applicable under all IM loading conditions.
- **Fault quantification**: A new means to transform fault features into a monitoring fault index.
- **Fault classification:** An evolving classification system developed to track and identify groups of fault index information for automatic IM health condition monitoring.

Results show that: (1) the wireless smart sensors are able to effectively collect data from the induction motor, (2) the fault detection and quantification techniques are able to efficiently extract representative fault features, and (3) the online diagnostic classifier diagnoses the induction motor condition with an average accuracy of 99.41%.

ACKNOWLEDGMENTS

This work acknowledge the contributions of many others. To the following faculty and staff, thank you:

- Dr. Wilson Wang (supervisor) for the overall support, funding, guidance, exposure to life-changing experiences, and teaching me the important life skills of thinking critically and perceiving deeper truths beyond what's presented on the surface.
- Dr. Will Tian (external reviewer), on taking the time to evaluate the work and ensuring it meets the standards of a doctorate degree in Canada.
- Dr. Yushi Zhou and Dr. Mohammad Uddin (thesis reviewers), for the helpful feedback on how to improve this work.
- Dr. Abdelhamid Tayebi (graduate coordinator), for patiently listening to difficulties expressed, and for providing advice, support, and encouragement to move forward.
- Dr. Carlos Christoffersen (professor) for instilling the importance of integrity regardless of outcome, and Dr. Krishnamoorthy Natarajan (professor) for instilling the importance of the practical real-world impact of all work related to engineering.
- Mr. Jason Servais (technologist) for the helpful initial advice on how to proceed with smart sensors, Mr. Bruce Misner (technologist) for the material support of electronic parts and entertaining discussions, Mr. Kailash Bhatia (technologist) for the help on machining the parts required for this work, and Morgan Ellis (technologist) for providing the strobe sensor to help further validate this work.

To the following peers and colleagues, thank you:

- Dr. Derek Li for helpful theoretical discussions related to fuzzy systems and Dr. Shazali Osman for helping me realize the importance of verifying everything.
- Angelo Menezes, Gracieth Batista, and Turker Sengoz for coding assistance, Rahul Sable for designing the sensor casing, and Manzar Mahmud for help in identifying universally-important smart sensor development considerations.

And thanks to friends, family, relatives, and my fiancée, Yue E, who one way or another, provide encouragement and motivation to contribute my utmost to society.

- *Peter Luong* (2019)

TABLE OF CONTENTS

LIST OF FIGURES

LIST OF TABLES

CHAPTER 1
Introduction

1.1 Motivation

Since their practical beginnings in 1888 [1], induction motors (IMs) have been widely used in industrial applications because they offer a balance between robust operation, relatively simple construction and high efficiency relative to other types of motors [2]. Due to such widespread usage, IMs consume approximately 40%-45% of the annual electrical energy generated globally [3,4]. Typical applications of IMs include pumps, manufacturing facilities, electric vehicles, etc. [5,6]. One example of such an IM application is as a horizontal mill pinion drive used to grind materials to a requested size [7], as shown in Fig.1.1.

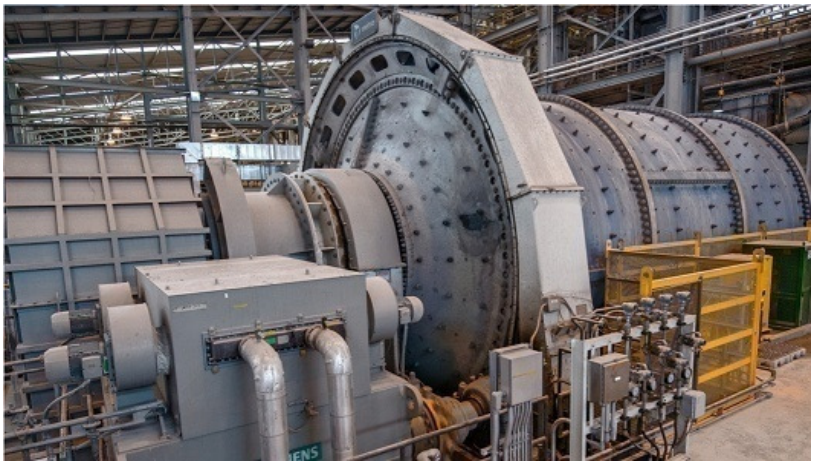

Fig.1.1. Example of IM-based mining material grinding application [7].

As IMs are critical to a wide array of industrial applications with a high demand of power consumption, there is a strong incentive to ensure that they operate efficiently and do not break down unexpectedly. In general, like other machinery systems, there are two conventional types of maintenance strategies for IMs, run-to-break and preventative maintenance [8]. Run-to-break entails running the IM until it breaks down. On the other hand, preventative maintenance entails stopping a motor at periodic intervals, opening up the motor, then manually inspecting it for possible damage and/or replacing faulty components; frequently, such inspections do not result in the discovery of any damage [8].

The unnecessary shutdowns as a consequence of the conventional preventative maintenance strategies account for an increasingly significant portion of a company's operating expenses, where maintenance costs can range from 26% to 160%[1] of the annual capital investment of an industrial plant, with costs in the order of hundreds of billions of dollars in the US alone, at an annual growth rate of 12% [9]. Conditions in other developed countries, such as Canada, are likely to follow a similar trend. To help reduce such costs, research has been conducted over decades to develop technologies and tools to detect IM faults at their incipient stage, prior to reaching more serious levels, in order to prevent performance degradation, malfunction, or even catastrophic failures of the IMs and the related driven facilities. This active monitoring process is known as condition monitoring [8], which serves as a form of predictive maintenance strategy.

Unfortunately, most of the developed fault detection techniques and monitoring tools could not be applied efficiently for IM health condition monitoring due to several reasons. Such reasons include the following specific examples:

1) In real industrial monitoring applications, hardware bottlenecks of data acquisition are related to the lack of appropriate wireless smart sensors and communication protocols.
2) In signal processing, the available IM fault detection techniques lack robustness against signal interference and noise.
3) In automatic diagnostic decision-making, the reliability of intelligent diagnostic classifiers is low due to poor adaptive capability to accommodate variable system conditions.

These imperfections will result in missed alarms (i.e., existing defects are not detected) and false alarms (i.e., triggered alarms are due to noise signals rather than real IM defects) in real-world monitoring applications [10]. Hence, this work is motivated based on addressing these challenges.

[1] 160% can represent an operating loss.

1.2 Brief Background

1.2.1 General Flow of an IM Health Condition Monitoring System

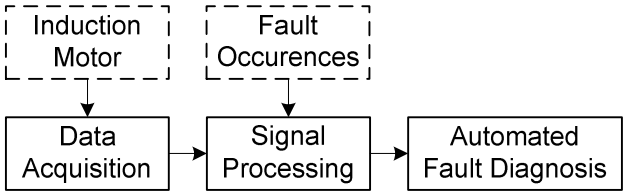

Fig. 1.2. General work flow diagram.

As illustrated in Fig. 1.2, a general online IM health condition monitoring system consists of three modules:

- **Data Acquisition**: Appropriate sensors are used to collect signals from the IM to be monitored.
- **Signal Processing**: Acquired signals are processed using appropriate signal-processing techniques to extract representative features for IM fault detection.
- **Automated Fault Diagnosis**: Representative features are classified into various categories for automated IM fault diagnosis in real time.

The development of the signal processing module also requires knowledge of the most common IM fault occurrences to prioritize subsequent research efforts.

1.3 Induction Motors

At its essence, an electric motor can be considered as a machine that converts electrical energy into mechanical energy. Though there are multiple types of electric motors such as DC motors, permanent magnet synchronous motors, and switched reluctance motors, IMs have the overall best balance between power density, efficiency, controllability, reliability, technological maturity, and cost [2]. IMs themselves on the other hand, can be further subdivided into single-phase and three-phase types [11]; within the three-phase IMs, it is again subdivided into squirrel cage and slip ring types [12]. Due to the high self-starting torque and simplicity of design compared with all other IM designs [13], the squirrel-cage IM is most commonly used for industrial applications [14]. Hence this work focuses on three-phase squirrel cage IMs.

The structure of a typical, three-phase squirrel cage IM is shown in Fig. 1.3 and Fig. 1.4.

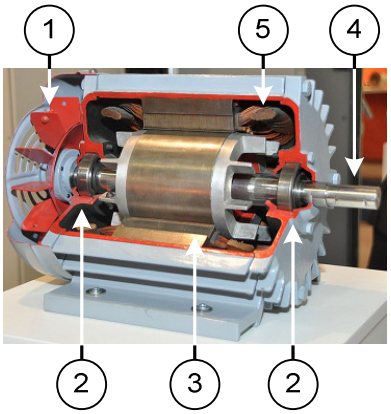

Fig. 1.3. Interior structure (compact view)[2] of a three-phase IM: (1) cooling fan, (2) bearings, (3) rotor, (4) shaft, (5) stator and stator windings.

[2] (Image Credit) S.J. de Waard, "Nederlands: Opengewerkte electromotor", *licensed under CC-BY-SA-3.0*. Nov. 2011.

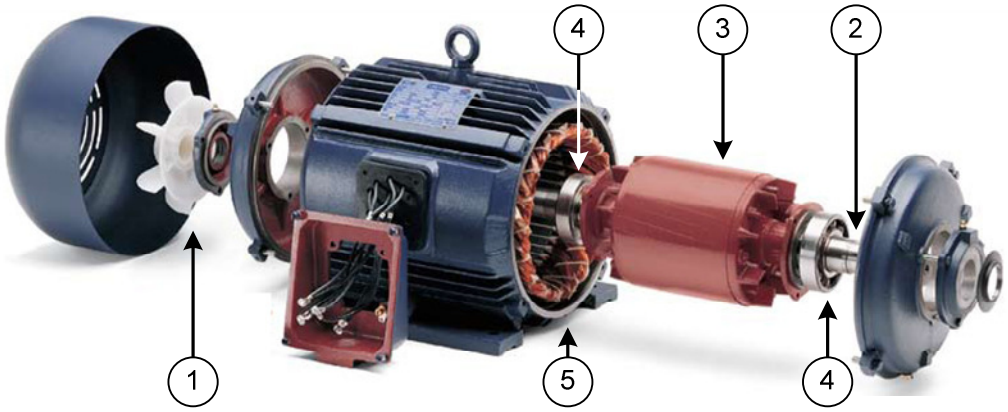

Fig. 1.4. Interior structure (expanded view)[3] of a three-phase IM: (1) cooling fan, (2) bearings, (3) rotor, (4) shaft, (5) stator and stator windings.

The stator's position is fixed. Three phases of electrical current flow into three separate sets of copper windings in the stator. These currents induce magnetic fields within the rotor bars, which attract/oppose the magnetic fields from the stator, thereby the generated electromotive force causes rotation of the shaft connected to the rotor. The shaft is supported by rolling element bearings to reduce friction, while the cooling fan is used to dissipate heat generated by friction and by the electrical current flowing through the stator windings.

In application, an IM is largely characterized by two properties: the synchronous speed and the slip. The synchronous speed, n_{SY} in revolutions-per-minute (r/min), or the synchronous frequency, f_{SY} in Hertz (Hz), is the speed at which the stator-current-induced magnetic field rotates, defined as:

$$n_{SY} = \frac{2 f_L 60}{p} \quad , \quad f_{SY} = \frac{2 f_L}{p} \tag{1.1}$$

where f_L is the electrical line frequency in Hz and p is the number of poles per line phase that exists in the stator teeth of the IM. Fig. 1.5. illustrates an example of a 3-phase, 2-pole IM.

[3] (Image Credit) J. Murphy, "What's the difference between AC induction, permanent magnet, and servomotor technologies?," [Online]. Available: http://machinedesign.com. Apr. 2012.

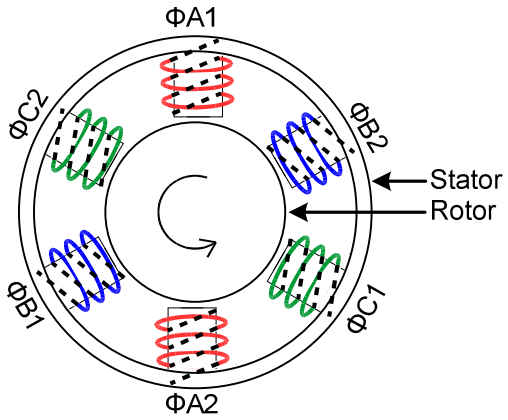

Fig. 1.5. Example of a 3-phase, 2-pole induction motor, where "ΦA, ΦB, ΦC" denotes each of the three phases; "1" and "2" denote the respective start and end of the stator winding.

As the rotor can never reach the synchronous speed or synchronous frequency, the slip of an IM, s, is calculated as:

$$s = \frac{n_{SY} - n_R}{n_{SY}} = \frac{f_{SY} - f_R}{f_{SY}} \tag{1.2}$$

where n_R is the speed of the rotor in r/min and f_R is the frequency of the rotor in Hz.

1.4 Data Acquisition System

To date, the majority of published condition monitoring works rely on wired laboratory data acquisition (DAQ) systems, as illustrated in Fig. 1.6.

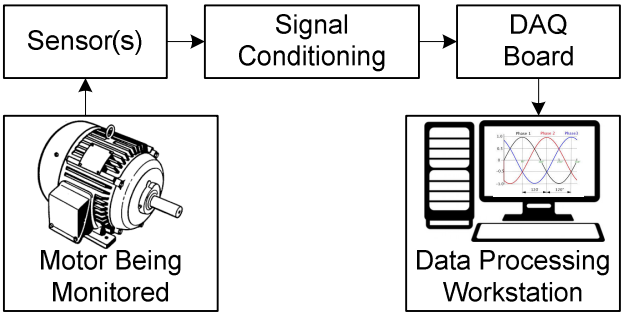

Fig. 1.6. A traditional wired laboratory DAQ system.

A traditional DAQ system consists of the following:

- Sensors
- Signal conditioning
- DAQ board
- Workstation

Sensor types depend on signal information required for monitoring; commonly-used signals for IM monitoring include electrical current and vibration signals. The signal conditioning provides functionalities such as the sensors' required excitation voltages and/or currents, amplification, anti-aliasing filters, and noise reduction over the transmission line. The DAQ board is used to process data through an analog-to-digital converter (ADC), and finally sends the digitized data to the workstation (i.e., one or more computers) for advanced signal processing and diagnosis of the motor conditions. For industrial implementation, such a DAQ setup requires long sensor cables, as well as additional power sources for the intermediary signal conditioning circuits. Such a setup will generate issues related to space and safety, which could seriously limit the application of condition monitoring in most industrial plants for IMs and other general machinery systems.

To solve these challenges associated with traditional DAQ systems, a solution could be the use of wireless smart sensors. A smart sensor is a system that integrates the sensor(s), signal conditioning, and DAQ as one unit, with the related functions coordinated by a microcontroller. Fig. 1.7 shows a wireless-transceivers-based DAQ for IM fault detection.

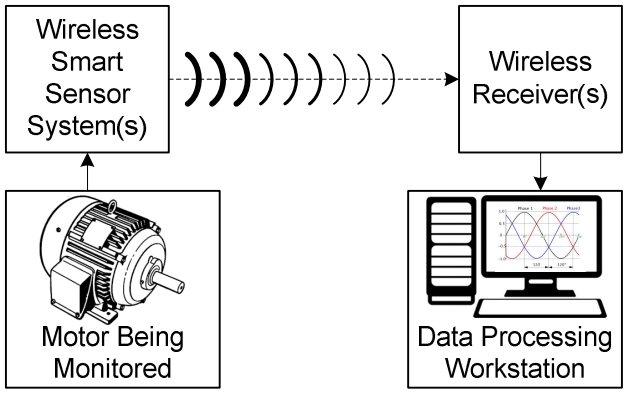

Fig. 1.7. Wireless smart sensor system(s) for IM fault detection.

1.4.1 Smart Sensor-based Data Acquisition Systems

A smart sensor is characterized by the combination of the sensing unit, an ADC controlled by a microcontroller unit (MCU), and communications interface in one housing [15], where due to this integrated nature of components, costs can be significantly reduced

compared to traditional DAQ hardware. A modular representation of a smart sensor is shown in Fig. 1.8.

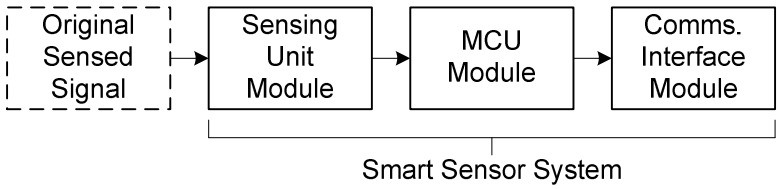

Fig. 1.8. Generic block diagram of a smart sensor system.

Such modules are briefly described as follows:

- **Sensing Unit:** Consists of a sensing transducer, amplifier, anti-aliasing low-pass-filter, and ADC. The process first involves the original signal being converted to a voltage via the transducer. This voltage is then appropriately amplified and low-pass-filtered before being sampled and digitized with an ADC.
- **MCU Module:** Controls the operations of the ADC sampling and stores the digitized information from the ADC in memory.
- **Communications Interface:** Enables the MCU to transfer its information to and from an outside system, such as a receiver connected to another computing device. Such an interface enables communication by using an appropriate wireless protocol.

1.4.2 Current Development in Smart Sensor-based IM Monitoring

While the underlying technology for smart sensors has existed for years, it has seen limited application with respect to the monitoring of IMs due to the added complexity associated with developing such devices.

Cabanas *et. al* in [5] demonstrated a wireless, low-power, smart sensing system to detect broken rotor bar faults, though that system's memory limitations can be problematic if longer sampling times are required.

Cardoso *et. al* in [16] developed a smart sensing unit, with a low-power consumption of 1.6mA / 3.3V, which further demonstrated the feasibility of a low-power DAQ system.

Philipp *et. al* in [17] designed a wireless smart sensor network that can be employed to capture data from multiple IMs, as depicted in Fig. 1.9.

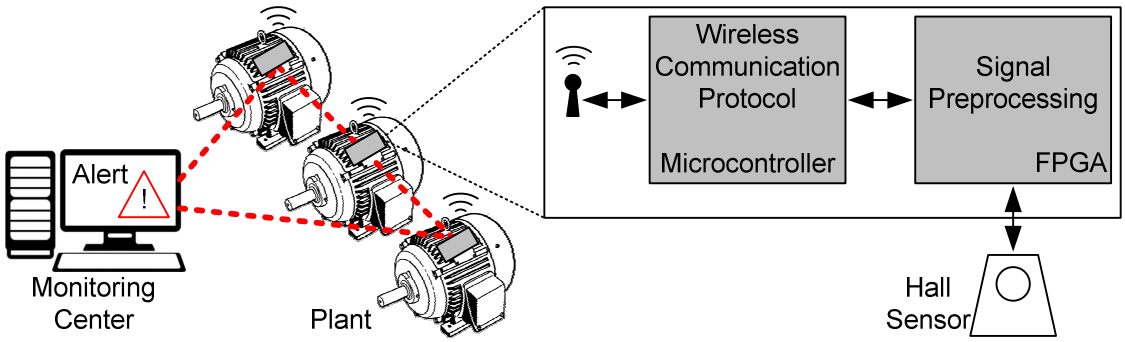

Fig. 1.9. Wireless network of smart sensors [17].

Esfahani *et. al* in [18] demonstrated that the vibration and current transducers, as well as the wireless transceivers, were available at the low power required for smart sensor implementation, and could therefore be used for IM smart DAQ.

Hedge *et. al* in [19] validated smart-sensor-compatible vibration transducers with conventional DAQ equipment, which could further prove the transducer's efficacy for the smart DAQ in IM fault detection.

The limitations of the aforementioned development include limited memory to store data, lack of published design considerations in terms of appropriate DAQ bandwidth, power efficiency, signal-to-noise ratio, and reliable wireless communications. All of these factors are essential to wireless smart sensor-based IM monitoring.

1.5 IM Fault Occurrences

Table I summarizes the most common IM fault occurrences from surveys conducted.

Table I. Type of IM faults and reported frequency of occurrences (%).

Published Survey	Type of Fault				No. of Samples
	Bearing	Stator	Rotor	Other	
Paper [20]	41%	37%	8%	14%	24,914
Paper [21]	41%	36%	8%	15%	1,474
Paper [22]	42%	13%	8%	37%	419
Paper [23]	52%	25%	6%	17%	250

As the bearing, stator, and rotor fault conditions consist of about 80% of IM fault occurrences, the majority of IM condition monitoring should be focused on reliable diagnosis of these faults in their incipient stages so as to prevent IM performance degradation and improve its operational efficiency.

Despite the data from the surveys, however, the stator winding's insulation material design has undergone significant improvements in past decades [24]. In contrast, there have been relatively fewer advancements to the cage rotor design [25]; therefore, rotor-related faults now account for a larger percentage of total IM failures [26] with approximately half due to broken rotor bars [9]. Hence, the focus of this work will be on rotor bar faults.

1.5.1 Rotor Bars and Faults Overview

A typical IM rotor is comprised of three parts: rotor end caps, laminations, and rotor bars. Fig. 1.10 shows the exterior and interior structure of an IM rotor.

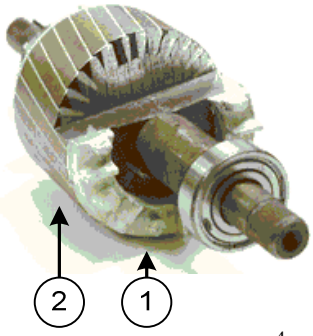

(a) Exterior structure.[4]

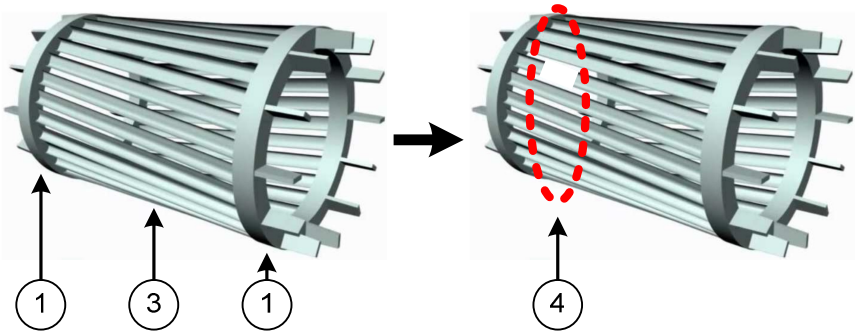

(b) Interior structure.[5]

Fig. 1.10. A typical IM rotor: (a) exterior structure, (b) interior structure; (1) rotor end cap(s), (2) laminations, (3) rotor Bars, (4) broken rotor bar.

The rotor bars are connected by end caps. The current in the rotor bars, induced by the magnetic fields of the stator, will create the opposing magnetic fields necessary for movement. Multiple thin plates of electrically-isolated laminations are combined as one piece to reduce the eddy current losses in the rotor bars.

A rotor bar breakage is illustrated in Fig. 1.10(b). The causes of rotor bar faults include excessive dynamic load stress, electromagnetic stress due to an imbalance in the stator's magnetic field, corrosion due to chemicals in the environment [27], etc. The

---

[4] (Image Credit) "Electrical problem-solving training course," Technical Training Solutions. [Online]. Available: https://www.technicaltrainingsolutions.co.uk/courses/electrical-problem-solving-course.html. 2018.

[5] (Image Credit) "How does an Induction Motor Work?", Learn Engineering. [Online]. Available: http://www.learnengineering.org/2013/08/three-phase-induction-motor-working-squirrel-cage.html. 2011.

consequences of an untreated rotor bar defect include increased vibration and noise, deterioration of the motor output efficiency, and ultimately, the progression to IM failure [28].

1.6 Signal Processing for IM Rotor Bar Fault Detection

Signal processing is a process of extracting representative features from the collected signal using an appropriate DAQ system for IM fault detection. As varying IM operating conditions can produce ambiguous results [6], reliable IM fault feature extraction remains an open research problem in signal processing.

1.6.1 Sensing Methods

Though several types of signals can be measured and used for rotor bar defect detection, the most intensive research efforts have been focused on the analysis of current and vibration signals, with alternatives focusing on thermal and acoustic-based monitoring.

- **Thermal and acoustic signals:** Although thermal and acoustic signals are simple to measure, thermal signals would be impractical in accurately detecting the minute changes in temperature that an IM fault condition may represent [29]. Acoustic signals would require placement of acoustic sensors at proper distances, locations, and orientations, with specialized uni-directional microphones to prevent noise contamination [30]. If such stringent requirements are not met, then acoustic signals can have a low signal-to-noise ratio (SNR).
- **Vibration signals:** Vibration signals have a high SNR [31], but vibration sensors are often expensive and have high mounting-related requirements for installation, which can be difficult to achieve considering the specific cylindrical structure of IMs [32]. In addition, a broken rotor bar defect in its incipient stage may not generate strong signal modulation and clear representative fault features from vibration signals [33].
- **Current signals:** Current sensors have an inherent advantage of being non-invasive to the IM, and can be easily installed due to the availability of step-down current transformers in most industrial plants. Its primary drawback, however, is a

lower SNR relative to vibration signals, increasing the challenge of detecting certain types of IM faults, such as bearing defects [32,34].

Weighing the aforementioned factors in favour of practicality of implementation, greater consideration will be placed on current-based signal-processing techniques, also known as motor current signature analysis (MCSA) [35].

1.6.2 MCSA-based Signal Processing Methods

Several MCSA-based techniques have been proposed in literature for rotor bar fault detection, based on spectral feature analysis of sidebands to the main line frequency component [36,37,38]. However, similar sidebands can also occur in spectral maps of healthy motors due to rotor asymmetries caused by manufacturing/assembly tolerances, connection coupling, or speed oscillation of connected gearboxes [5,6].

The sideband issue has been addressed by instead monitoring the zero-crossing moments of the time domain signal, using small differences in these time durations to indicate the rotor bar fault, in time measurements of hundreds of microseconds [5]. However, such a setup requires the installation of search coils, which may not be suitable in real applications; furthermore a very high sampling frequency of the DAQ system is challenging to achieve under the hardware limitations of a wireless smart sensor DAQ system.

It is identified in [6] that some higher frequencies of the current, based on magnetomotive force space harmonics, are less susceptible to the feedback influences such as gearbox-induced oscillations. However, the above fault detection methods are based on the IM slip that is usually measured using a speed encoder attached to the IM shaft [36]. Such means to measure slip may be problematic in real IM applications, where an encoder could be difficult to implement on a standard motor.

Time-frequency and homogeneity analysis of the startup transient is also used as a means to detect rotor bar faults [39,40]. The success rate of these startup-based methods depends on whether the transient is long enough; such an approach is difficult to apply to soft-started inverter or variable-frequency-drive (VFD)-fed motors [6]. In addition, startup-based methods are not suitable for the monitoring of motors that have already started up and are in actively-running operation.

1.7 Automated Online Health Condition Monitoring for IM Fault Diagnosis

In general, for IM fault detection, a different signal processing technique has its own strengths and limitations; it could be efficient only under specific IM fault type and operating conditions. Correspondingly, an approach to improve accuracy in IM health condition monitoring could be based on the analysis of results from several fault detection techniques. The integration of these features could be undertaken by the use of analytical methods or soft-computing tools. In general an accurate analytical model is difficult to derive from complex IM systems connected with the driven machinery systems. In this work, a soft-computing tool will be applied to integrate the strengths of multiple fault detection techniques for automatic fault diagnosis. Such a process will be conducted online, where a real-time diagnosis can be made based on new data without requiring the storage of large databases of past data.

Common problems with diagnostic systems are false alarms (system indicates a fault when there is no fault) and missed alarms (system indicates no fault when there is a fault) [8]. One of the objectives of this work is to mitigate these false/missed alarm problems.

1.7.1 Soft-computing-based IM Fault Diagnostic Classifier

In the context of automatic IM condition monitoring, a soft-computing system can employ multiple features for real-time diagnostic classification. The inputs to such a classifier will be monitoring indices that are numerical characteristic values derived from features extracted by signal processing, and a diagnostic output of the IM's conditions, as illustrated in Fig. 1.11(a).

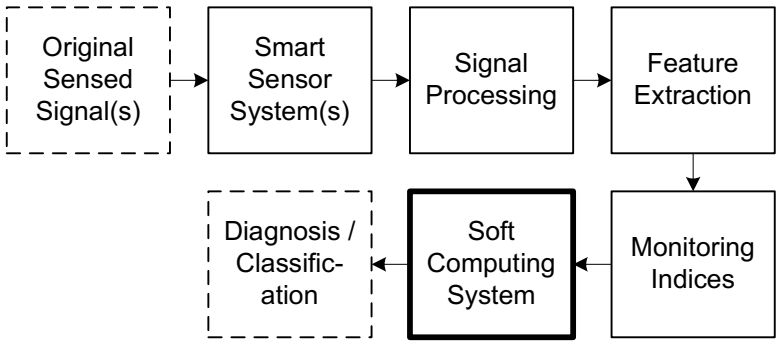

(a) Block diagram.

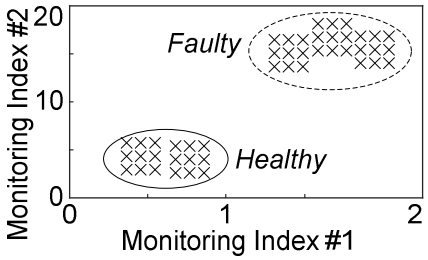

(b) Example classification.

Fig. 1.11. Soft computing system block diagram with example classification.

Classification is a means to classify patterns into different group categories. This grouping in turn corresponds to different IM health conditions for diagnostic purposes, as outlined in Fig. 1.11(b). To perform such pattern classification, multiple soft-computing-based methods[6] have been achieved in literature, such as support vector machines [41], principle component analysis [18], k-nearest-neighbors, and artificial neural networks [42]. While these methods can be effective in terms of classification accuracy under specific conditions, all of them are essentially a black box where its decision-making process is either unclear or the results are difficult to explain. This drawback makes it difficult to clarify the reasons behind a false or missed alarm, and hence is less suitable for IM fault diagnosis.

A fuzzy-inference-system (FIS), however, has a clear decision-making process by using linguistic fuzzy reasoning structure, with the FIS's universe of discourse (i.e., range of input data) corresponding to different motor condition classifications [43]. However,

[6] Soft computing-based methods produce outputs based on uncertainty, imprecision, and approximate reasoning, with more flexibility in its decision-making process compared to hard computing-based methods which produce outputs based on precise, crisp reasoning [42,74].

this FIS classifier requires knowledge of specific system parameters and cannot be generalized to other systems due to differences in the sensors, DAQ systems, SNR of fault features, motor structures, and operating conditions.

To solve the problem in the classical FIS in manual parameter adjustment, the adaptive neuro-fuzzy-inference-system (ANFIS), is developed in [44],[7] which uses error back-propagation to automatically adjust FIS system parameters with its training data.[8] However, some expertise is required to specify the number of membership functions in advance and for training error control [45]. For example, if a user-specified error is too low, it tends to lead to overtraining. Under this condition, the FIS system cannot accurately assess subsequent testing inputs if these inputs have a large divergence from the training data [46,47].[9] In addition, if dynamics of the monitored system change dramatically, parameter adjustment alone may not ensure an ANFIS system to have a reasonable decision-making accuracy.

To tackle the parameter and expertise-related problems of ANFIS-based classifiers, an evolving FIS system has been developed, where both system parameters and linguistic fuzzy reasoning structure are created and evolved iteratively based on the clustering of the input training data [48,49,50]. Such clustering can be achieved with evolutionary algorithms based on measures such as data potential (a measure of data density) [49]. However, the basis of this data potential calculation on a previous datapoint at $k-1$ may cause the formed clusters to be less accurate due to it not reflecting the most recent datapoint at k [50,51,52]. In addition, aggressive clustering schemes can cause overly-simplified reasoning structures [51] which in turn, causes a deficit of rules that cannot adequately describe all the different possible output classes.

The issues related to clustering and insufficient reasoning structures reduce the interpretability of the diagnostic results, which in turn decreases the clarity of reasoning behind false or missed alarms.

---

[7] ANFIS was originally referred to as the adaptive **networked-based**-fuzzy-inference-system [44], but is now commonly referred to as the adaptive **neuro-fuzzy**-inference-system.

[8] Training is a phase where system parameters are determined based on known correct output values.

[9] Testing is a phase where there are no longer any system parameter changes, and the correct output values are used only to compare with the system outputs to determine system accuracy.

1.8 Challenges

From the aforementioned discussions in Sections 1.4.1 to 1.7.1, which relate to the different modules of an IM health condition monitoring system, the challenges that remain to be solved are summarized as follows:

- **Smart Sensor-based Wireless DAQ:** The currently-available wireless DAQ systems could not meet the requirements in terms of memory, ease of reproducibility, bandwidth, wireless communication, and power efficiency. These drawbacks will limit the sensor's ability to collect ideal signals for advanced fault detection analysis.
- **Signal Processing for Rotor Bar Fault Detection:** It remains a challenging task to reliably recognize rotor bar defects based on current signal analysis. On the other hand, fault detection under a decoupled condition (i.e., the motor shaft is disconnected from the working/load system) has not been considered in literature, despite such a condition being very useful for motor testing runs during maintenance. Moreover, motor slip often relies on encoders, which are not always available, especially in real-world industrial applications.
- **Classifier for IM Fault Diagnostics:** Existing literature on evolving fuzzy classifiers [48,49,50] has not yet addressed issues such as evolved system structure, clustering algorithms, and an incomplete rule base. These factors will cause insufficient transparency in diagnosis decision-making, where investigations into false and/or missed IM fault alarms cannot be conducted effectively.

1.9 Objectives

To tackle these aforementioned challenges, the objective of this thesis is to develop an intelligent monitoring system for more reliable IM fault diagnosis in real-time; this work will focus on broken rotor bars. The new monitoring system consists of three basic modules: smart sensor-based DAQ, signal processing, and diagnostic decision-making. The strategy is to develop new techniques and tools in each module to provide more reliable IM health condition monitoring. To achieve these goals, the proposed strategy is to develop new and more efficient technologies in each of the three modules. Specifically:

1) **Smart Sensor-based Wireless DAQ Systems:** Compact wireless smart vibration and current sensor DAQ systems will be designed, developed, and implemented for remote vibration and current data collection.
2) **Signal Processing for IM Rotor Bar Fault Detection:** A synergistic feature analysis technique will be proposed to extract representative features from both vibration and current data for broken rotor bar fault detection. A new post-processing method is developed to characterize the extracted features as diagnostic indices. In addition to the typical load cases, a decoupled motor load condition will be investigated for motor maintenance applications.
3) **Diagnostic Classifier for IM Faults:** An evolving fuzzy classifier will be developed to integrate features from several fault detection techniques for a more reliable IM fault diagnosis. This classifier will have adequate adaptive capability to accommodate variable system conditions by novel training operations.

1.10 Outline

The thesis is outlined as follows:

- Chapter 2 details the development of wireless smart vibration and current sensored-based DAQ. Some specific development strategies are also summarized.
- Chapter 3 proposes the synergistic feature analysis technique for IM rotor bar fault detection. It also discusses a new post-processing method to quantify the results and formulate representative fault monitoring indices.
- Chapter 4 discusses the experimental setup using the proposed developed smart sensor-based DAQ. The effectiveness of the proposed signal processing technique will be verified experimentally, corresponding to different motor conditions.
- Chapter 5 proposes a design of an evolving fuzzy system that can automatically diagnose IM faults; its effectiveness with respect to multiple datasets and other classifiers are also evaluated.
- Chapter 6 summarizes the contributions from this research work and possible future research and development based on the results of this work.

CHAPTER 2

Smart Sensor-based Wireless DAQ Systems

2.1 Brief Background

As stated in Section 1.4.2, multiple wireless smart sensors and transducers have been developed and validated in the past [5], [16]-[19]. However, the limitations of the aforementioned development include limited memory to store data, lack of published design considerations in terms of appropriate DAQ bandwidth, power efficiency, SNR, and reliable wireless communications. Hence, this work develops a new smart sensor-based wireless DAQ system to tackle the aforementioned problems.

2.2 Overview of Architecture

Fig. 2.1 illustrates the architecture of a wireless, battery-powered smart sensor DAQ system, which can further be subdivided into the smart sensor node(s) and a receiver.

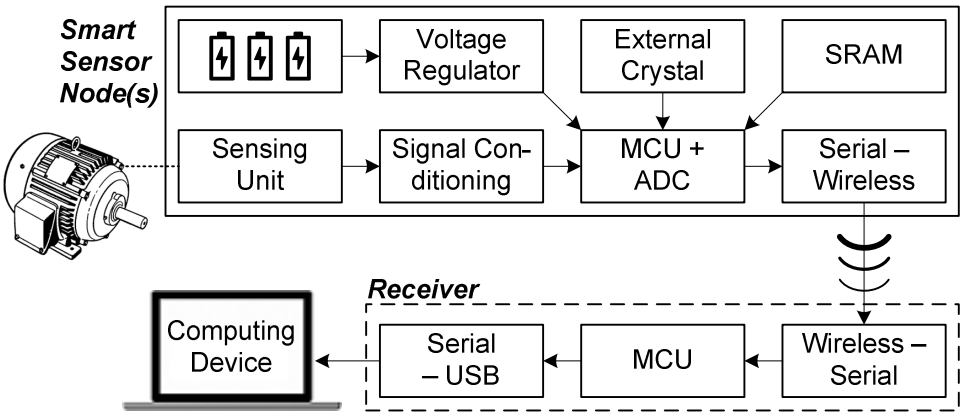

Fig. 2.1. Architecture of a wireless smart sensor DAQ system.

2.2.1 Smart Sensor Node

The sensing unit is a transducer to convert the physical signal of interest (i.e., current and vibration) into an electric signal. Its outputs get amplified and filtered in the signal conditioning module before being sampled and digitized by an ADC. The ADC is referenced to a voltage regulated output of a battery power source, with its sampling coordinated by an MCU. The battery provides power to the entire system. A precise external crystal is used to ensure consistent timing between samples. In data collection, the

MCU first collects data and then stores the collected data into a static random access memory (SRAM) before transferring its contents through a wireless transceiver.

2.2.2 Receiver

The receiver unit consists of an MCU and a wireless transceiver. Its contents are processed by an MCU before being converted in a Universal-Serial-Bus (USB) interface, readable by a connected computing device for advanced processing. The receiver system is powered by the computing device (i.e.: laptop or desktop computer) through the USB port.

2.2.3 Contributions

Novel contributions in this aspect of the work include the following:

1) A new strategy to design for signal conditioning circuits with respect to noise, bandwidth, and desired signal-to-noise ratios.
2) A new design method to ensure correctly-timed data samples.
3) A new design strategy for noise and reliable wireless transmissions.

2.3 Wireless Smart DAQ System Design

2.3.1 Sensing Element Transducers and their Strategic Applications

Two types of transducers are used for this smart sensor system: electric current and vibration. The vibration signal will be used to analyze and estimate the rotor's rotational frequency, which in turn, will be used to determine the slip. The slip is an important parameter for motor fault detection using the electric current. Vibration signals can be used to monitor the rotor frequency because the rotor slot produces a unique vibration pattern upon every shaft rotation. Relegating the vibration transducer to monitor the rotor frequency has some strategic advantages:

- Facilitates data processing since the rotor frequency is usually the dominant one, which is relatively easy to distinguish from other spectral components.
- Reduces the issue with mechanical impedance due to additional components between the point of vibration sensor mounting and the defect. This impedance

may modulate defect-related signatures with uncorrelated signals from other rotating components such as gears or bearings [53].

- Performs like a digital encoder, since the monitored rotor frequency is related to its speed and slip, as per Eq. (1.2). It can eliminate the need for any physical speed encoder hardware connected to the IM shaft, which is expensive and difficult to install in most IMs.

Based on this proposed strategic application of vibration and current signals, the required bandwidth of the related transducers can then be determined.

2.3.2 Bandwidth Considerations for a Current Transducer

In this work, the current transducer's purpose is to collect the stator current signals that are used to detect the characteristic IM fault frequencies. Based on primary current signal analysis, with a line frequency up to 60 Hz and observing the frequencies evaluated in related recent work in [40,54], a bandwidth of about ten times the main line harmonic, or 600 Hz,[10] would be sufficient for analysis in this work for rotor bar fault detection. Hence a *C-CT-16* split-core current transformer unit from Nidec Copal Electronics [55] with a bandwidth up to 5 kHz, is suitable for this application.

2.3.3 Bandwidth Considerations for a Vibration Transducer

In this work, the vibration transducer is used to collect and analyze vibration signals. It is mounted to the top of the motor. The purpose of this data analysis is to estimate the IM rotor's rotating frequency. As the rotor's rotational frequency is not expected to exceed 60 Hz in this work,[11] a lower bandwidth is acceptable. Hence, a digital accelerometer, the *LIS3DH* from STMicroelectronics [56], with a bandwidth of up to 2.5 kHz is suitable for rotor speed monitoring.

---

[10] Higher frequencies of current are possible, but have higher susceptibility to noise [5] due to the inherently low SNR of current fault features.

[11] Assuming a maximum line current of 60 Hz, then the maximum synchronous frequency with 2 poles is 60 Hz as per Eq. (1.1). Additional poles (4 poles, 8 poles, etc.) in the IM would result in lower synchronous frequencies. Hence a maximum rotor frequency approaching 60 Hz is expected in this work.

2.3.4 Sensitivity Considerations

In order to obtain an appropriate SNR, the sensing range of the transducer must meet the application requirements. In this work, the tested IMs are typical fractional-horsepower motors, which have stator current fluctuations of approximately ±1A, and vibration acceleration strengths within ± 2g.

The *LIS3DH* vibration transducer is within operational limits with a digital output range of ±2, 4, 8, 16g. The *C-CT-16* current transformer, however, has a nominal analog output range of ±100A, which necessitates additional analog signal conditioning considerations.

2.3.5 Signal Conditioning for a Current-based Output

Under the assumption that the sensor output is modeled as an AC current source, the architecture of the developed signal conditioning interface is illustrated in Fig. 2.2.

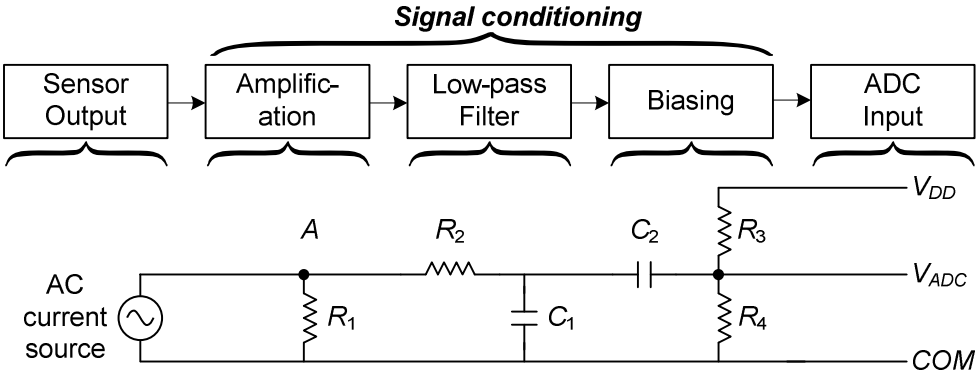

Fig. 2.2. Architecture of the signal conditioning circuit interface along with implementation for an AC-current-source-based sensor output.

The AC current source is fed into R_1 for current-to-voltage conversion.[12] R_2 and C_1 serve as a low-pass filter, with a cutoff frequency of:

$$f_{c,lpf} = \frac{1}{2\pi R_2 C_1} \tag{2.1}$$

[12] This current-to-voltage conversion can also be considered as an amplification stage, where a larger value of R_1 results in a larger output voltage.

C_2, R_3, and R_4 provide a DC bias to the original AC signal, thereby ensuring that the output is within the operating limits of a battery-powered system. The biasing stage also doubles as a high-pass filter with a cutoff frequency of:

$$f_{c,hpf} = \frac{1}{2\pi \left(R_3 \parallel R_4\right) C_2} \tag{2.2}$$

Hence, these cutoff frequencies define the effective bandwidth of the sensor, B_W:

$$B_W = f_{c,hpf} - f_{c,lpf} \tag{2.3}$$

B_W should be compatible with the frequency requirements of the fault detection application. To ensure consistent sensor outputs throughout the range of B_W, the impedance to the right of point A in Fig. 2.2 should exceed that of the amplifying resistor, R_1, or:

$$R_1 < \left| R_2 + \left\{ Z_{C_1} \parallel (Z_{C_2} + R_3 \parallel R_4) \right\} \right| \tag{2.4}$$

where Z_C is the capacitor's impedance, bound by the low-pass and high-pass cutoff frequencies expressed as:

$$Z_C = \frac{1}{j2\pi f C} \quad ; \quad f \in [f_{c,hpf}, f_{c,lpf}] \tag{2.5}$$

To ensure correct ADC performance, the impedance referred at the output of the ADC, or $\left|Z_{ADC}\right|$, should also be below a limit for optimal ADC performance (as per component specifications):

$$\left|Z_{ADC}\right| > \left| R_3 \parallel R_4 \parallel (Z_{C_2} + Z_{C_1} \parallel [R_2 + Z_A]) \right| \tag{2.6}$$

where Z_A is the impedance of R_1 in parallel with the equivalent impedance of the sensor.

2.3.6 ADC Bit Resolution Considerations

The usable bit resolution of the ADC is selected based on the noise levels present in the sensing unit:

$$V_{inc} = \frac{\left|\Delta V_{DD}\right|}{2\hat{}\{N_{bit}\} - 1} \geq V_{n,pp} \tag{2.7}$$

where V_{inc} is the minimum incremental voltage for the least-significant-bit of the ADC, $|\Delta V_{DD}|$ is the range of the voltage referenced by the ADC, and N_{bit} is the bit resolution of the ADC. $V_{n,pp} = V_{n,rms}\ k_{CF}$ is the peak-to-peak voltage fluctuations of the sensing unit output due to noise; $V_{n,rms}$ is the voltage root-mean-square (RMS) of white noise in the sensing element; and k_{CF} is a conversion factor related to the standard deviation of Gaussian noise. For instance [57], k_{CF} = 3 ~ 6.6 corresponds to a probability of approximately 87% to 99.9%, in which the value of $V_{n,pp}$ will satisfy Eq. (2.7). $V_{n,rms}$ can be approximated as:

$$V_{n,rms} \cong V_{n,w}\sqrt{B_W N_B} \tag{2.8}$$

where $V_{n,w}$ is the voltage noise spectral density of sensor white noise; N_B is the equivalent noise bandwidth multiplication factor associated with non-idealities of actual filtering [57,58]. For a first-order filter used in the signal conditioning, as depicted in Fig. 2.2, N_B has a value of $\pi/2$. The approximation of Eq. (2.8) is valid as long as the lower-end-frequency of the bandwidth is close to the low-frequency-noise corner frequency of the sensor, f_{CO}, and the higher-end-frequency is at least an order of magnitude higher than f_{CO}.[13]

2.3.7 Data Pre-processing and Storage

The chosen MCU data processor [59] is the *ATmega328P*, which includes a built-in 10-bit ADC, operating within the noise-related bit resolution restrictions discussed in Section 2.3.6. This ADC has a sampling frequency of up to 15 kHz for 10-bit data, and is therefore compatible with the chosen current and vibration transducers.

Due to the processor requiring quick storage and retrieval of data, SRAM is used in this project. The internal SRAM of the *ATmega328P* is two kilobytes (kB), with two

[13] Assuming $f_{CO} = f_{c,hpf}$ then as per [57], $V_{n,rms} = V_{n,w}\sqrt{\left[f_{c,hpf}\ \ln\frac{f_{c,hpf}}{f_{c,lpf}} + \left(f_{c,lpf} - f_{c,hpf}\right)\right]N_B}$.
The larger $f_{c,lpf}$ is, with respect to $f_{c,hpf}$, the more accurate the approximation of Eq. (2.8).

bytes required to store every 10-bit data sample, thereby allowing 1000 data samples to be stored. As this amount is insufficient for IM condition monitoring purposes, an additional SRAM chip, the *23LC1024* from Microchip [60], is used in this work to provide 128 kB of additional memory, allowing for 64,000 data samples.

2.3.8 Wireless Communications

For wireless transmissions, a 915 MHz transceiver [61], the *A1101* from Anaren, is chosen because it is an entire wireless system-on-chip (SoC), requiring only digital signals for interfacing. This 915 MHz carrier frequency is in compliance with Canada's allocated band for Industrial, Scientific, and Medical purposes [62]. The choice of an SoC solution thereby can eliminate the need for more advanced design and PCB considerations, such as impedance matching. To reduce transmission overhead, a customized version of the Simple Wireless Abstract Protocol (SWAP) is used [63].

2.3.9 Chip-to-chip Communications

For rapid chip-to-chip communications, the Serial-Peripheral-Interface (SPI) protocol is used [64], as the chip selection involves only a change of a digital output (DOUT) state.[14] A scheme to connect the digital vibration transducer, SRAM, and transceiver via SPI is illustrated in Fig. 2.3. The ATmega328P processor has a maximum of 16 DOUTs, and contains built-in SPI pins, which is therefore well-suited to handling the multiple chip-to-chip communications required in this work.

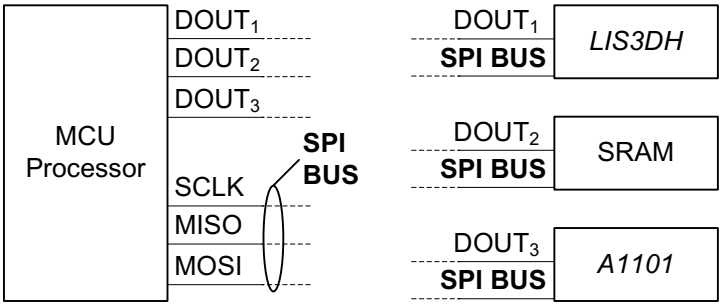

Fig. 2.3. SPI connection scheme.

[14] In comparison to the alternative I2C protocol, which requires two separate transmissions for device addressing and data transfer [64].

2.3.10 Receiver Considerations

The receiver uses the same wireless transceiver and MCU processor as contained in the smart sensor nodes, but requires a means to transfer the received data using a computing device. As the *ATmega328P* primarily outputs via serial communications, and computing devices primarily input with USB communications, another chip is required to handle communications between the serial and USB devices. The choice of chip to suit these communications is the *FT231X* from Future Technology Devices International Ltd. [65]. As such chips are required not only for programming, but also for burning the bootloader to activate the functional frequency of the MCUs. The *FT231X* is a suitable choice for quick and direct access to both communications and programming of the MCU.

2.4 Other Strategies in Smart DAQ Development

2.4.1 Noise reduction

Random noise adversely affects the operation of the smart sensors, resulting in incorrect samples being stored during data collection. For a smart sensor, there are two main sources of noise, electronic and electromagnetic interference (EMI).

Electronic noise: Random electronic noise such as thermal, shot, flicker, and burst noise exists mainly due to the inherently probabilistic nature of electron flow within semiconductors [66]. They can be mitigated using the following strategies:

1) Using printed circuit board (PCB) design techniques such as having ground and power planes adjacent to one another to reduce high frequency impedance.[15]
2) Minimizing crosstalk and current return paths between the high-frequency circuit traces (e.g., SPI communication lines, crystal oscillator) and low-frequency ones (e.g., analog signals, power lines).
3) Performing standard PCB design best practices for trace routing in the context of decoupling capacitors and signal isolation [67].

[15] Assuming noise is primarily higher frequency and having lower impedances at higher frequencies would dissipate more noise-related energy.

EMI noise: In addition to existing EMI noise in the environment that can interfere with the smart sensor operations, the internal switching of the MCU can also radiate EMI, as every pin on the MCU is potentially susceptible to this noise [68]. This issue can be mitigated by the use of pullup resistors on all unused input-output pins to prevent unintended switching of the MCU pins [69], and to avoid incorrect data collection/digitization operations.

2.4.2 Consistent Sampling Times

To ensure the time between samples is consistent, the crystal oscillator must have sufficient accuracy to minimize oscillator jitter. Oscillator jitter is a phenomenon where the periods of oscillation differ in every cycle due to random noise from different sources [70] such as the electronic and EMI noise sources as detailed in Section 2.4.1. This accuracy affects the frequency components of a signal. The frequency components of a signal should be able to distinguish down to the frequency resolution, f_{RES}, defined as,

$$f_{RES} = \frac{f_s}{N} \tag{2.9}$$

where f_s and N are the sampling frequency and total number of samples, respectively.

Shown in Fig. 2.4 is a Pierce-Gate crystal oscillator circuit used in this work, where U_1 is a digital CMOS inverter internal to the selected *Atmega328P* MCU, R_f is the feedback resistor to linearize the inverter, X_1 is a crystal oscillator component, C_3 and C_4 are the load capacitors for X_1. The value of R_f is selected based on typical values for a given frequency of X_1 as suggested in [71]; C_3 and C_4 are selected based on the required load values specified in the datasheet of X_1.

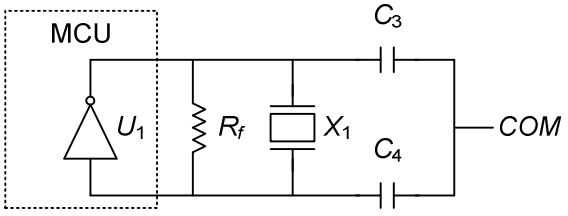

Fig. 2.4. Pierce-Gate crystal oscillator circuit.

The influence of the oscillator accuracy on results are shown in Fig. 2.5 and Fig. 2.6 where identical amplitude-modulated data are collected and digitized with two smart sensor prototype systems. The expected frequency-domain result is a center carrier frequency of approximately 50 Hz with 0.4 Hz sideband frequencies. Both systems have identical frequency resolutions of around 0.02 Hz, where one system uses an internal RC oscillator with an accuracy of 10,000 parts-per-million (ppm), and other using an external crystal oscillator with an accuracy of 30 ppm.

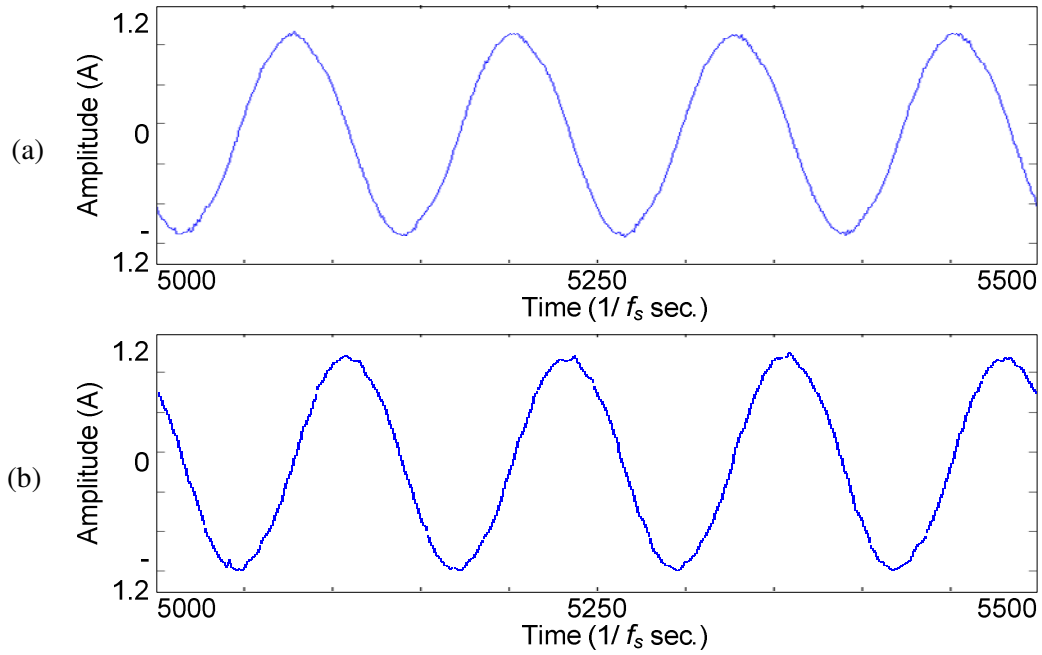

Fig. 2.5. Time-domain results of collected data using: (a) 30 ppm external crystal oscillator, (b) 10,000 ppm internal RC oscillator.

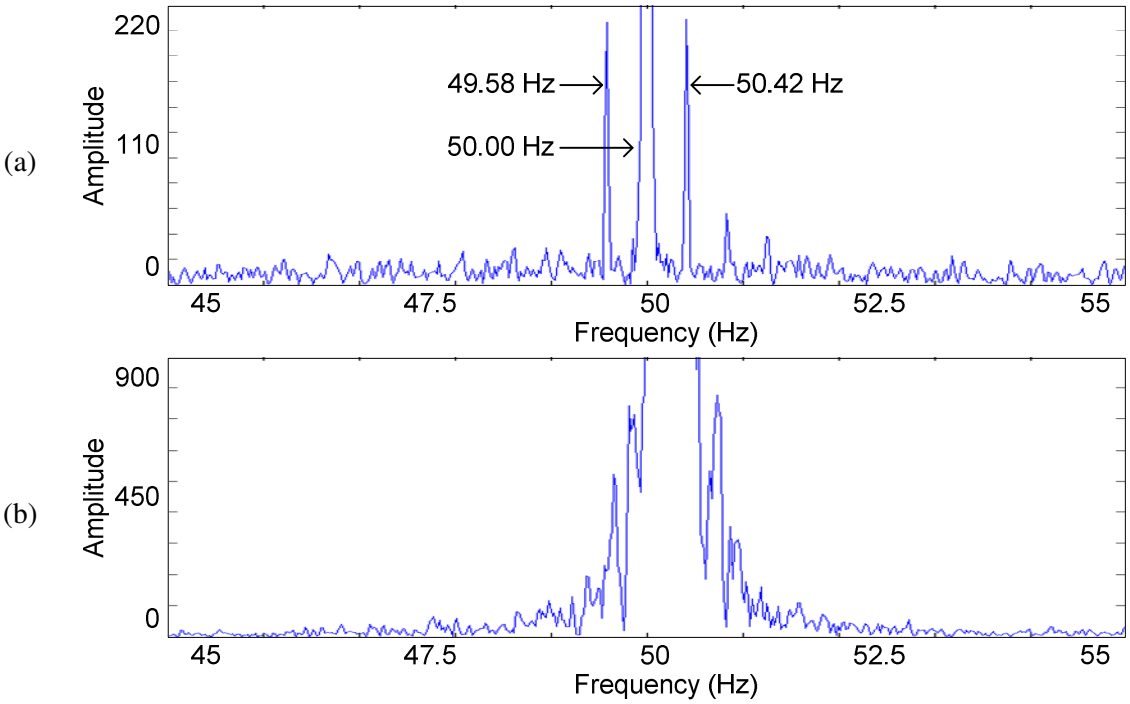

Fig. 2.6. Frequency-domain results of collected data using: (a) 30 ppm external crystal oscillator, (b) 10,000 ppm internal RC oscillator.

Despite the different sensor systems showing near-identical time-domain results as per Fig. 2.5(a)(b), a clear difference is observed in the frequency-domain results of Fig. 2.6(a)(b). The 30 ppm oscillator system can distinguish sideband frequencies 0.42 Hz away from the main 50 Hz frequency; the 10,000 ppm oscillator system, however, cannot distinguish these frequencies, despite both systems having the same frequency resolution. Hence, the 30 ppm oscillator is a requirement for data collection in most rotor bar fault detection techniques that depend on a precise analysis of spectral properties [6,18,36,41].

2.4.3 Sampling Frequency

Though the ADC of the *ATmega328P* MCU [59] has a theoretical maximum sampling frequency of 15 kHz, there are several factors that influence the actual sampling frequency that can be implemented in the developed smart DAQ system:

1) **Bit resolution of data:** Since the MCU is an 8-bit processor, it requires additional processing cycles to process a 10-bit datapoint. This extra processing time contributes to a reduction in the sampling frequency.

2) **Speed and energy consumption:** The MCU can theoretically support a clock frequency up to 20 MHz. However, to reduce power consumption, the clock frequency of the MCU is set to 8 MHz via software boot loader burning. This lower clock frequency can contribute to a reduction in the sampling frequency.
3) **SPI device communications:** Additional processing time is required in communications between the MCU and the SRAM and transceiver components since the SPI protocol requires several additional processing cycles. In the case of the SRAM, additional cycles are required to specify the SRAM memory address prior to storage and retrieval. These extra communication delays contribute to a reduction in the sampling frequency.
4) **Digital switching speed:** Since the SPI communications are initiated with a digital output pin from the MCU, the digital output switching speed can be improved by software and hardware. With hardware, pullup resistors on the digital pins are used to ensure the switching times are minimized. With software, the digital pin operations are optimized for more direct control. In addition, the MCU's code can be optimized to reduce complexity and processing times. These combined factors can contribute to an increase in the sampling frequency.

Due to the above factors, the actual maximum sampling frequency of the smart sensor DAQ system is around 5 kHz. However, this is within the bandwidth requirements as discussed in Section 2.3.2. To improve the frequency resolution as per Eq. (2.9), the sampling frequency can be reduced and fine-tuned with delays based on internal timers of the MCU; the external oscillator allows these delays to be precise enough for the application of rotor bar defect detection. In this work, the sampling frequency is set to approximately 1 kHz with 64,000 samples for a frequency resolution of 0.0156 Hz.

2.4.4 Wireless Communications Implementation Strategy

The wireless communications are based on a custom protocol that expands on the existing SWAP protocol [63]. To ensure reliable data communications, a two-way handshake protocol is implemented in this work to prevent data loss:

1) The receiver sends commands repeatedly until the transmitter acknowledges.

2) The transmitter completes a command, and then sends an acknowledgement of command completion until the receiver acknowledges.

The chosen *A1101* transceiver allows up to 61 Bytes to be sent per wireless packet transmission with the first Byte specifying the wireless address of the destination device. Since each data sample requires two Bytes, one packet can transfer up to 30 data samples. Wireless commands are differentiated with different transmission packet sizes. Such commands include:

1) Change data sampling size.
2) Change sampling frequency delay.
3) Change wireless packet delay.
4) Reset MCU.
5) Control MCU sleep mode.
6) Initiate data sampling collection and storage into SRAM.
7) Initiate wireless transfer of data from SRAM.

Since this transceiver cannot perform multiple communications simultaneously within the same frequency channels, data sampling is initiated by rapid sequential commands to start data collection and then store the data to the smart sensor's SRAM. This allows for near-simultaneous data collection operations from multiple sensors. Afterwards, the data is sequentially retrieved from multiple sensors. Possible network topologies for such a communications scheme are illustrated in Fig. 2.7.

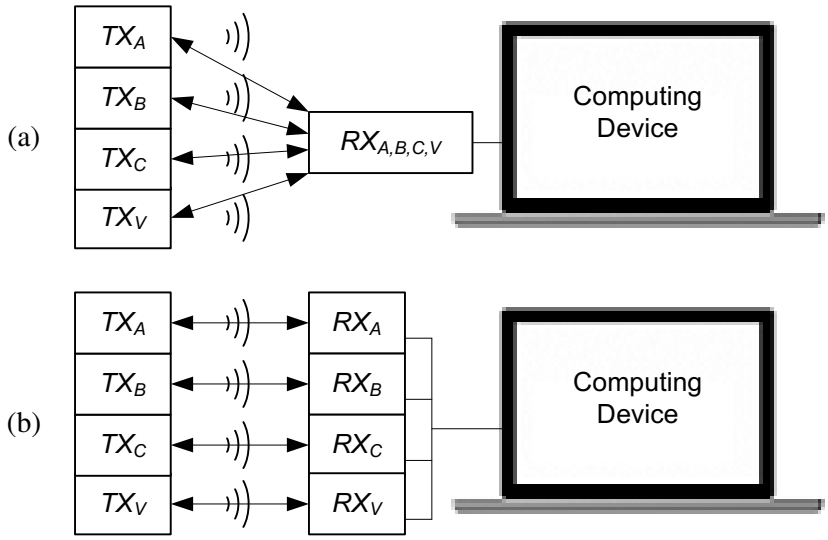

Fig. 2.7. Possible wireless network topologies for sequential smart sensor communications: (a) star topology, (b) one-to-one topology.

Though the star topology would be efficient for sequential communications, this work opts for the one-to-one topology for higher reliability due to the lack of any single point of failure, i.e., a single receiver failure in the star topology of Fig. 2.7(a) will halt all data collection operations.

The delay between each wireless packet should be selected properly; a longer delay can result in more reliable communications, but higher power consumption, whereas a shorter delay can result in faster communications, but may lock up the transceiver due to a current overload. Hence, the delay between each wireless packet should be set to an optimal value; in this work, a wireless delay of 15 ms is used.

Due to the sensitive nature of the wireless transceiver, it is possible that rapid functions or EMI noise may unexpectedly lock up the MCU, ceasing all communications and operations. To tackle this problem, a watchdog timer [72] is implemented to periodically reset the MCU if any smart sensor system node becomes unresponsive for a certain amount of time (e.g., 8 seconds in this work).

CHAPTER 3

Synergistic Feature Analysis Technique for IM Rotor Bar Fault Detection

3.1 Brief Background

As stated in Section 1.6.2, several MCSA-based techniques have been proposed in the past such as (1) spectral sideband analysis [36,37,38], (2) time-domain analysis [5], (3) spectral analysis of magnetomotive force harmonics [6], and (4) time-frequency analysis [39,40], with their respective primary disadvantages being (1) susceptibility to speed oscillation of connected gear boxes, (2) high sampling frequency requirement, (3) lack of a practical means to estimate IM slip, and (4) inapplicability to actively running motors. Hence, this work develops a new rotor bar fault detection scheme to alleviate the aforementioned problems.

3.2 General Overview

As illustrated in Fig. 3.1, vibration and current signals are collected from an IM using the developed smart sensor DAQ systems. The signals are transferred wirelessly to the receiver connected to a computing device, such as a laptop or a workstation. The data are then further processed for the IM rotor bar fault diagnosis.

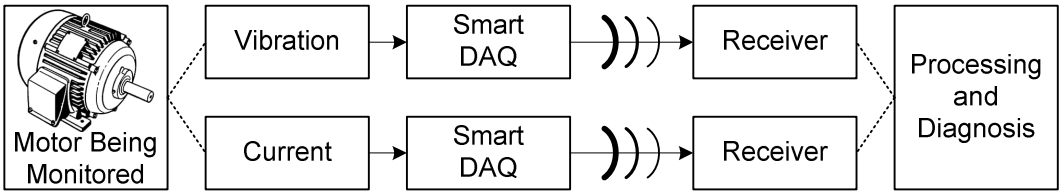

Fig. 3.1. Block diagram of the processes for IM rotor bar fault detection.

3.2.1 Contributions

Novel contributions in this aspect of the work include the following:

1) A new strategy of fault feature extraction, based on even multiples of a slip-based frequency.
2) A synergistic feature analysis technique for accurate fault detection.
3) A means to verify consistent rotor frequency to ensure correct fault feature extraction.

4) A post-processing method to formulate a signal-to-noise-ratio-based fault index based from the extracted features.

3.3 Fundamental Analysis

3.3.1 Overview

In the MCSA-based broken rotor bar fault detection, the severity of the fault is analyzed based on the spectral magnitude at a characteristic fault frequency, f_{bb}, which is determined by [6,28]:

$$f_{bb}(z,s) = f_L[z(1-s) \pm s] \tag{3.1}$$

where f_L is the line current frequency of the IM through the stator coils, s is the slip, and z represents both the time and space harmonics of the voltage and magnetomotive force waves, respectively. The applicable values of z shall be investigated in the subsequent sections.

3.3.2 Even Harmonic Analysis

Due to the symmetrical nature of the input current and voltage to an IM in the time domain (i.e., the first half of the signal period has symmetry with the second half), an even number of harmonics cannot exist. Such a qualitative analysis is demonstrated in Fig. 3.2 [73].

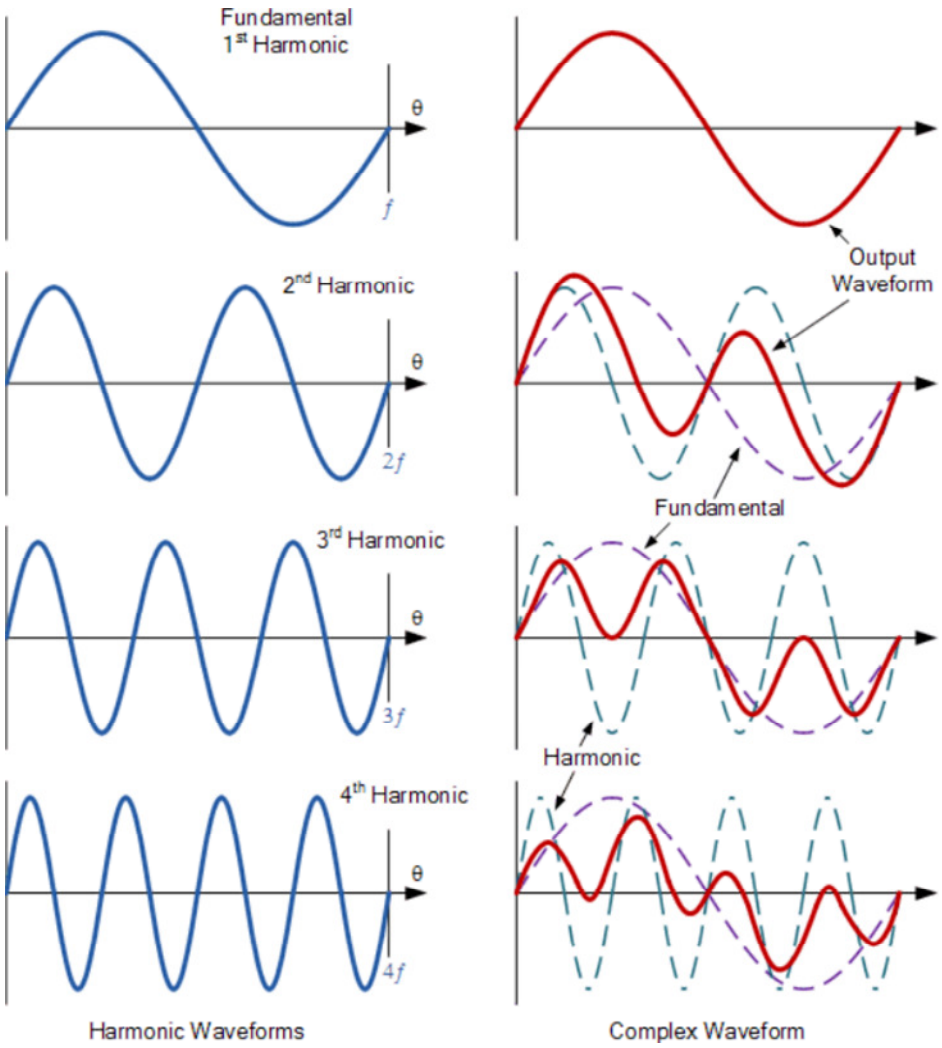

Fig. 3.2. Even and odd harmonics in a signal waveform, reproduced from [73].

3.3.3 Odd Harmonic Analysis

Assume a 3-phase wye connection of lines *A*, *B*, and *C*, with their respective voltages being v_A, v_B, and v_C, as shown in Fig. 3.3.

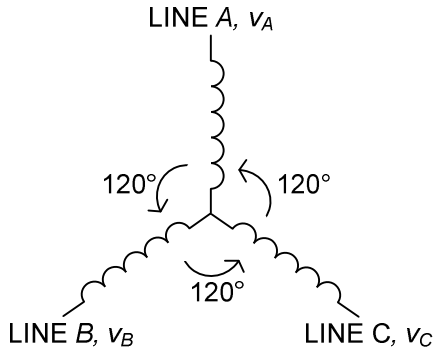

Fig. 3.3. 3-phase connection of an induction motor.

The voltages along with their harmonics can be expressed as [74]:

$$\begin{aligned} v_A &= V_1 \sin(\omega t) + V_3 \sin 3(\omega t) + V_5 \sin 5(\omega t) + \ldots \\ v_B &= V_1 \sin\left(\omega t - \frac{2}{3}\pi\right) + V_3 \sin 3\left(\omega t - \frac{2}{3}\pi\right) + V_5 \sin 5\left(\omega t - \frac{2}{3}\pi\right) + \ldots \\ v_C &= V_1 \sin\left(\omega t - \frac{4}{3}\pi\right) + V_3 \sin 3\left(\omega t - \frac{4}{3}\pi\right) + V_3 \sin 5\left(\omega t - \frac{4}{3}\pi\right) + \ldots \end{aligned} \tag{3.2}$$

with V_n being the amplitude of the *n*th harmonic.

Further analysis of the third harmonic of each phase results in:

$$\begin{aligned} v_{A,3} &= V_3 \sin(3\omega t) \\ v_{B,3} &= V_3 \sin(3\omega t - 2\pi) = V_3 \sin(3\omega t) \\ v_{C,3} &= V_3 \sin(3\omega t - 2\pi) = V_3 \sin(3\omega t) \end{aligned} \tag{3.3}$$

Assuming a balanced system where all voltages are equivalent across all phases, then no third-multiple harmonic current will flow from one phase line to another. Hence, this third-multiple harmonic current can be ignored.

3.3.4 Fundamental Analysis

From the analysis of Sections 3.3.2 and 3.3.3, z is restricted to odd, non-third-multiple harmonics, expressed as:

$$z = 1, 6k \pm 1 \tag{3.4}$$

with $k = 1,2,\ldots$ being a positive integer.

A common generalization of Eq. (3.1) is to consider its strongest fault spectral component at a left sideband to f_L; in addition, a corresponding spectral component at a right sideband to f_L, due to speed ripple [37], can be considered:

$$f_{bb,sb-} = f_L[1 - 2s] \tag{3.5}$$

$$f_{bb,sb+} = f_L[1 + 2s] \tag{3.6}$$

where its corresponding fault severity can be estimated by the addition of the amplitudes of both sideband components. However, a problem for such estimation is that these sideband spectral components can be strongly influenced by the speed oscillation of the IM's driving/load system (e.g., a connected gearbox). The characteristic frequencies of such oscillations can be expressed as:

$$f_{osc} = f_L\left[\mathrm{z} \pm k\frac{f_R}{r}\right] \tag{3.7}$$

where r is the speed reduction ratio of the gear train.

Studies have shown that the influence of f_{osc} at the fifth and/or seventh harmonics is diminished compared to its effect at near the fundamental line frequency [6]. Investigation of these harmonics features with Eq. (3.1) yields:

$$f_{bb}(5,s) = f_L[5-4s] \vee f_L[5-6s] \tag{3.8}$$

$$f_{bb}(7,s) = f_L[7-6s] \vee f_L[7-8s] \tag{3.9}$$

where $\vee$ denotes the logical "or" operator.

Assume that the rotational magnetomotive force components of a faulted rotor bar are also a phenomenon of rotor magnetic asymmetry, Eq. (3.8) and Eq. (3.9), along with empirically-observed evidence in [6], illustrate that the broken bar symptom can be characterized by even multiples of the slip frequency. Then, Eq. (3.1) can be further generalized as:

$$f_{bb,gen} = f_L[\mathrm{z} - 2ms] \tag{3.10}$$

where $m \in [1,2,\ldots,\{(z+1)/2\}]$; $z > 1$.

Substituting Eq. (1.1) and Eq. (1.2) into Eq. (3.10) yields:

$$f_{bb,gen} = f_L \left[z - 2m\left(1 - \frac{p}{2}\frac{f_R}{f_L}\right)\right] \tag{3.11}$$

In this work, the line frequency f_L is determined based on current sensor data. On the other hand, the rotor frequency f_R will be estimated by processing vibration data since the rotor slot produces a periodic vibration pattern after each shaft rotation. The purpose is to determine the characteristic fault frequency using a combination of current and vibration features.

3.3.5 Processing Procedures

The flowchart of the proposed synergistic processing technique is illustrated in Fig. 3.4, which consists of the following steps:

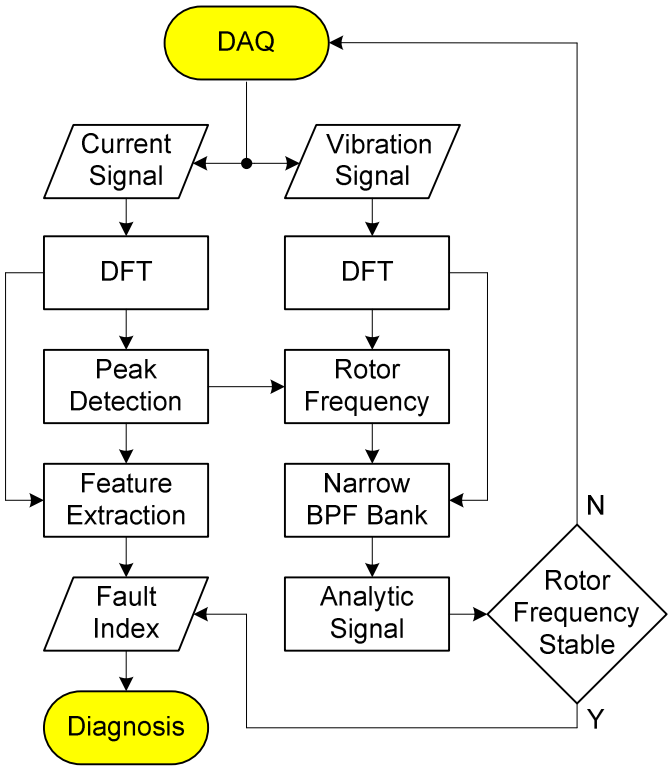

Fig. 3.4. Flow chart of synergistic feature analysis.

1) Collect the current and vibration signals by using the developed wireless smart DAQ system.
2) Conduct the discrete Fourier transform (DFT) of the signals. Use a Hanning window to reduce spectral leakage.

3) Recognize the current line frequency, f_L, from the current spectrum analysis.
4) Use f_L to estimate f_R by analyzing spectral properties of the vibration spectrum within a certain bandwidth.
5) Filter out the vibration signal with a bank of band-pass filters (BPF).
6) Formulate the analytic signal, and determine the instantaneous frequency (*IF*) and instantaneous amplitude (*IA*) of f_R.
7) Test the consistency of f_R, then extract the characteristic fault features from the current spectrum.
8) Generate a fault index for online IM health condition monitoring.

The signal processing for steps 5) to 8) will be discussed in the following sub-sections.

3.3.6 Band-pass Filtering for Rotor Frequency Analysis

The center frequency of the first BPF of the BPF bank is selected as the peak of the narrowed-down vibration spectrum range to estimate rotor frequency, f_R, as described in Section 3.3.5. To improve accuracy, the BPFs in the bank are overlaid as illustrated in Fig. 3.5, and defined by:

$$f_b(i) \in \left[f_c - \frac{f_{spr}}{2} Z_{th}, f_c + \frac{f_{spr}}{2} Z_{th} \right] \tag{3.12}$$

where $f_b(i)$ is the *i*th band of frequencies for the BPF; f_c and f_{spr} are the respective center and spread of the BPF frequency bands; $Z_{th} \in (1, 2)$ is a factor that is selected to ensure that all the ranges of frequencies overlap. Each $f_b(i)$ band includes some characteristic frequencies, and should cover bands from the motor's speed f_R at full load, to the synchronous frequency, f_{SY}. f_{spr} can be selected as 1 Hz in this case, representing a range of 60 r/min in f_R variations.

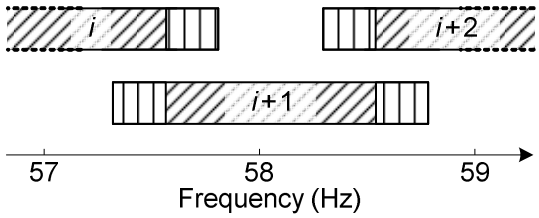

Fig. 3.5. Implementation of the band pass filter bank: diagonal lines represent nominal range; vertical lines denote overlap ranges.

Having a BPF can limit the frequency content to consist of f_R and ensure a monocomponent signature. Such narrow bands can also reduce the higher frequency components that may cause local minima and maxima [75]. As a result, the selected narrow bands can facilitate the formulation of the analytic signal [76].

3.3.7 Formation of the Vibration Analytic Signal

A direct formulation approach is proposed in this subsection to formulate the vibration analytic signal. Assume a vibration signal $x[n]$ with M samples. To aid subsequent computations, only an even number of samples, N, are considered, where:

$$N = M - (M \bmod 2) \tag{3.13}$$

The discrete analytic signal, $y[n]$, is computed by:

$$y[n] = x[n] + jH(x[n]) \quad ; \quad n = 1,2,\ldots,N \tag{3.14}$$

where $H(\bullet)$ denotes the Hilbert transform.

Taking the DFT, denoted by $F\{\bullet\}$, on Eq. (3.14) yields:

$$Y[k] = X[k] + jF\{H(x[n])\} \tag{3.15}$$

where $k = 1, 2,\ldots,N$. The domains of $k = 1, 2,\ldots,(N/2+1)$ and $k = (N/2+2),\ldots,N$ represent positive and negative frequencies, respectively; the positive frequencies, f_+, correspond to:

$$f_+ = \frac{k-1}{N/2} \cdot \frac{f_s}{2} \tag{3.16}$$

The Hilbert transform of $x[n]$ yields:

$$H(x[n]) = x[n] * \frac{1}{\pi n} \tag{3.17}$$

Take the DFT of Eq. (3.17) then:

$$F\{H(x[n])\} = X[k] \cdot F\left\{\frac{1}{\pi n}\right\} \tag{3.18}$$

where,

$$F\left(\frac{1}{\pi n}\right) = \begin{cases} -j & k \in [2, N/2+1] \\ +j & k \in [N/2+2, N] \end{cases} \tag{3.19}$$

Assume $\hat{Y}[k] = X[k]$ when $k = 1$; substituting Eq. (3.18)-(3.19) into Eq. (3.15) yields [76]:

$$\hat{Y}[k] = \begin{cases} X[k] & k = 1 \\ 2X[k] & k \in [2, (N/2+1)] \\ 0 & k \in [(N/2+2), N)] \end{cases} \tag{3.20}$$

The analytical signal of Eq. (3.14) is computed by taking the inverse DFT of Eq. (3.20) or:

$$y[n] = F^{-1}\{Y[k]\} = x[n] + jH(x[n]) \tag{3.21}$$

The corresponding *IA* and *IF* of the vibration signal are then computed as follows:

$$IA[n] = \sqrt{x[n]^2 + H(x[n])^2} \tag{3.22}$$

$$IF[n] = \frac{1}{2\pi}\frac{d\theta[n]}{dt} = \frac{1}{2\pi}\frac{\theta[n+1]-\theta[n]}{1/f_s} \tag{3.23}$$

$$\theta[n] = \tan^{-1}\frac{H(x[n])}{x[n]} \tag{3.24}$$

where $n+1$ represents a $1/f_s$ increment in the time domain.

Eq. (3.22)-(3.24) demonstrate how to directly apply the analytic signals by Eq. (3.20)-(3.21) for analysis, in comparison with the existing literature on the subject in [76,77,78].

3.3.8 Determining Spread of Rotor Shaft Frequency

The computed *IF* and *IA* from Eq. (3.22)-(3.24) can be used to determine the spread of the rotor shaft vibration frequencies, f_R. First, recognize the BPF band that contains the maximum *IA*:

$$f_b(i_{\max}) \in \max(IA[n])\big|_{\forall f_b(i)} \tag{3.25}$$

Consider the *IF* as being caused by f_R; its corresponding *IA* should satisfy the condition of $IA > Q$, where:

$$Q = \left\{ \max(IA[n]) - \hat{Z}_{TH} \left[\max(IA[n]) - \text{mean}(IA[n]) \right] \right\} \Big|_{f_b(i)}, \quad i = i_{\max} \tag{3.26}$$

$\hat{Z}_{TH} \geq 1$ is chosen such that:

$$Q > \left\{ \max\left(IA[n]\right) \right\} \Big|_{f_b(i)}, \quad i \neq i_{\max} \tag{3.27}$$

Eq. (3.27) can be used to choose the frequency band containing more energy than the other bands, which is therefore more likely to contain f_R. If no BPF band contains greater energy than the other BPF bands (with respect to a threshold established by Eq. (3.26)), it implies that f_R varies greatly in data sampling. Such a wide spread of f_R would degrade the motor fault detection accuracy, since fault detection generally requires a consistent value of f_R during the DAQ process, as per Eq. (3.11). In this case, the DAQ process should be repeated until f_R satisfies this requirement.

3.3.9 Post-processing for Fault Index Formulation

Post-processing is a procedure to quantify the extracted feature properties for online IM condition monitoring. A new fault index, F_I, is formulated as:

$$F_I\left(f_{fault}\right) = \begin{cases} \dfrac{1}{L}\displaystyle\sum_{i=1}^{L}\left[\frac{1}{3}\sum_{J=1}^{3}\left\{\frac{\beta}{\xi}-1\right\}_J\right]_i & \text{if } \beta > \xi \\ 0 & \text{Otherwise} \end{cases} \tag{3.28}$$

Eq. (3.28) represents an average of extracted features over *L* data sets, across *J* phases (e.g., three phases of current in this work). Within the *i*th data set, ξ is an approximation of the noise floor, computed based on the average of the current spectrum:

$$\xi = \frac{1}{N/2+1}\sum_{k=1}^{N/2+1}\left\{\frac{\lambda}{N}\left|X_I[k]\right|\right\} \tag{3.29}$$

where X_I consists of spectral amplitudes of the current spectrum. In addition, within the *i*th data set, β is the spectral amplitude corresponding to a theoretical fault characteristic frequency, f_{fault}:

$$\beta = \frac{\lambda}{N}\left| X_I[k_\beta] \right|; \quad k_\beta \to f_{fault} \tag{3.30}$$

where λ is a scaling factor to facilitate feature extraction.

Since λ is used in both Eq. (3.29) and Eq. (3.30), the choice of λ does not influence the formulation of F_I in Eq. (3.28); Eq. (3.28) could facilitate the generation of a more accurate diagnostic index, which will be demonstrated in the proceeding chapter.

CHAPTER 4

Performance Evaluation for Smart Sensors and Synergistic Feature Analysis Technique

4.1 Experimental Setup

To evaluate the effectiveness of the proposed technologies, a series of tests are undertaken under different IM conditions. The experimental setup used in this work is outlined in Fig. 4.1 and Fig. 4.2. It consists of a tested IM, a gearbox for speed reduction, and a magnetic clutch load system. Fig. 4.3 - Fig. 4.5 illustrate the developed wireless smart sensor DAQ systems used to collect both vibration and current signals.

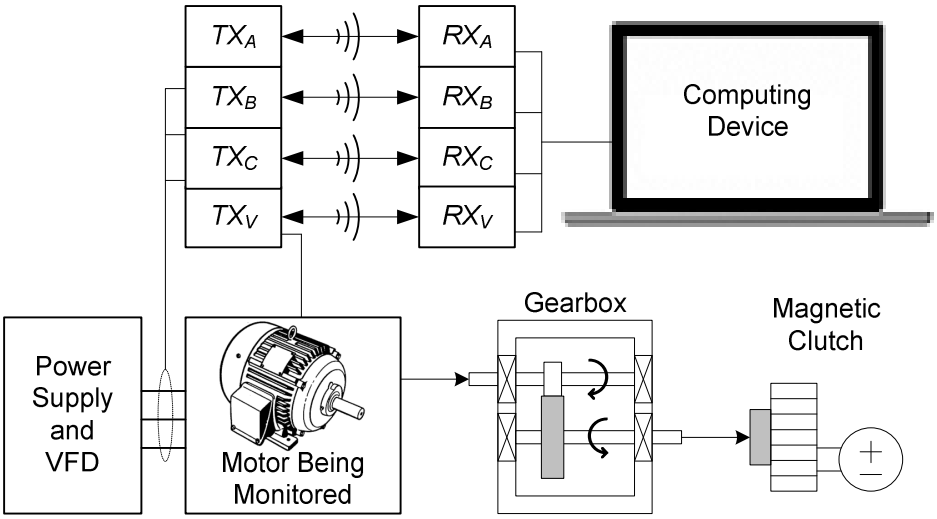

Fig. 4.1. Experimental setup, symbolic representation, showing smart sensors collecting data from an IM connected to a VFD supplied with 3-phase power; The IM's shaft is connected to a gearbox; the gearbox's output shaft is connected to a magnetic clutch.

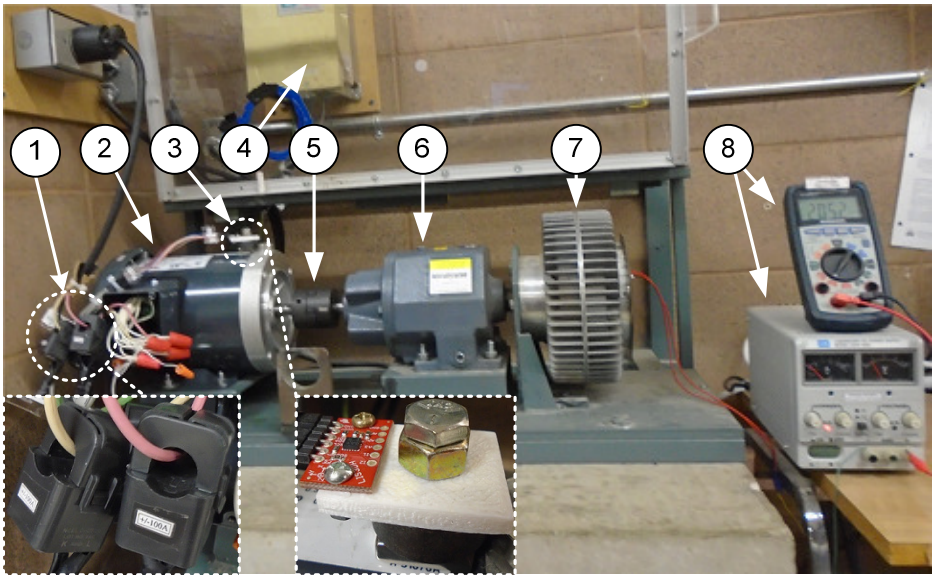

Fig. 4.2. Experimental setup, physical representation :(1) current transformers, (2) IM under test, (3) digital vibration transducer, (4) power source and VFD, (5) coupling, (6) speed-reduction gearbox, (7) magnetic clutch, (8) DC power source.

(a)

(b)

(c)

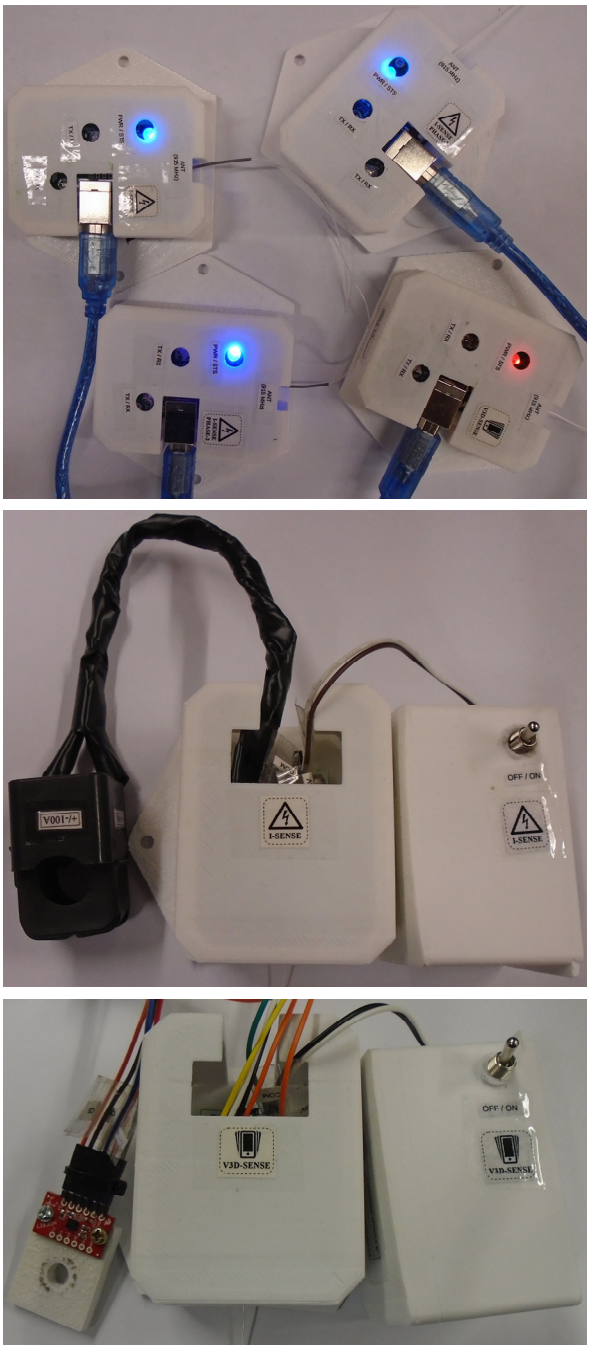

Fig. 4.3. Casing of the developed wireless smart DAQ system prototypes: (a) receivers, collecting three phases of current data (blue LEDs) and vibration data (red LED), (b) smart current sensor, from left to right, current transformer, main processing board, power module, (c) smart vibration sensor, from left to right, digital vibration transducer, main processing board, power module.

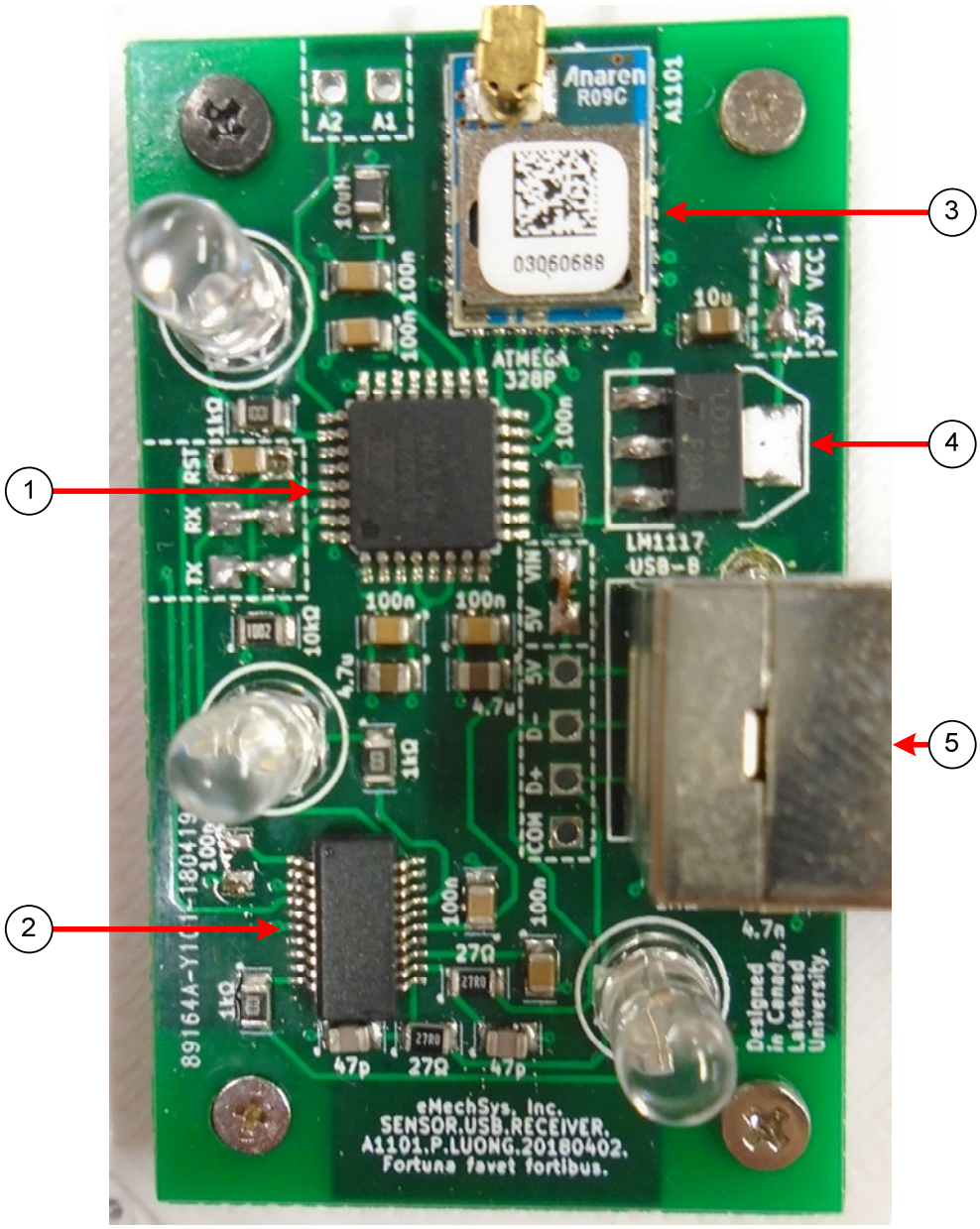

Fig. 4.4. Internal PCB of the developed wireless receiver prototypes: (1) microcontroller, (2) serial-to-USB interface chip, (3) wireless transceiver, (4) voltage regulator, (4) external crystal, (5) USB connector. PCB dimensions: 32.97 mm x 55.11 mm.

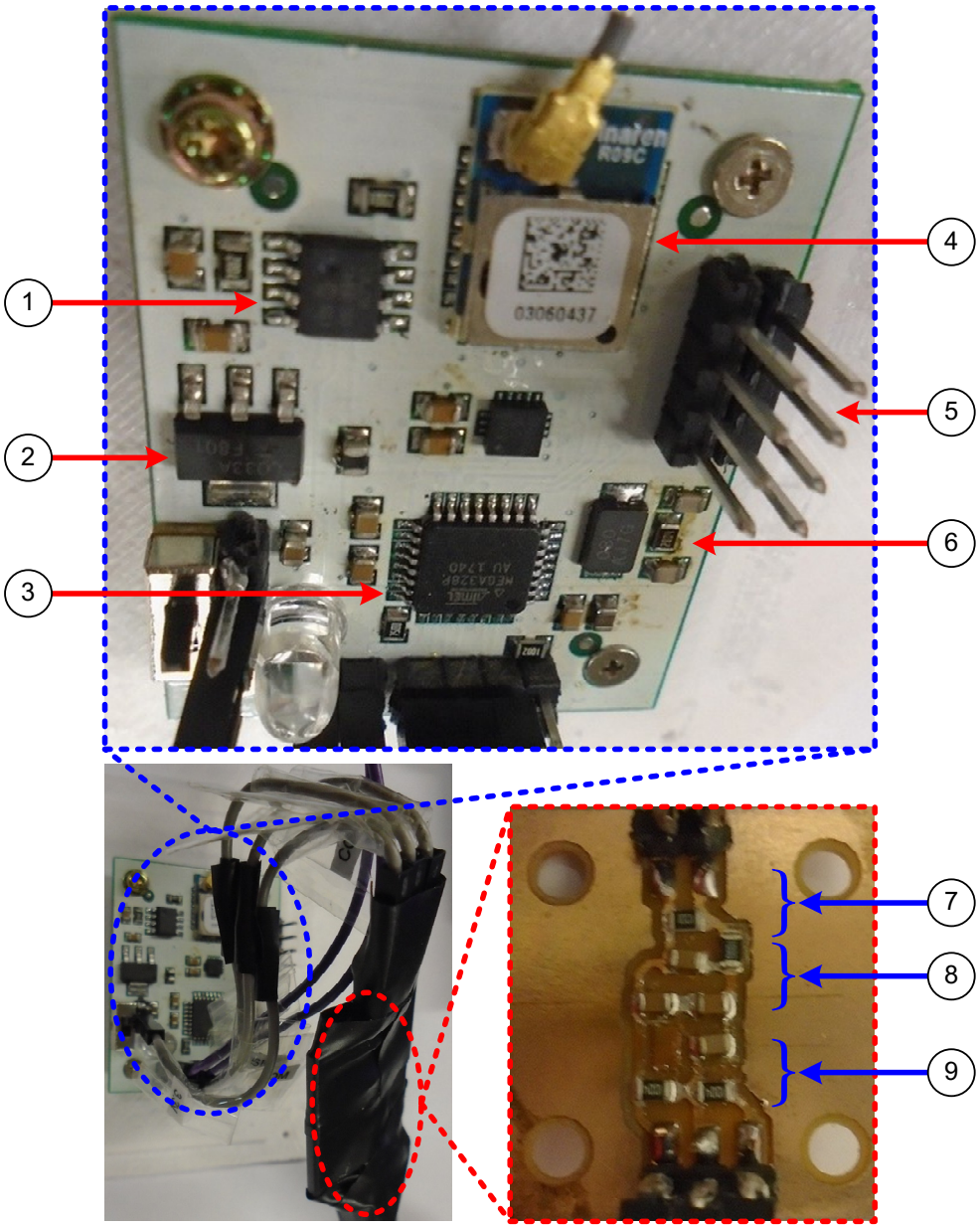

Fig. 4.5. Internal PCB of the developed smart sensor prototypes: (1) SRAM chip, (2) voltage regulator, (3) microcontroller, (4) wireless transceiver, (5) SPI device extension pins, (6) external crystal oscillator. serial-to-USB interface chip, (4) voltage regulator, (4) external crystal, (5) USB connector. Signal conditioning PCB: (7) current-to-voltage conversion / amplification, (8) low-pass filter, (9) high-pass filter / biasing circuit. PCB dimensions, smart sensor: 32.97 mm x 49.91 mm, signal conditioning: 25.49 mm x 23.12 mm.

The developed wireless smart sensor DAQ systems consist of current and vibration sensing units. Three current smart sensors are used to collect data from each phase, using +/-100A split-core current transformers (*C-CT-16* from Nidec), which are installed without the need to disconnect any IM power lines. The vibration smart sensor uses a digital +/-2g-to-16g 3D MEMS sensing unit (*LIS3DH* from STMicroelectronics), which is mounted to the IM with an industrial magnet. These sensors are based on the following considerations:

1) The sensing ranges and bandwidth should be compatible with the rated parameters of the IM.
2) The operating voltages should be compatible with the specifications of the MCU and ADC.
3) The smart sensor DAQ system is battery-operated and wireless. This adds limitations on the available power as well as the voltage range for DAQ operations. Power consumption reduction and the appropriate signal conditioning of the transducer signals should be considered in both design and application as per Chapter 2.

Data transmission is initiated wirelessly from four receivers connected to a computing device (e.g., a laptop in this case) via a serial-to-USB converter. A handshake protocol is applied to ensure no data loss through wireless communications; data transmission from the smart sensors is repeated until a confirmation signal is received from the receiver, in the event of a failed transmission.

Five fractional-horsepower IMs (from Marathon Electric Inc.) are tested in this work: two healthy IMs, and three faulted IMs with one, two, and three simulated broken rotor bars, respectively. The tested motor specifications and the test conditions are summarized in Table II and Table III, respectively.

Table II. Motor nameplate specifications (50 Hz, 60 Hz).

Phase	3	**Model Number**	056T34F5301
Poles	2	**Rotor Bars**	34
Output Power	1/3 HP / 248W, 1/2 HP / 372W	**Stator Slots**	24
Supported Line Frequency	50 Hz, 60 Hz	**Rated Voltage**	190V, 200-230V
Full-load Amperage	1.85 A, 2.2 A	**Nominal Full-load r/min**	2850 r/min (47.5 Hz), 3450 r/min (57.5 Hz)

Table III. Summary of test conditions.

VFD Frequency	50 Hz, 60 Hz
Motor Conditions	Healthy, 1-bar, 2-bar, 3-bar defects
Load Levels and approximate torque (N•m)	Zero, minimum, medium, full 50 Hz: 0.793, 0.804, 0.809, 0.814 60 Hz: 0.991, 1.002, 1.009, 1.015
f_R **(@ 50 Hz)**	49.78 Hz, 49.1 Hz, 48.8 Hz, 48.5 Hz
f_R **(@ 60 Hz)**	59.76 Hz, 59.1 Hz, 58.7 Hz, 58.3 Hz
N	64,000
f_s **(Vibration)**	~1000 Hz
f_s **(Current)**	~1000 Hz

Fig. 4.6 illustrates an example of an IM that contains two simulated broken rotor bars.

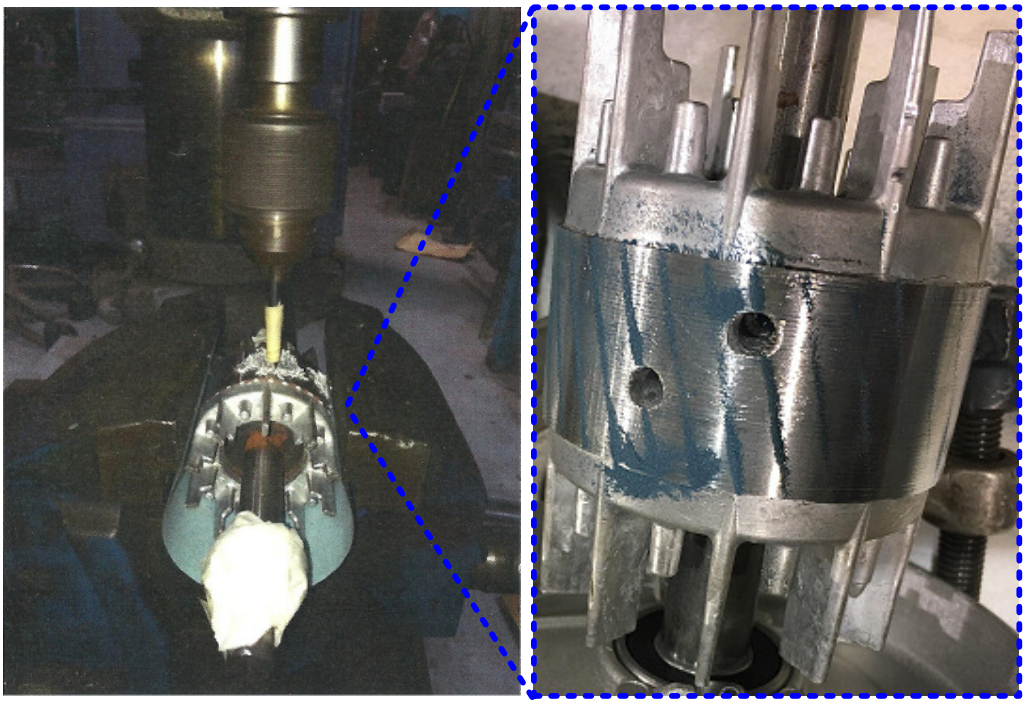

(a) (b)

Fig. 4.6. (a) Introduction of the simulated defects using a drilling machine, [16] (b) example rotor with two simulated broken rotor bars.

The supply frequency of the tested IMs are evaluated at 50 Hz and 60 Hz with a VFD (*VFD-B* from Delta Electronics Inc.), switching at 15 kHz. The IM output shaft is jaw-coupled to a gearbox with 10.11:1 speed reduction ratio (*832B-10K* from Boston Gear). A magnetic particle clutch (*PHC-50* from Placid Industries Inc.) used to provide the load via an external DC power source.

The full load of the IM is determined based on increasing the load from the magnetic clutch until the average 3-phase RMS values of current signals reach their rated full load values [79]. At this full-load condition, the IM rotor speeds (f_R, slip) are 2910 r/min (i.e.: f_R = 48.5 Hz, slip = 3%) at a 50 Hz line frequency, and 3498 r/min (i.e., f_R = 58.3 Hz, slip = 2.83%) at a 60 Hz line frequency. In the motor tests, four load conditions

[16] Drilling conducted by Mahon Electric Ltd. of Thunder Bay, Ontario, Canada (http://mahonelectric.ca).

are considered: decoupled shaft with zero external loads, and coupled shaft with minimum load, medium load, and full load, with the rotor speeds shown in Table III. The minimum load condition is attained by connecting the output shaft to the load, but with a minimal magnetic clutch current applied in order to ensure the same slip across multiple motors.

4.2 Performance Evaluation

4.2.1 General Verification of Smart Sensors

To verify the timing and signal accuracy of smart sensor DAQ, a traditional DAQ board, the *Q4* from Quanser [80], is initially used as a comparison benchmark. The *Q4* has an ADC range of +/-10.0V and a bit resolution of 14-bits. In comparison, the smart sensor DAQ has an ADC range of 0.0V-3.3V and a bit resolution of 10-bits.

For current signal verification, the same *C-CT-16* split-core current transducer with a similar signal conditioning circuit is connected to the *Q4* board, collecting data under the same conditions and bandwidth as the smart current sensor.

For vibration verification, since the digital *LIS3DH* vibration transducer is not able to directly interface with the *Q4*,[17] an analog *ICP 603C01* vibration transducer from PCB Piezotronics [81] is used for comparison, collecting data under the same conditions and bandwidth (with an appropriate signal conditioning circuit) as the smart vibration sensor.

In both of the above comparison tests, the results indicate that identical fault and rotor frequencies are obtained, from the current and vibration spectrum respectively, with a similar SNR.[18] Hence in terms to DAQ timing accuracy and SNR, the smart sensors are determined to be of sufficient accuracy and used to obtain the subsequent results of this work.

4.2.2 Rotor Speed Verification of Smart Vibration Sensor

Further verification of the rotor speed is conducted with a strobe light, where a reflective sticker is attached to the coupling of the motor. The strobe light frequency is

[17] It is theoretically possible to rewrite the Q4 interface software to be compatible with the digital vibration sensor's SPI signals, but that is beyond the scope of this work.
[18] The SNR of the two DAQ systems are not identical, given that the Q4 has a different ADC range and bit resolution than the smart sensor.

adjusted until the sticker appears to be stationary. Under such a condition, the shaft rotation should be identical to the strobe flicker frequency, thereby indicating the rotor frequency. For comparison, the vibration sensor also collects data during the same test with characteristic spectral components analyzed to identify the rotor frequency.

The experimental setup for this test is shown in Fig. 4.7 with results summarized in Table IV and Table V.

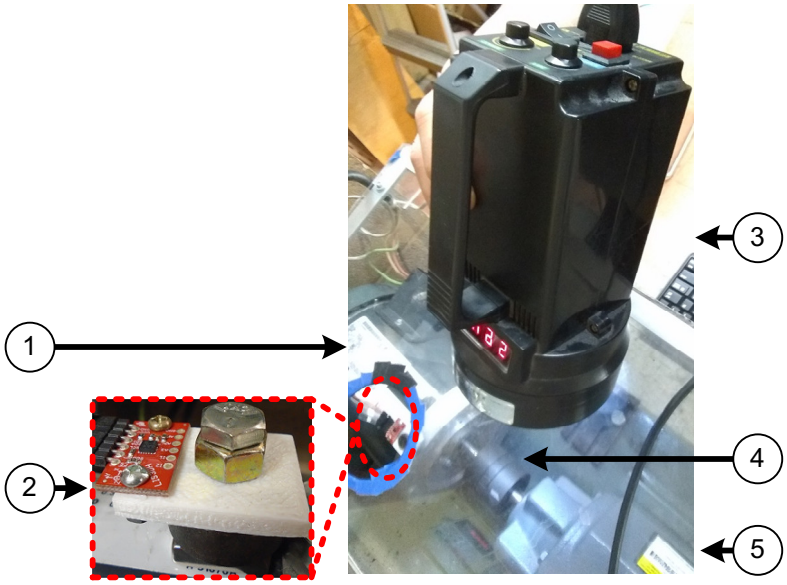

Fig. 4.7. Experimental setup, physical representation: (1) IM under test, (2) smart vibration sensor, (3) strobe light, (4) coupling with reflective sticker attached, (5) speed-reduction gearbox.

The results show a negligible discrepancy between the rotor frequency found by the strobe light and the vibration sensor. Some minor speed variations are observed during the tests with the strobe light, where the reflective tape appeared to oscillate slowly, and indicating slight variations in the rotor speeds. However, these same variations are also detectable from the *IF* analysis of the vibration signal as shown in the next section. Hence, the vibration sensor used in this work is determined to be a reliable indicator of the actual rotor frequency.

Table IV. Rotor frequency verification results, 50 Hz.

Motor Load Condition	Trial	Rotor frequency according to:	
		Strobe Sensor	**Vibration Smart Sensor**
Decoupled	1	49.82 Hz	49.73 Hz
	2	49.80 Hz	49.76 Hz
	3	49.85 Hz	49.74 Hz
	4	49.82 Hz	49.76 Hz
	5	49.80 Hz	49.78 Hz
Low	1	49.10 Hz	49.07 Hz
	2	49.08 Hz	49.07 Hz
	3	49.07 Hz	49.07 Hz
	4	49.07 Hz	49.07 Hz
	5	49.07 Hz	49.07 Hz
Medium	1	48.82 Hz	48.82 Hz
	2	48.83 Hz	48.82 Hz
	3	48.83 Hz	48.82 Hz
	4	48.83 Hz	48.82 Hz
	5	48.85 Hz	48.82 Hz
High	1	48.50 Hz	48.51 Hz
	2	48.50 Hz	48.51 Hz
	3	48.50 Hz	48.51 Hz
	4	48.50 Hz	48.51 Hz
	5	48.50 Hz	48.51 Hz

Table V. Rotor frequency verification results, 60 Hz.

Load Condition	Trial	Rotor frequency according to:	
		Strobe Sensor	**Vibration Smart Sensor**
Decoupled	1	59.82 Hz	59.76 Hz
	2	59.73 Hz	59.76 Hz
	3	59.68 Hz	59.78 Hz
	4	59.70 Hz	59.81 Hz
	5	59.75 Hz	59.73 Hz
Low	1	59.10 Hz	59.09 Hz
	2	59.15 Hz	59.15 Hz
	3	59.13 Hz	59.15 Hz
	4	59.12 Hz	59.15 Hz
	5	59.13 Hz	59.15 Hz
Medium	1	58.67 Hz	58.71 Hz
	2	58.68 Hz	58.71 Hz
	3	58.70 Hz	58.71 Hz
	4	58.60 Hz	58.71 Hz
	5	58.67 Hz	58.71 Hz
High	1	58.23 Hz	58.27 Hz
	2	58.27 Hz	58.27 Hz
	3	58.27 Hz	58.27 Hz
	4	58.25 Hz	58.27 Hz
	5	58.25 Hz	58.27 Hz

4.2.3 Vibration-based Analysis Results

The first step of evaluating the effectiveness of the proposed synergistic feature analysis technique is collecting the vibration signals to estimate the shaft speed. Fig. 4.8(a) and Fig. 4.8(b) show the *IF*s and *IA*s within the BPF band consisting of f_R. Fig. 4.8(c) demonstrates the levels of *IA*s based on a neighboring BPF band, which does not meet the criteria of Eq. (3.27). Since only the relative values between the *IA*s of the BPF bands are of any significance, their amplitude levels are normalized from [0.0,1.0]. Based on this comparison of energy in the BPF bands, it is evident that throughout the entire duration of the sampling, the f_R is confined to a very narrow band, indicating that f_R is consistent and suitable for the subsequent current-based spectral analysis.

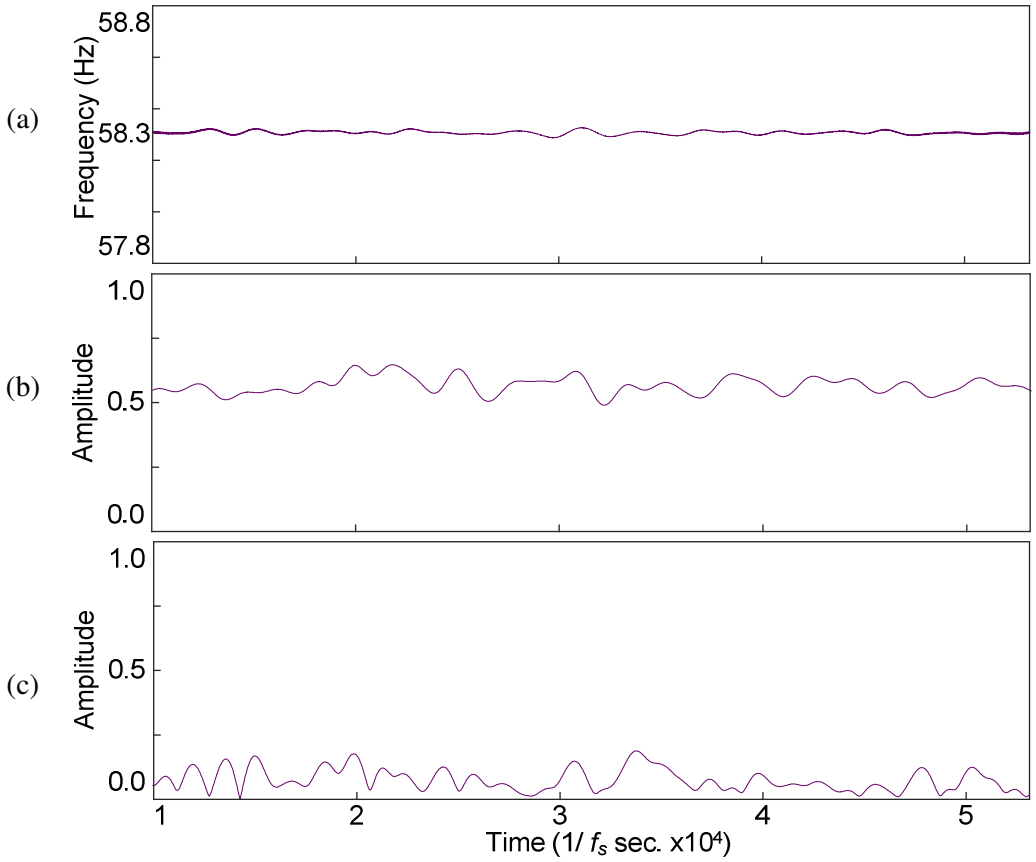

Fig. 4.8. Processing results of vibration signals from a motor with 3 broken rotor bars at full load: (a) *IF* of f_R; (b) *IA* of a BPF signal centered at the rotor frequency; (c) *IA* of a BPF signal of an adjacent band.

4.2.4 Current-based Analysis Results

Fig. 4.9 to Fig. 4.12 illustrate typical processing results from one phase of the current at 60 Hz, depicting features of a motor with three broken rotor bars (3B) and a healthy motor (H1), under zero-load (decoupled shaft), minimum load, medium load, and full load, respectively. The results are around f_L and the corresponding 5th and 7th harmonics. The arrows indicate the predicted fault characteristic frequencies, as per Eq. (3.5)-(3.6), and Eq. (3.8)-(3.10). The red dashed line indicates the estimated noise floor, as per Eq. (3.29). It is seen from Fig. 4.9 to Fig. 4.12 that under all IM load conditions (i.e., from the decoupled no-load state to the full-load state), there are obvious differences between the healthy and faulted motors. Under no-load, smaller fault frequency components can still be observed at the measured stator current due to a smaller current induced in the rotor compared to loaded conditions.

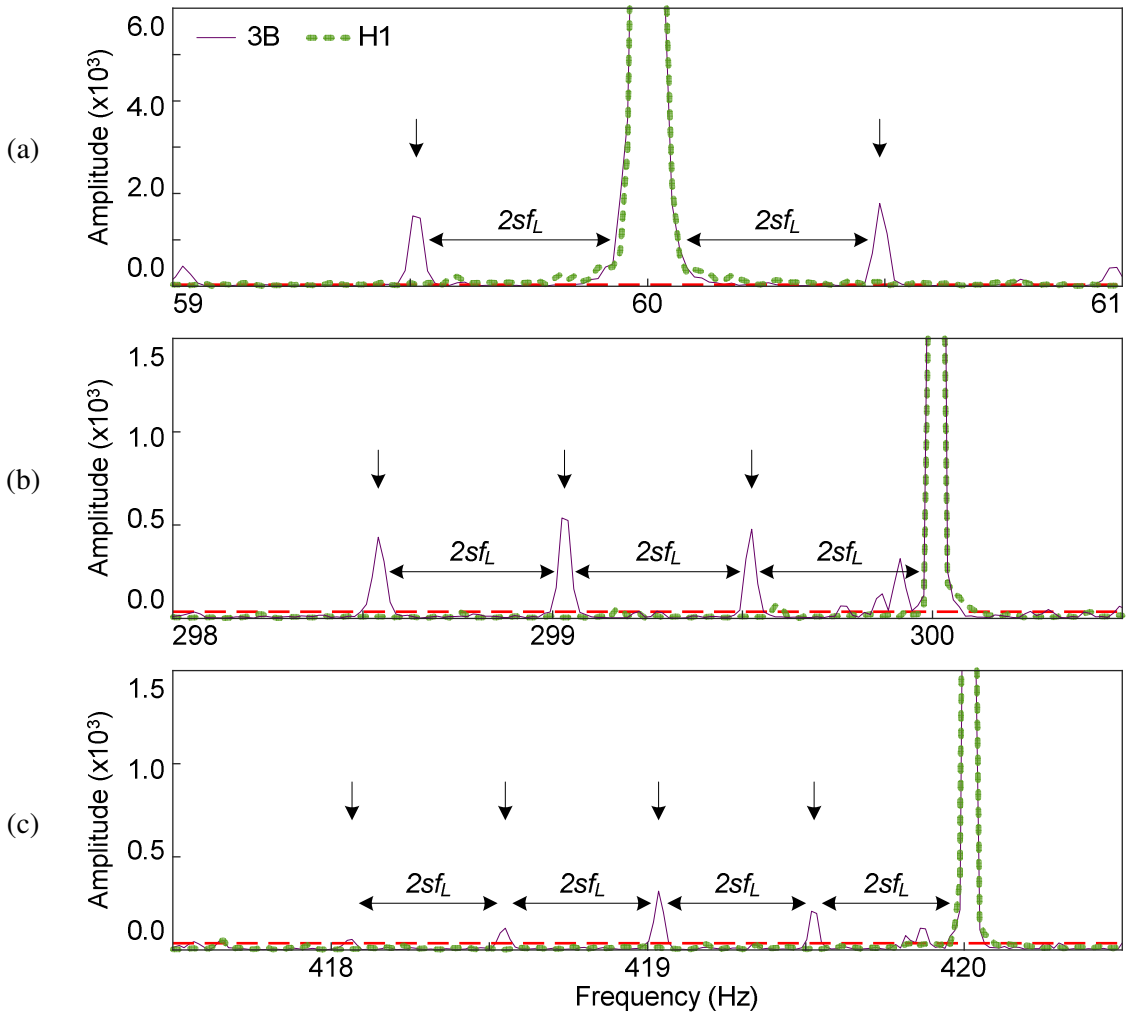

Fig. 4.9. Current results at 60 Hz under a decoupled zero-load condition for an IM with three broken rotor bars (purple, solid), and a healthy motor (green, dashed) at: (a) fundamental line frequency; (b) 5th harmonic; (c) 7th harmonic.

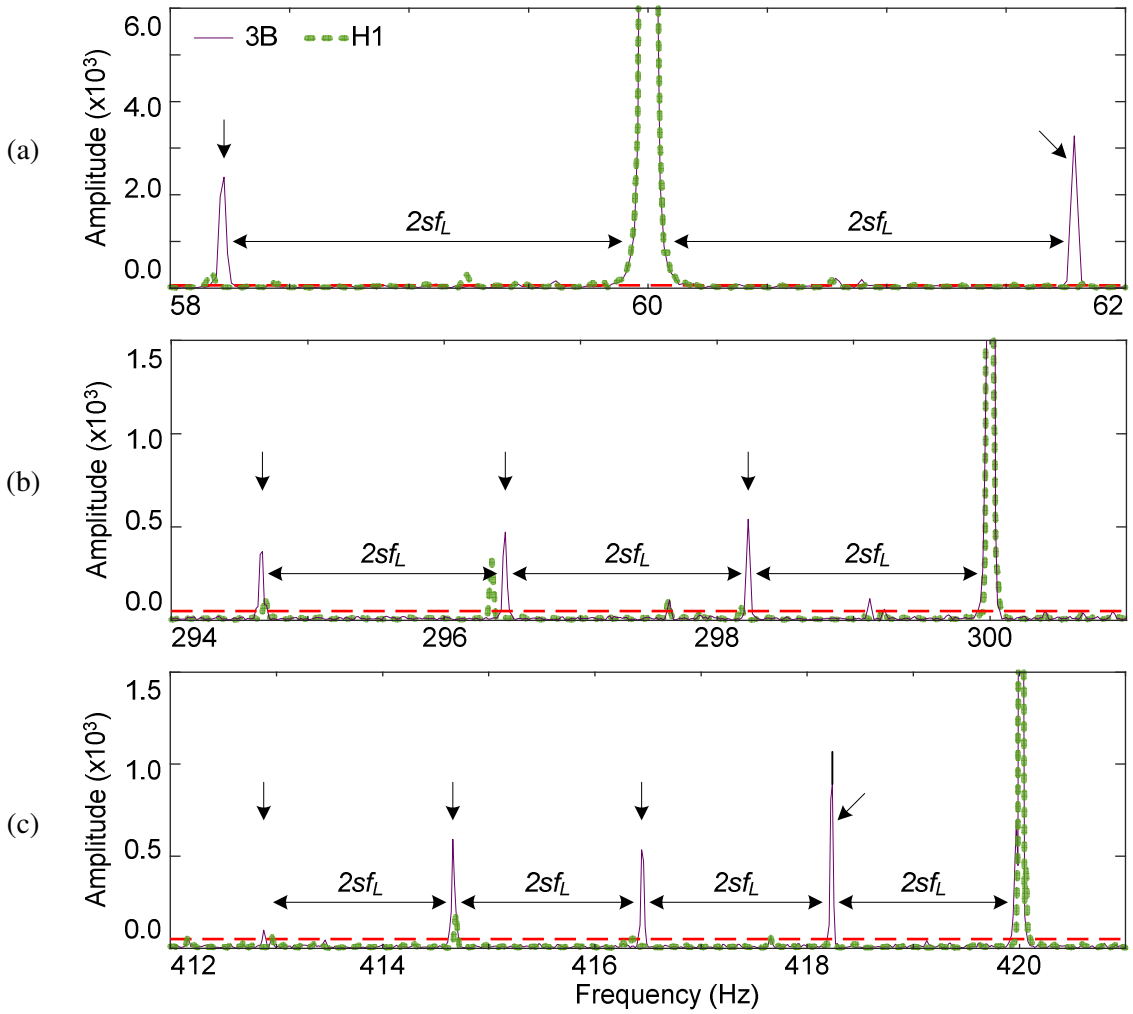

Fig. 4.10. Current results at 60 Hz under a low load condition for an IM with three broken rotor bars (purple, solid), and a healthy motor (green, dashed) at: (a) fundamental line frequency; (b) 5th harmonic; (c) 7th harmonic.

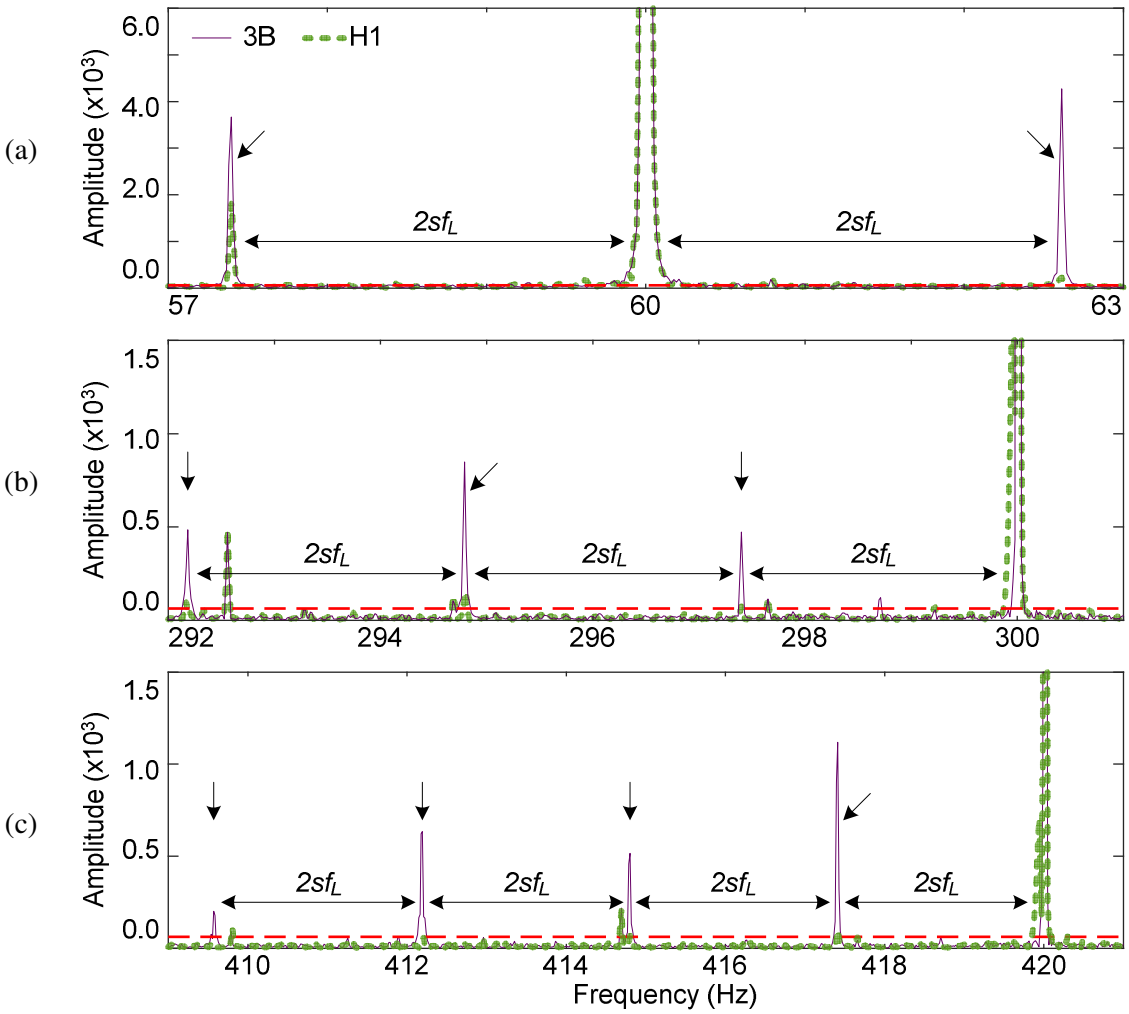

Fig. 4.11. Current results at 60 Hz under a medium load condition for an IM with three broken rotor bars (purple, solid), and a healthy motor (green, dashed) at: (a) fundamental line frequency; (b) 5th harmonic; (c) 7th harmonic.

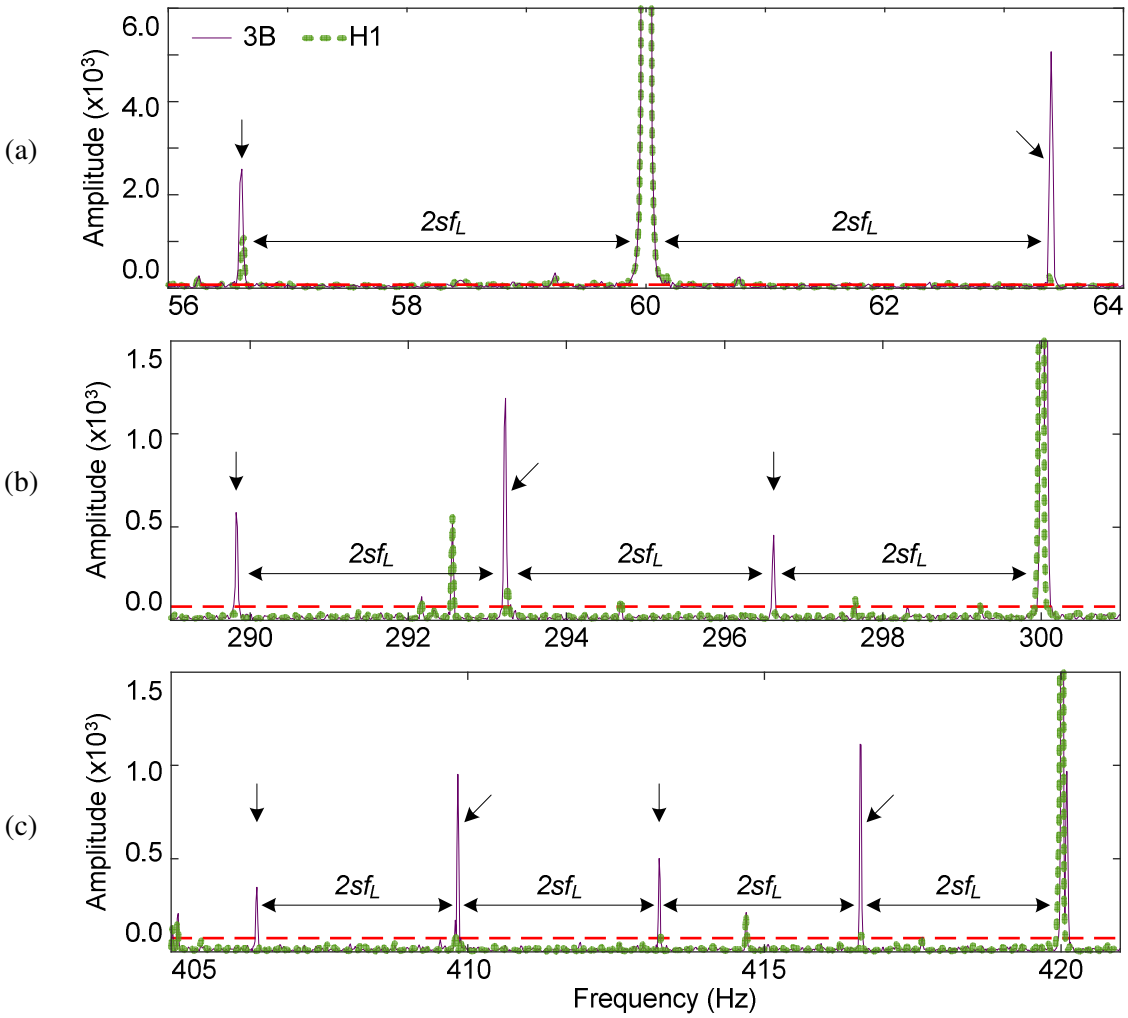

Fig. 4.12. Current results at 60 Hz under a full load condition for an IM with three broken rotor bars (purple, solid), and a healthy motor (green, dashed) at: (a) fundamental line frequency; (b) 5th harmonic; (c) 7th harmonic.

4.2.5 Post-processing for Monitoring Index Formulation

For every test condition, current data for each phase along with the vibration are collected ten times. The results of the fault index quantification are shown in Fig. 4.13 and Fig. 4.14, and enumerated on Table VI and Table VII, where 3B, 2B, 1B, H2, H1 represent the IM with three-, two-, and one-rotor bar faults, as well as two healthy motors, respectively. The sideband-based broken bar fault index $F_{I,1}$ is used as a comparison and calculated by [37]:

$$F_{I,1} = F_I\left(f_{bb,sb-}\right) + F_I\left(f_{bb,sb+}\right) \tag{4.1}$$

For the testing under load, comparing the evaluated frequencies of Eq. (4.1) with the gear-mesh speed oscillation frequencies of Eq. (3.7), the results of $F_{I,1}$ are not modulated by such unrelated frequencies.

Other results for comparison include those based on 5th and 7th magnetomotive force space harmonics from Eq. (3.8)-(3.9), where:

$$F_{I,2} = \max\left\{F_I[f_{bb}(5,s)], F_I[f_{bb}(7,s)]\right\} \tag{4.2}$$

The proposed $2sf_L$-fold-based fault frequencies from Eq. (3.10) is formulated as a fault index by:

$$F_{I,3} = \text{mean}\left(F_{I,2}, F_I[\max\left(f_{bb,gen}\right)]\right) \tag{4.3}$$

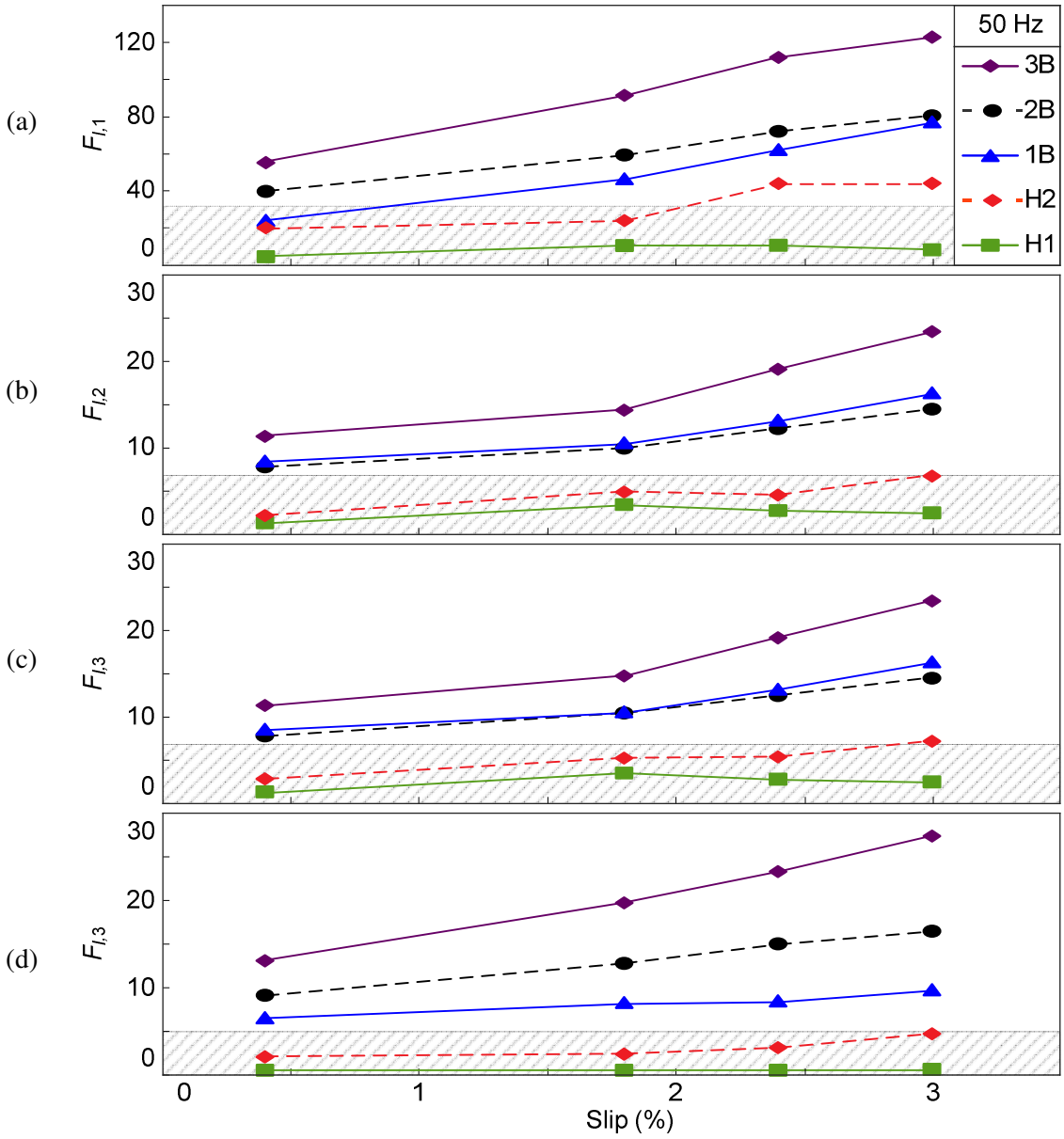

Fig. 4.13. F_I results at 50 Hz, based on the following methods: (a) addition of sidebands around the fundamental frequency (averaged results); (b) max MMF from either the 5th or 7th harmonic (averaged results); (c) max $2sf_L$ multiple from either the 5th or 7th harmonic (averaged results); (d) max $2sf_L$ multiple from either the 5th or 7th harmonic (best results).

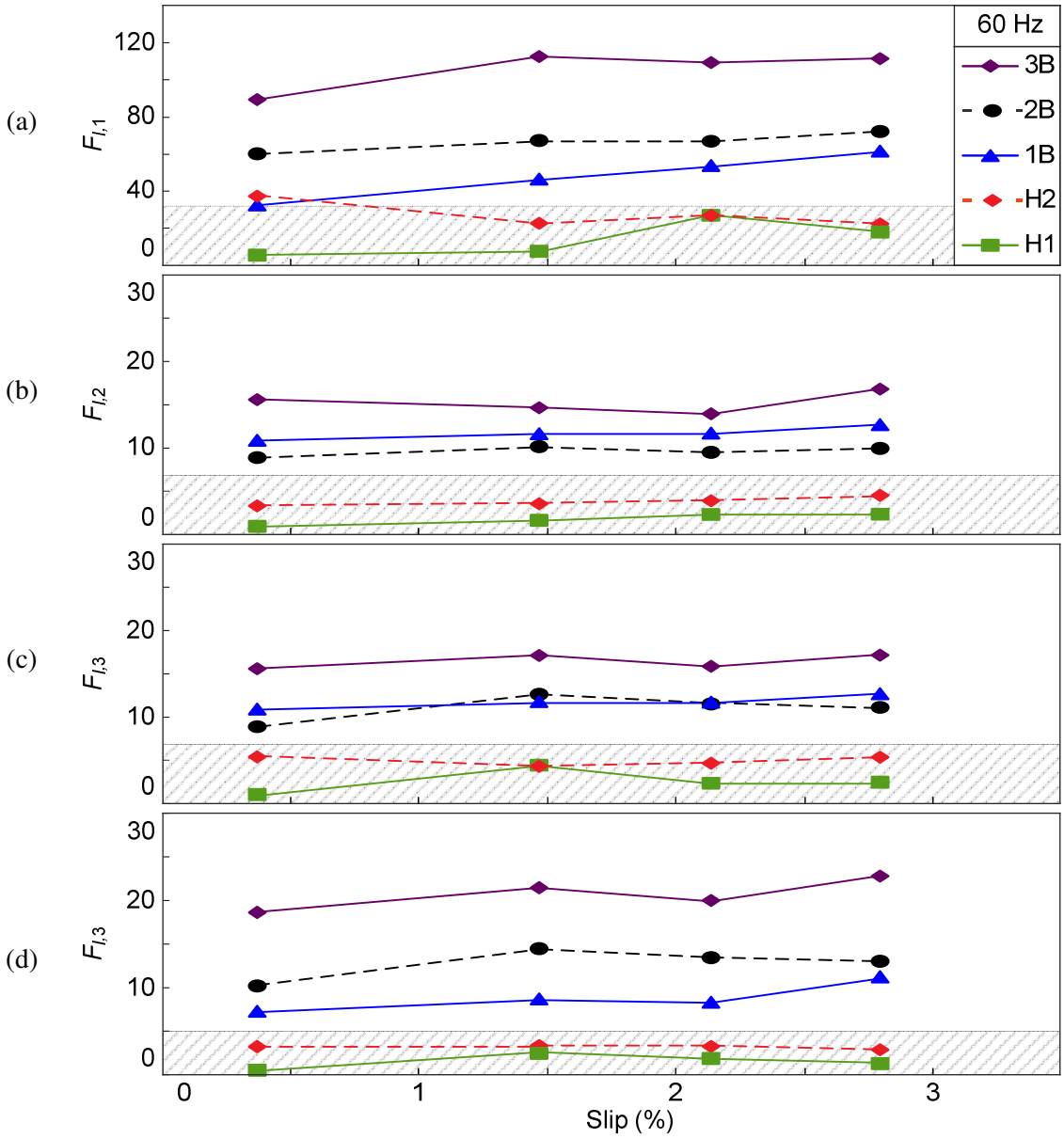

Fig. 4.14. F_I results at 60 Hz, based on the following methods: (a) addition of sidebands around the fundamental frequency (averaged results); (b) max MMF from either the 5th or 7th harmonic (averaged results); (c) max $2sf_L$ multiple from either the 5th or 7th harmonic (averaged results); (d) max $2sf_L$ multiple from either the 5th or 7th harmonic (best results).

Table VI. Summary of results per technique at 50 Hz, averaged over 10 data sets, expressed in terms of average and standard deviation (std) respectively.

Fault Detection Technique	**Tested Motor**	**Load levels,** Average (*std*)			
		Decoupled	Low	Medium	High
$F_{I,1}$ Sideband-based from [36,37,38]	H1	4.60 (*1.40*)	10.53 (*1.87*)	10.74 (*2.48*)	8.35 (*2.37*)
	H2	20.14 (*2.11*)	24.08 (*6.14*)	43.93 (*8.08*)	44.06 (*9.23*)
	1B	24.90 (*3.66*)	46.54 (*13.89*)	62.32 (*19.05*)	77.22 (*17.03*)
	2B	39.71 (*3.08*)	59.40 (*7.82*)	72.07 (*17.01*)	80.48 (*11.71*)
	3B	55.25 (*5.89*)	91.41 (*7.11*)	111.95 (*15.82*)	122.84 (*13.19*)
$F_{I,2}$ Magneto-motive-force-based from [6,28]	H1	1.35 (*0.33*)	3.46 (*2.21*)	2.77 (*2.05*)	2.51 (*1.26*)
	H2	2.20 (*0.42*)	4.90 (*2.39*)	4.57 (*1.54*)	6.76 (*2.73*)
	1B	8.49 (*1.12*)	10.61 (*1.38*)	13.23 (*3.05*)	16.39 (*5.25*)
	2B	7.83 (*0.89*)	9.99 (*1.89*)	12.23 (*1.55*)	14.49 (*1.02*)
	3B	11.36 (*1.01*)	14.37 (*3.04*)	19.12 (*2.67*)	23.44 (*2.32*)
The proposed $F_{I,3}$ $2sf_L$ -based	H1	1.35 (*0.32*)	3.54 (*2.01*)	2.82 (*1.90*)	2.51 (*1.26*)
	H2	2.86 (*0.59*)	5.25 (*1.40*)	5.41 (*1.25*)	7.20 (*2.15*)
	1B	8.60 (*0.97*)	10.61 (*1.38*)	13.23 (*3.05*)	16.40 (*5.25*)
	2B	7.83 (*0.89*)	10.46 (*0.92*)	12.48 (*1.20*)	14.49 (*1.02*)
	3B	11.36 (*1.01*)	14.75 (*2.41*)	19.16 (*2.53*)	23.42 (*2.34*)

Table VII. Summary of results per technique at 60 Hz, averaged over 10 data sets, expressed in terms of average and standard deviation (std) respectively.

Fault Detection Technique	**Tested Motor**	**Load levels,** Average (*std*)			
		Decoupled	Low	Medium	High
$F_{I,1}$ Sideband-based from [36,37,38]	H1	5.32 (*1.93*)	7.53 (*2.20*)	26.85 (*3.41*)	17.84 (*2.14*)
	H2	37.32 (*5.58*)	22.51 (*10.07*)	26.73 (*9.32*)	22.29 (*8.75*)
	1B	32.49 (*2.88*)	46.40 (*8.00*)	53.71 (*9.33*)	61.50 (*14.74*)
	2B	59.98 (*3.51*)	67.16 (*6.40*)	66.74 (*18.64*)	72.06 (*14.36*)
	3B	89.18 (*7.47*)	112.67 (*4.14*)	109.10 (*17.50*)	111.20 (*14.45*)
$F_{I,2}$ Magneto-motive-force-based from [6,28]	H1	0.96 (*0.42*)	4.45 (*1.32*)	2.32 (*0.35*)	2.35 (*1.13*)
	H2	3.32 (*0.96*)	3.56 (*0.96*)	3.90 (*1.25*)	4.54 (*2.32*)
	1B	10.89 (*2.50*)	11.65 (*1.88*)	11.74 (*1.98*)	12.71 (*0.77*)
	2B	8.89 (*1.03*)	10.15 (*1.49*)	9.50 (*2.32*)	9.97 (*1.63*)
	3B	15.60 (*1.96*)	14.66 (*4.27*)	13.96 (*3.23*)	16.79 (*2.92*)
The proposed $F_{I,3}$ $2sf_L$ -based	H1	1.05 (*0.23*)	4.45 (*1.32*)	2.35 (*0.38*)	2.47 (*0.90*)
	H2	5.41 (*0.98*)	4.32 (*0.46*)	4.66 (*0.61*)	5.37 (*1.05*)
	1B	10.94 (*2.38*)	11.79 (*1.52*)	11.74 (*1.98*)	12.71 (*0.77*)
	2B	8.89 (*1.03*)	12.62 (*1.24*)	11.51 (*2.17*)	11.12 (*1.80*)
	3B	15.60 (*1.96*)	17.12 (*1.28*)	15.87 (*1.71*)	17.14 (*2.61*)

4.2.6 Results Discussion

Fig. 4.13(a)-(c) and Fig. 4.14(a)-(c) compare the average $F_{I,1}$, $F_{I,2}$ and $F_{I,3}$ indices, averaged over ten results, in IM fault detection and severity assessment. To facilitate visual inspection, a horizontal line is drawn to subjectively classify the healthy and faulty states. This line can facilitate IM diagnosis, since a constant threshold can be defined without to the requirement to test at all load conditions. As seen in Fig. 4.13(a) and Fig. 4.14(a), although $F_{I,1}$ generates clear distinction of fault severity under the zero-load (little slip) condition, it misses alarms without recognizing the IM fault with the 1B condition due to weak feature modulations. Similarly, at 60 Hz, there is a false alarm at the zero-load condition.

Examining Fig. 4.13(b)(c) and Fig. 4.14(b)(c), it is seen that both the averaged $F_{I,2}$ and $F_{I,3}$ generate no false or missed alarms under the same zero-load conditions; it indicates that the integration of higher harmonics during processing can better characterize actual motor conditions. Moreover, due to the integration of these higher 5th and 7th harmonics, $F_{I,2}$ and $F_{I,3}$ are much less susceptible to the gear-mesh speed oscillation than $F_{I,1}$ and hence are more applicable to IM health condition monitoring.

On the other hand, it is evident from Fig. 4.13(b) and Fig. 4.14(b) that $F_{I,2}$ cannot accurately diagnose the severity of faults between the 1B and 2B conditions. In contrast, Fig. 4.13(c) and Fig. 4.14(c) demonstrate that $F_{I,3}$ outperforms $F_{I,2}$ in rotor bar fault severity assessment between the same 1B and 2B conditions. This result suggests that the choices of fault features used in $F_{I,3}$, as per Eq. (3.10), can result in a more accurate diagnosis than the comparatively limited choices of fault features used in $F_{I,2}$, as per Eq. (3.8)-(3.9).

Table VIII summarizes some visual diagnostic results. With the above considerations, the proposed $F_{I,3}$ fault index can provide the best overall diagnostic accuracy.

Table VIII. Comparison of diagnostic clarity.

Fault index	Differentiate healthy vs. faulty	Differentiate fault severity
$F_{I,1}$ (comparison)	Least clear	Very clear
$F_{I,2}$ (comparison)	Very clear	Least clear
$F_{I,3}$ (proposed)	Clear	Clear

4.2.7 Fault Indices Results Additional Discussion

An additional observation in the results of Fig. 4.13(a)-(c) and Fig. 4.14(a)-(c) is that the 1-bar and 2-bar fault indices are often very similar to one another, which increases the difficulty in determining the fault severity. A likely explanation for this similarity is due the influence of location of the faulted rotor bars on the fault severity results [82,83], which can be a subject of further investigation.

It is noted that Fig. 4.13(a)-(c) and Fig. 4.14(a)-(c) represent an average of ten results. To demonstrate the potential of the proposed fault detection technique, the best results are shown in Fig. 4.13(d) and Fig. 4.14(d), which indicate that under ideal circumstances, the proposed synergistic analysis technique can provide very clear diagnostic results in both fault detection and fault severity assessment. It has a potential to be used in real-world IM health condition monitoring applications.

CHAPTER 5

An Evolving Fuzzy Classifier for IM Health Condition Monitoring

5.1 Brief Background

As stated in Section 1.7.1, the goal of a diagnostic classifier for condition monitoring is to classify the representative features (input patterns) obtained by the use of the related fault detection techniques into different categories corresponding to different IM health conditions, as depicted in Fig. 1.11(b). Classifiers with transparent decision-making schemes such as the fuzzy inference system (FIS) have disadvantages with requiring system-specific parameters being set by expertise, which cannot always be optimal and generalized to other systems. ANFIS systems [46,47] on the other hand, have limitations regarding to error control, and adaptability to time-varying system dynamics. Evolving fuzzy classifiers [48,49,50] have limitations related to data clustering and its ability to generate an adequate number of rules to describe the overall output classifications. Hence, this work develops a new evolving fuzzy classifier to address the aforementioned problems.

5.2 Overview

In this work, the input data to the classifier are monitoring indices formulated from the related fault detection techniques as discussed in Section 4.2.5. The output is an indicator corresponding to a motor condition, such as, 1 = "healthy", 2 = "faulty", etc. A first-order Takagi-Kang-Sugeno (TSK-1) fuzzy inference architecture is selected as the reasoning platform in this proposed evolving fuzzy classifier, due to its ability to efficiently model data [52,84].[19] For such an intelligent system to be functional, two general processes must be completed, as illustrated in Fig. 5.1:

- **Training phase:** Uses available training data pairs[20] to formulate a fuzzy model and update the system's parameters.

---

[19] Compared with a zero-order Takagi-Kang-Sugeno model, where outputs are strictly defined by constants and have limitations with non-linear approximations, and a Mamdani model where the output is determined by a computationally-intensive fuzzy set [86,89].

[20] A data pair consists of an input and a known corresponding output.

- **Testing phase** (performance evaluation)**:** Check the accuracy of the recognized fuzzy model from a set of testing data pairs.

5.2.1 Contributions

The contributions in this aspect of the work include the following:

1) An updated clustering algorithm for an evolving fuzzy system.
2) Implementation of the developed evolving fuzzy classifier with rotor bar condition monitoring.

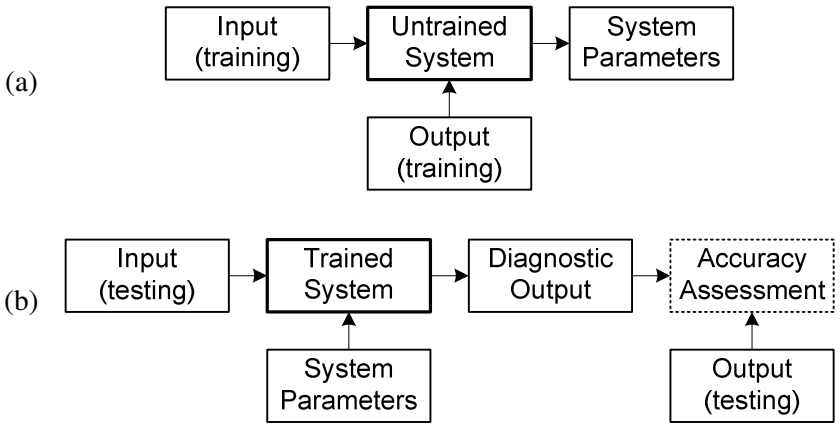

Fig. 5.1. Training and testing phases of an evolving fuzzy classifier: (a) training phase, (b) testing phase.

5.3 System Training Overview

The procedure for training an evolving fuzzy system is shown in Fig. 5.2, and is graphically illustrated in Fig. 5.3.

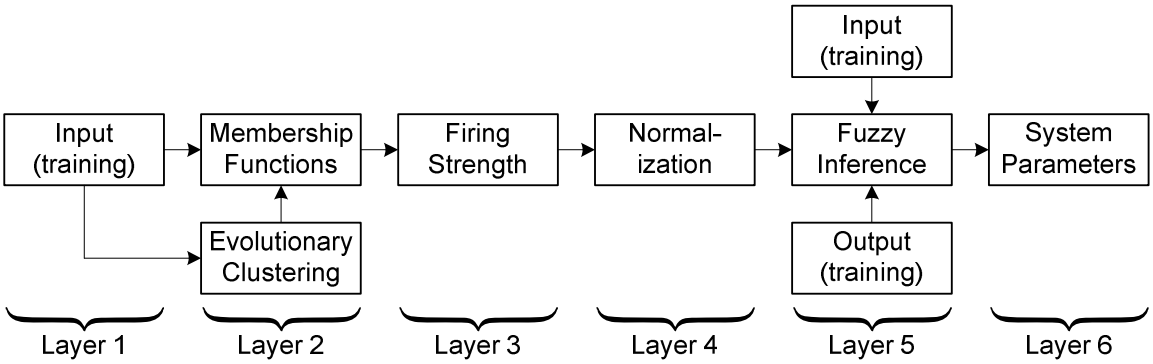

Fig. 5.2. Training with respect to system layers.

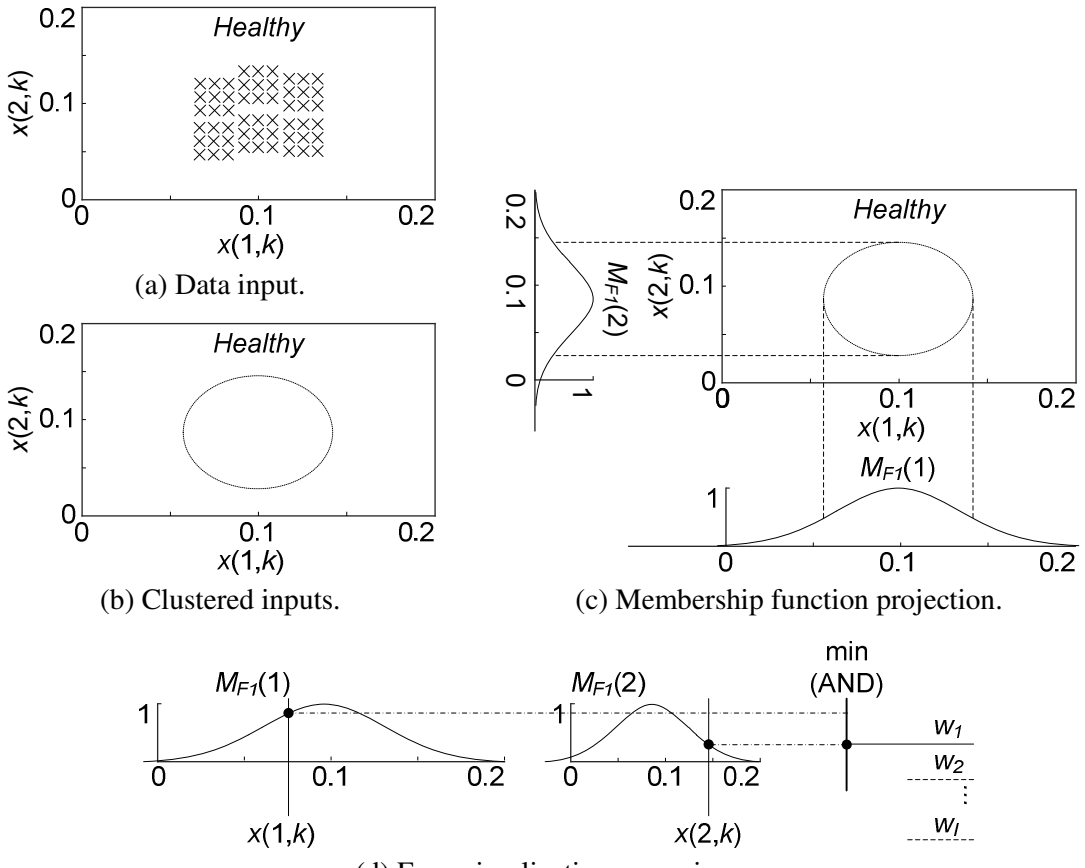

Fig. 5.3. Graphical illustrations of the system training process: (a) original input data, (b) clustering of input data, (c) membership function projection based on clusters, (d) fuzzy implication reasoning.

The training procedures can be described in the following steps:

1) Cluster inputs with an evolutionary algorithm, as per Fig. 5.3(a)(b).

2) Project clusters into fuzzy membership functions, as per Fig. 5.3(c).

3) Process inputs with membership functions to determine each rule's firing strength, as per Fig. 5.3(d).

4) Normalize all firing strengths, as a measure of the rules' contributions to the final output.

5) Formulate an input matrix by multiplying normalized firing strengths and inputs into a TSK-1 model.

6) Update the TSK-1 consequent parameters using available training data pairs.

Assume that an input to the fuzzy classifier system has the form $x(j,k)$, where $j = 1,2,\ldots J$, and J is the number of dimensions or attributes of the input; $k = 1,2,\ldots,K$ represents the instance of normalized datapoint inputs to the classifier system. Each output class (i.e., healthy motor, faulty motor) corresponds one or more rules in the fuzzy system. As an illustration, consider a fuzzy classifier with only two dimensions or $j = 1,2$. Then the *i*th rule, R_i can be represented as [44,46]:

$$R_i: \quad \begin{array}{cc} \text{IF} & [x(1,k) \text{ is } M_{Fi}(1)] \text{AND} [x(2,k) \text{ is } M_{Fi}(2)] \\ \text{THEN} & y(k) \text{ is } O_i(k) \end{array} \tag{5.1}$$

where $O_i(k)$ is the classifier output of rule R_i; M_{Fi} is a fuzzy membership function representing a degree of belongingness of an input along the *j*th dimension:

$$M_{Fi}(j) \in (0,1] \tag{5.2}$$

Details for obtaining the results of the fuzzy classifier will be discussed in the proceeding sections.

5.3.1 Input Clustering

Fig. 5.3(a) shows an example of inputs used to generate the clusters as illustrated in Fig. 5.3(b). The clustering takes two steps:

1) Evolve cluster centers.
2) Compute cluster spreads after evolution.

The clustering in the input spaces can be achieved with an evolutionary algorithm based data potential, a measure of data density [49]. The potential of a given datapoint can be computed based on the Euclidean distance of the datapoint with respect to all other datapoints, such as:

$$P(k) = \frac{1}{1 + \frac{1}{N}\sum_{a=1}^{N}\sum_{j=1}^{J}\left[x(j,k) - x(j,a)\right]^2} \tag{5.3}$$

where $a = 1,2,\ldots,N$ is an index, and N represents the total number of datapoints.

Based on the principle of Eq. (5.3), a recursive computation of the data potential can be undertaken as [49]:

$$P(k) = \frac{k-1}{\left\{(k-1)\left[1 + \sum_{j=1}^{J}[x(j,k)]^2\right] - 2\sum_{j=1}^{J} x(j,k)\, B(k) + D(k)\right\}} \tag{5.4}$$

where,

$$B(k) = \sum_{a=1}^{k-2} x(j,a) + x(j,k-1) \tag{5.5}$$

and

$$D(k) = \sum_{a=1}^{k-2}\sum_{j=1}^{J}\left[x(j,a)\right]^2 + \sum_{j=1}^{J}\left[x(j,k-1)\right]^2 \tag{5.6}$$

Eq. (5.4)-Eq. (5.6) have been applied to several evolving fuzzy classifiers [50,51,52]. However, its basis on the previous datapoint at $k-1$ may cause problems such as the formed clusters being less accurate because it does not fully reflect the most recent datapoint at k.

To tackle that accuracy problem and improve the representation of the clusters with respect to the data, from a revised derivation of Eq. (5.3), a recursive algorithm of the data potential is proposed in this work as:

$$P(k) = \frac{k}{\left\{k\left[1 + \sum_{j=1}^{J}[x(j,k)]^2\right] - 2\sum_{j=1}^{J} x(j,k)\, B(k) + D(k)\right\}} \tag{5.7}$$

where

$$B(k) = \sum_{a=1}^{k-1} x(j,a) + x(j,k) \tag{5.8}$$

$$D(k) = \sum_{a=1}^{k-1} \sum_{j=1}^{J} [x(j,a)]^2 + \sum_{j=1}^{J} [x(j,k)]^2 \tag{5.9}$$

$B(k)$ and $D(k)$ are variables representing the relationship between the previous datapoints up to $k-1$, and the present data point at k. For implementation, the variables of Eq. (5.8) and Eq. (5.9) can be simplified by using their previous values, rather than a summation of datapoints, [21] or:

$$B(k) = B(k-1) + x(j,k) \tag{5.10}$$

$$D(k) = D(k-1) + \sum_{j=1}^{J} [x(j,k)]^2 \tag{5.11}$$

With Eq. (5.7), Eq. (5.10), and Eq. (5.11), the data potential can be computed recursively, without having to store all datapoints into memory, as is the case in Eq. (5.3). Consequently, such recursive computations can simplify implementation, improve computational efficiency, and make it possible to use in stand-alone condition monitoring applications.

In cluster center identification, from Eq. (5.7), the initial (i.e., the first) cluster center is established at the first datapoint. With subsequent datapoints, the potential of the *m*th existing cluster center can be recursively updated by:

$$P_m(k) = \frac{k}{\left\{ k\left[1 + \sum_{j=1}^{J} [x(j,c_m)]^2 \right] - 2\sum_{j=1}^{J} x(j,c_m)\, B(k) + D(k) \right\}} \tag{5.12}$$

where $x(j,c_m)$ is the datapoint corresponding to a cluster center.

---

[21] i.e., in Eq. (5.8), the previous iteration of the variable $B(k)$ is already equivalent to the current iteration's summation portion of the equation, or $\sum_{a=1}^{k-1} x(j,a) = B(k-1)$.

A new cluster center is established when the data potential at datapoint k, $P(k)$, is larger than the data potential of any other existing cluster center, or $\exists m = 1,2,..: P(k) \geq P_m(k)$. Once the data potential and cluster centers of every datapoint have been computed, the spread is determined with an algorithm (e.g., a scatter-based calculation [85]) expressed as:

$$\sigma_m = \sqrt{\frac{\sum_s \sum_{j=1}^{J} [x(j,c_m) - x(j,s)]^2}{S_d}} \tag{5.13}$$

where S_d is the data scatter, or in other words, the number of datapoints which have the shortest Euclidean distance to a cluster center $x(j,c_m)$. Given any value of k, if an $x(j,k)$ datapoint satisfies such a distance requirement, then $x(j,s) = x(j,k)$. Note that the values of s in $x(j,s)$ depends on the value of k in $x(j,k)$. Accordingly the summation involving s in Eq. (5.13) has indeterminate values.[22] From the known training output data, each cluster center is assigned to its respective class, for example, the cluster center "1" represents a healthy motor condition,"2" represents a faulted motor condition, etc.

Once the initial cluster centers and spreads have been computed, post-processing is undertaken to use these results to generate a single representative cluster per rule.

5.3.2 Membership Function Formulation

To perform fuzzy reasoning, the inputs are fuzzified with Gaussian membership functions, [23] expressed as:

$$M_{Fi}(j) = \exp\left(\frac{-(x(j,k) - x(j,c_m))^2}{2\sigma_m{}^2}\right) \in (0,1] \tag{5.14}$$

---

[22] As an example, s could consist of [3,8,11,17,…, etc.]

[23] Gaussian membership functions have an advantage of having non-zero values for all values of inputs from (-∞,+∞). This property ensures that all unique inputs will having unique firing strengths and ensures every unique input can be considered in the consequent parameter calculations, as will be detailed later.

where $i = 1,2,\ldots,I$ is the rule associated with a cluster. From Eq. (5.14), the membership functions are derived from the cluster centers and spreads, with an example illustrated in Fig. 5.3(c).

5.3.3 Firing Strength

To implement the fuzzy reasoning structure of Eq. (5.1), the firing strength of the *i*th rule, $w_i(k)$ is as follows:

$$w_i(k) = \min\{ M_{Fi}(1), M_{Fi}(2), \ldots, M_{Fi}(J) \} \tag{5.15}$$

where the min operator is a fuzzy t-norm operator (e.g.: AND) [86], with a simplified illustration shown in Fig. 5.3(d).

5.3.4 Consequent Parameters for the Evolving Fuzzy Inference System

The output of the classifier system, $O(k)$, is computed as:

$$O(k) = \sum_{i=1}^{i=I} \{ \overline{w}_i(k)\ f_i[x(j,k)] \} \tag{5.16}$$

where $\overline{w}_i(k) = w_i(k) / \sum_{i=1}^{I} w_i(k)$ is the normalized firing strength, which represents the contribution of the firing strength of the *i*th rule to the output. f_i is the TSK-1 consequent function of the *i*th rule, represented as:

$$f_i[x(j,k)] = C_{i0} + \sum_{j=1}^{J} x(j,k) C_{ij} \tag{5.17}$$

where $C_{i0}, C_{i1}, \ldots, C_{iJ}$ are the consequent parameters of the *i*th rule of the classifier. Since these linear consequent parameters are unknown, they can be estimated by a training algorithm. For example, if $T(k)$, is the target of the *k*th, training data pair, [24] then:

$$T(k) = \sum_{i=1}^{i=I} \{ \overline{w}_i(k)\ f_i[x(j,k)] \} \tag{5.18}$$

which can be expanded to,

---

[24] Training data pairs are, known target outputs, correspondingly paired to a given input in the training data.

$$T(k)=\begin{bmatrix} \overline{w}_1(k) \\ \overline{w}_1 x(1,k) \\ \overline{w}_1 x(2,k) \\ \vdots \\ \overline{w}_1 x(J,k) \\ \vdots \\ \overline{w}_I(k) \\ \overline{w}_I x(1,k) \\ \overline{w}_I x(2,k) \\ \vdots \\ \overline{w}_I x(J,k) \end{bmatrix}^T \begin{bmatrix} C_{10} \\ C_{11} \\ C_{12} \\ \vdots \\ C_{1J} \\ \vdots \\ C_{I0} \\ C_{I1} \\ C_{I2} \\ \vdots \\ C_{IJ} \end{bmatrix} \qquad k=1,2,\ldots,K \tag{5.19}$$

where K is the total number of training data pairs. Eq. (5.19) can be represented in a matrix/vector form:

$$\vec{T}=\mathbf{Z}\,\vec{C} \tag{5.20}$$

where $\vec{T}$, $\mathbf{Z}$, and $\vec{C}$ are the target vector, input matrix, and consequent parameter vector, respectively. Since $\mathbf{Z}$ is likely a non-square matrix where the inverse may not be computed directly, the singular value decomposition (SVD) will used to solve for $\vec{C}$. The SVD breaks down the $\mathbf{Z}$ matrix into three components:

$$\mathbf{Z}=UDV^T \tag{5.21}$$

where U and V are the respective left and right singular values, and D are the singular eigenvalues of $\mathbf{Z}$. From Eq. (5.21), the Moore-Penrose pseudo-inverse [87] is computed by,

$$\mathbf{Z}^+=VD^+U^T \tag{5.22}$$

where D^+ is the reciprocal of all non-zero elements of D.

With Eq. (5.22), the consequent parameters $\vec{C}$ can then estimated by:

$$\mathbf{Z}^+\,\vec{T}=\mathbf{Z}^+\mathbf{Z}\vec{C}\cong\vec{C} \tag{5.23}$$

5.4 Performance Evaluation Overview

The testing phase of the evolving fuzzy classifier is illustrated in Fig. 5.4, using the estimated consequent parameters of Eq. (5.23).

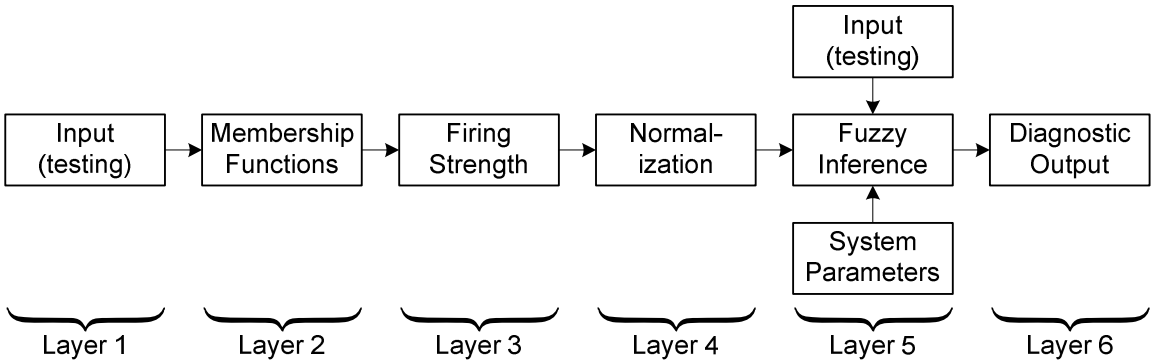

Fig. 5.4. Testing phase, system layers.

To determine the effectiveness of this classifier, the classifier is assessed with datasets associated with simulation and implementation.

- **Simulation:** Uses the two iris and wine datasets [88], which are well-known datasets that serve as a benchmark for simulated results.
- **Implementation:** Uses two two rotor fault-based datasets as an implementation case for rotor fault condition monitoring.

The respective simulation and implementation datasets are summarized in Table IX and Table X.

Table IX. Summary of datasets used for simulation.

Dataset	Number of classifications	Number of attributes	Total number of datapoints used
Iris	3	4	150
Wine	3	13	144

Table X. Summary of datasets used for implementation.

Dataset	Number of classifications	Number of attributes	Total number of datapoints used
Rotor bar, 50 Hz	5	3	1000
Rotor bar, 60 Hz	5	3	1000

In the above datasets, ~75% of the data is used for training, with the remaining ~25% for testing. The data is input to the evolving classifier by order of the class, with the same number of samples per class. To avoid order dependencies in the results, data within each class is randomly permutated for every test.

For comparison, variants of both the proposed and evolving fuzzy classifier proposed in [49] will be evaluated. The variants differ primarily based on the requirements to form clusters:

1) **Loose clustering:** New clusters are formed when the data potential is larger than any existing cluster center [50,89].
2) **Strict clustering:** New clusters are formed when the data potential is larger than all existing cluster centers [49,90].

Each dataset is run 100 times across all evolving fuzzy classifiers. Some of the evaluation metrics are described as follows:

- **Accuracy:** A measure of percentage of times the output classification of the system match the known classification of the test data.
- **Number of clusters:** The number of clusters evolved from the training.
- **Percentage of classes represented:** The percentage of classes represented by the clusters after training.
- **Time / Sample:** The processing time required to produce a resulting classification output for one sample of test data input.

5.4.1 Significance of New Metric

"Percentage of classes represented" is a new metric that is not typically presented in other works, but remains critical for a condition monitoring system to assess false and missed alarms.

Due to the randomized input data for each test, the datapoints that will become cluster centers are not known in advance, nor can the same datapoints always become a cluster center. Because of this uncertainty, there can be some test runs where the resulting clusters do not completely represent all the possible classifications.

In this case, even though the output accuracy can still be high due to accurate consequent parameter estimation, the lack of classes represented by the clusters after the training can result in a lack of rules describing every class. The lack of rules, in turn, will reduce the transparency of the decisions made by the evolving fuzzy classifier. A classifier exhibiting this drawback makes it less suitable for condition monitoring since false or missed alarms cannot be investigated based an incomplete fuzzy reasoning model.

5.4.2 Classifiers used for Comparison

The classifiers evaluated will be represented as follows:

- #1: The proposed classifier using the revised clustering algorithm and a loose clustering variant.
- #2: A comparison classifier, using the revised clustering algorithm and a strict clustering scheme.
- #3: A comparison classifier using the original clustering algorithm and a loose clustering scheme.
- #4: A comparison classifier using the original clustering algorithm and a strict clustering scheme.

5.5 Performance Evaluation, Iris Dataset (Simulation)

5.5.1 Clustering and Identified Fuzzy Model

The inputs and expected outputs of the iris dataset are as follows:

- ***Inputs*:** Four physical measurements of the flower's sepal length, sepal width, petal length, and petal width, corresponding to the system inputs of $x(1,k)$, $x(2,k)$, $x(3,k)$, and $x(4,k)$, respectively.
- ***Outputs*:** Three different iris flower type classifications of setosa, virginica, and veriscolor, corresponding to the system outputs of 1, 2, and 3 respectively.

The data and clustering across all attributes in one representative trial with the iris dataset are shown in Fig. 5.5. It can be observed that the clusters closely correspond to the original data, showing clear distinctions between the different classes. Based on these clustering results, the corresponding recognized fuzzy model is shown in Fig. 5.6.

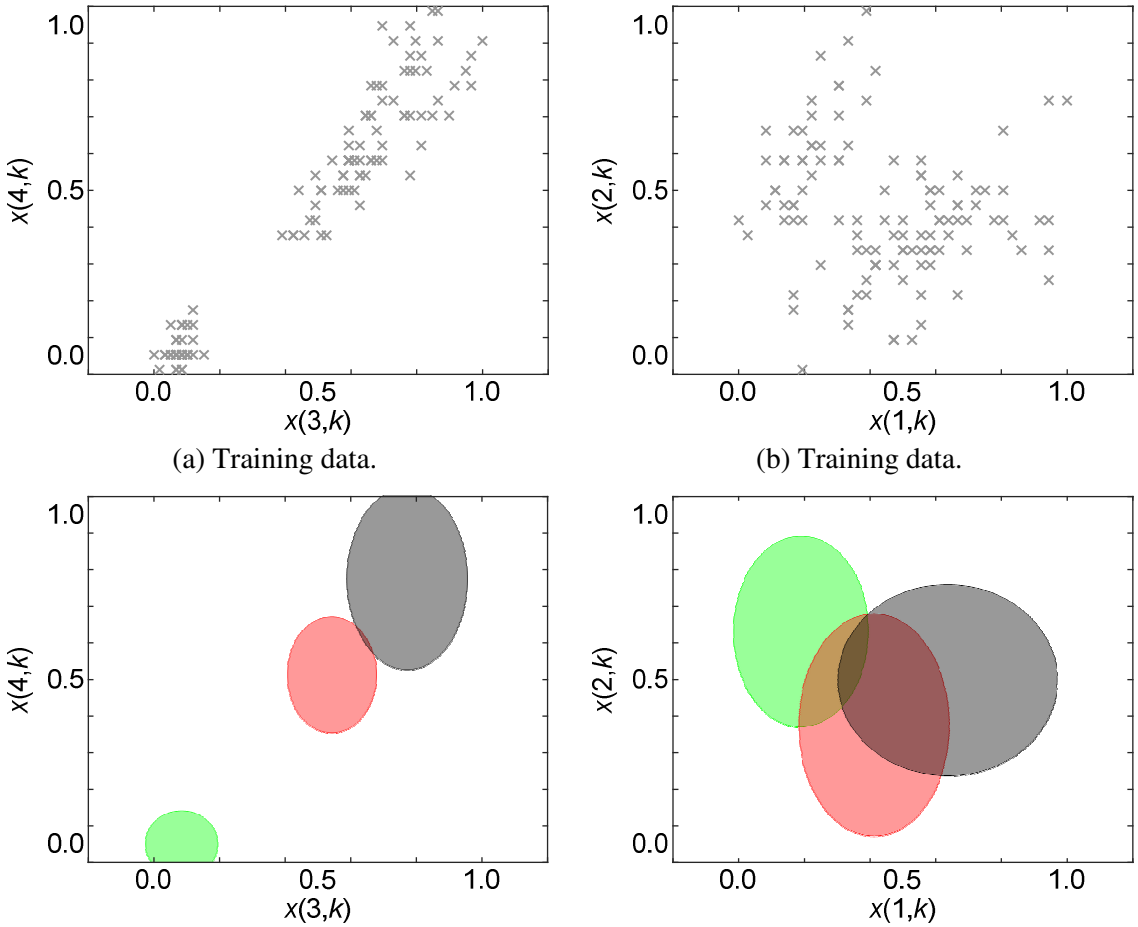

(a) Training data. (b) Training data.

(c) Resultant clusters. (d) Resultant clusters.

Fig. 5.5. Training data (a-b) and clustering results (c-d) of iris data, where green, red and black correspond to flower types of setosa, veriscolor and virginica, respectively; $x(1,k)$, $x(2,k)$, $x(3,k)$ and $x(4,k)$ represent sepal length, sepal width, petal length, and petal width respectively.

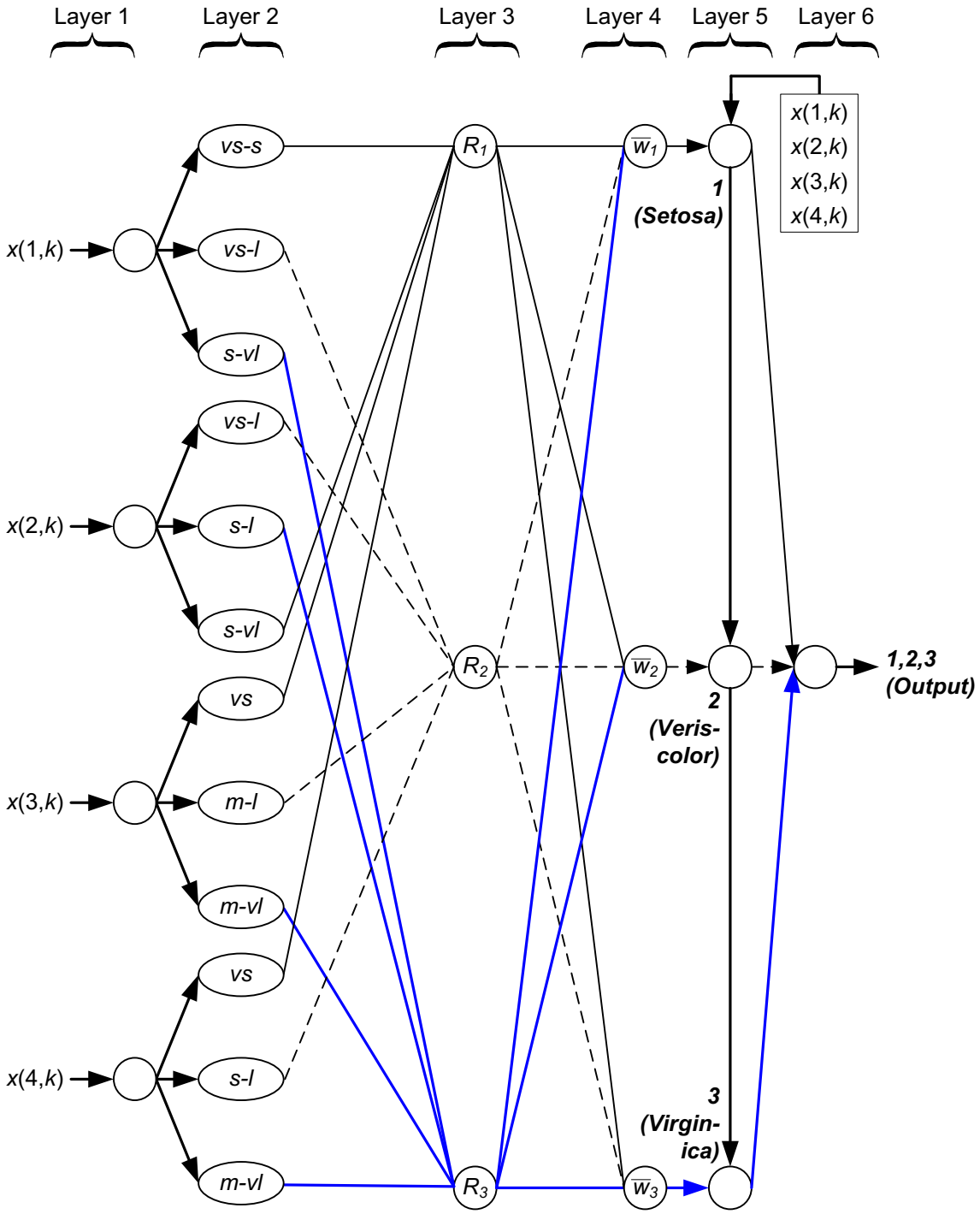

Fig. 5.6. Recognized fuzzy reasoning model of the iris dataset. All inputs are normalized from [0.0,1.0]. Approximations of membership functions are represented by "vs" (very small), "s" (small), "m" (medium), "l" (large), and "vl" (very large), denoting input ranges of [0.0,0.2), (0.2, 0.4], (0.4, 0.6], (0.6, 0.8], (0.8, 1.0], respectively.

With such a fuzzy reasoning model, a sample fuzzy rule for one of the flower type classifications can be described as follows:

$$R_1: \quad \text{IF} \quad \begin{cases} \begin{bmatrix} x(1,k) \text{ is} \\ \text{"very small" -} \\ \text{"small"} \end{bmatrix} & \text{AND} \quad \begin{bmatrix} x(2,k) \text{ is} \\ \text{"small"} \\ \text{-"very large"} \end{bmatrix} \quad \text{AND} \\ \begin{bmatrix} x(3,k) \text{ is} \\ \text{"very small"} \end{bmatrix} & \text{AND} \quad \begin{bmatrix} x(4,k) \text{ is} \\ \text{"very small"} \end{bmatrix} \end{cases} \tag{5.24}$$

$$\text{THEN} \quad y(k) \text{ is } 1 \rightarrow \text{Setosa flower type}$$

5.5.2 Comparison and Discussion

Table XI shows the results of the proposed evolving fuzzy classifier compared with other related evolving fuzzy classifiers in literature.

For this dataset, the accuracy of the propose classifiers #1 are comparable to that of classifiers #2, #3 and #4. Due to the simplicity of the dataset, all the classifiers effectively have similar accuracy.

Classifier #2 has lower average processing times than classifier #1, due to the generation of fewer clusters; the clusters do not sufficiently represent all the classes and as a result, do not have a fully transparent fuzzy rule base for decision making. Likewise, the proposed classifier #1 outperforms the comparison classifiers #3 and #4, in terms of class representation of the clusters, with a significant advantage of having a more transparent rule base. In addition, classifier #1 has lower processing times than #3 and #4 due to having less clusters.

In summary, the proposed classifier #1 demonstrates the ability to handle simple data with comparable accuracy, yet demonstrates improvement in terms of processing time and class representation of the clusters.

Table XI. Summary of results for the iris dataset over 100 trials, with 36 test samples per trial, expressed in terms of average and standard deviation (std) respectively.

Evolving Fuzzy Classifier variant	**Dataset**	Iris Average (*std*)
#1 Proposed (loose clustering)	Accuracy (%)	**99.81 (*0.82*)**
	No. of clusters	**2.99 (*0.1*)**
	Percentage of classes represented (%)	**99.67 (*3.33*)**
	Time/Sample (us)	**84.95 (*21.77*)**
#2 Comparison (strict clustering)	Accuracy (%)	99.97 (*0.28*)
	No. of clusters	2.02 (*0.14*)
	Percentage of classes represented (%)	67.33 (*4.69*)
	Time/Sample (us)	78.01 (*76.38*)
#3 Comparison publications [50,89] (loose clustering)	Accuracy (%)	99.67 (*0.28*)
	No. of clusters	26.10 (*5.18*)
	Percentage of classes represented (%)	99.33 (*4.69*)
	Time/Sample (us)	119.95 (*29.27*)
#4 Comparison publications [49,90] (strict clustering)	Accuracy (%)	99.92 (*0.48*)
	No. of clusters	5.26 (*1.60*)
	Percentage of classes represented (%)	66.67 (*0.00*)
	Time/Sample (us)	89.02 (*20.17*)

5.6 Performance Evaluation, Wine Dataset (Simulation)

5.6.1 Clustering and Identified Fuzzy Model

The inputs and expected outputs of the wine dataset are as follows:

- ***Inputs*:** Thirteen physical and chemical-based measurements of the wine with the following names: alcoholic, malic acid, ash, alkalinity, magnesium, total phenols, flavanoid, nonflavanoid, proanthocyanins, color intensity, hue, OD280/OD315 of diluted wines, and proline. These measurements respectively correspond to the system inputs of $x(1,k)$, $x(2,k)$, … , $x(13,k)$.
- ***Outputs*:** Three different wine type classifications, represented only with values of 1,2, and 3, corresponding to the system outputs of 1, 2, and 3 respectively.

The data and clustering across all attributes in one representative trial with the wine dataset are shown in Fig. 5.5, depicting 4 dimensions with the highest standard deviations (out of a total of 13 dimensions). Though the clusters closely correspond to the original data, different classes show significant overlap with one another; however, the distinctions can be clearer when considering all 13 dimensions simultaneously. Based on these clustering results, the recognized fuzzy model is shown in Fig. 5.6.

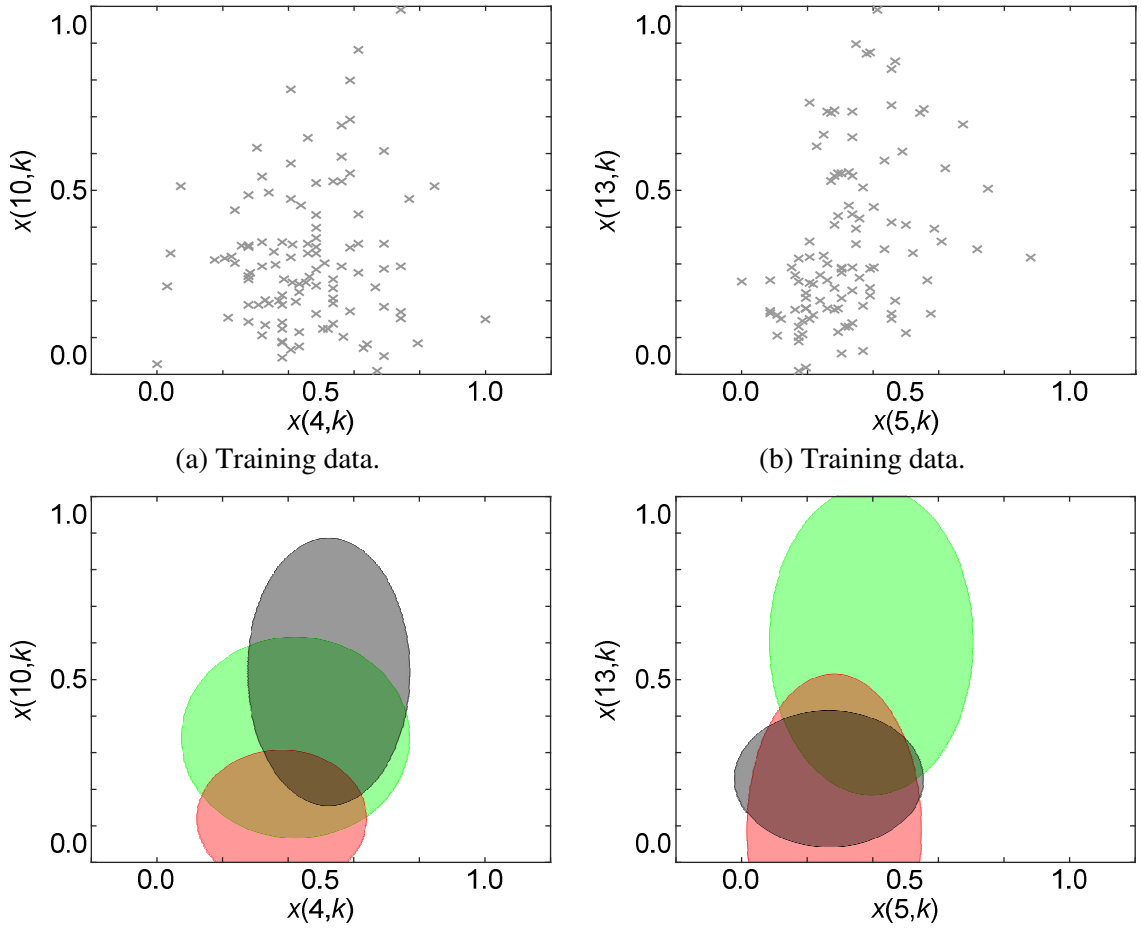

(a) Training data. (b) Training data.

(c) Resultant clusters. (d) Resultant clusters.

Fig. 5.7. Training data (a-b) and clustering results (c-d) of wine data, where green, red and black correspond to wine types of 1, 2, and 3, respectively; $x(4,k)$, $x(5,k)$, $x(10,k)$ and $x(13,k)$ represent alkalinity, magnesium content, colour intensity, and OD280/OD315 of diluted wines respectively.

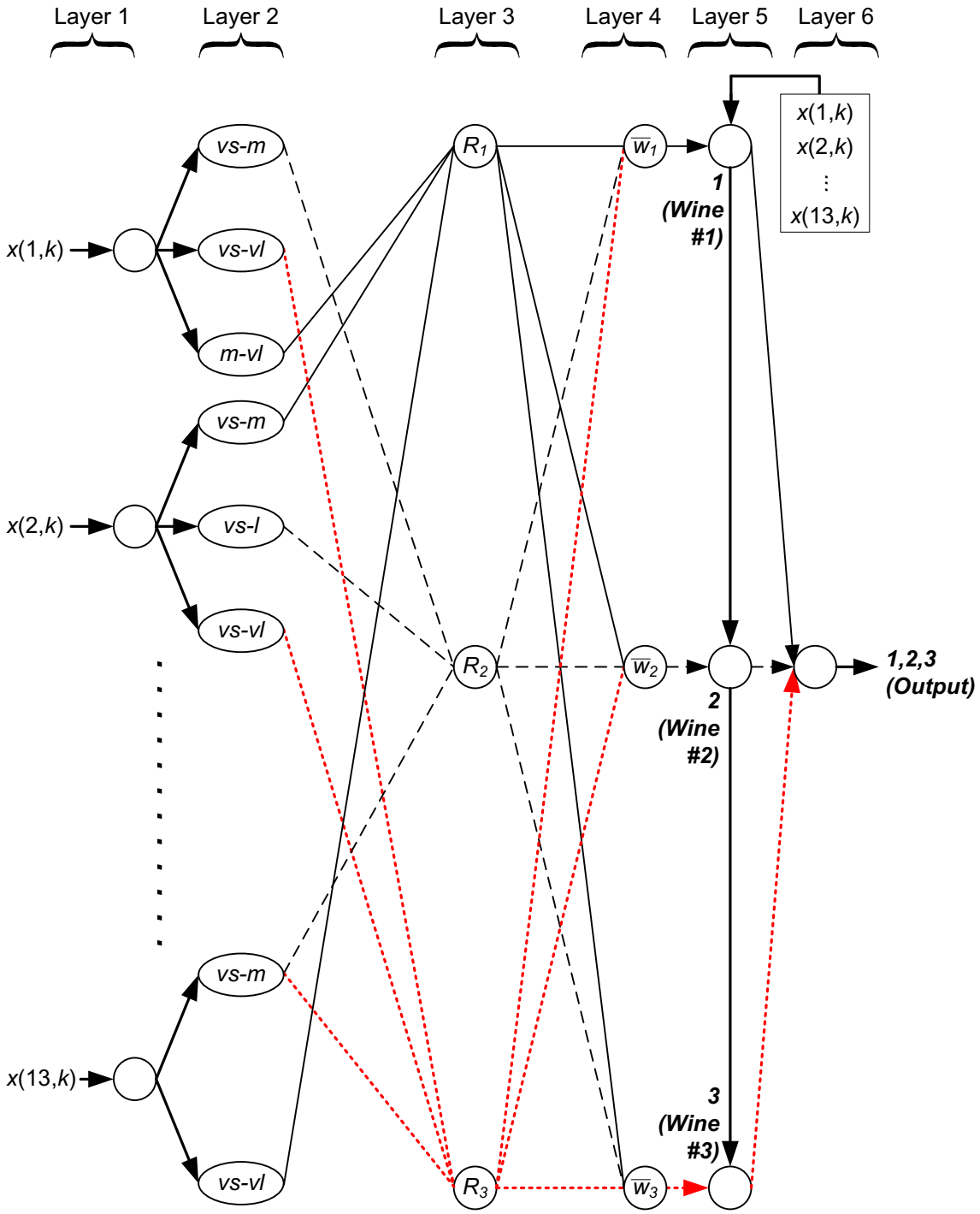

Fig. 5.8. Recognized fuzzy reasoning model of the wine dataset. All inputs are normalized from [0.0,1.0]. Approximations of membership functions are represented by "vs" (very small), "s" (small), "m" (medium), "l" (large), and "vl" (very large), denoting input ranges of [0.0,0.2), (0.2, 0.4], (0.4, 0.6], (0.6, 0.8], (0.8, 1.0], respectively.

With such a fuzzy reasoning model, a sample fuzzy rule for one of the wine type classifications can be described as follows:

$$R_1: \quad \text{IF} \quad \begin{cases} \begin{bmatrix} x(1,k) \text{ is} \\ \text{"medium"-} \\ \text{"very large"} \end{bmatrix} & \text{AND} & \begin{bmatrix} x(2,k) \text{ is} \\ \text{"very small"} \\ \text{-"medium"} \end{bmatrix} & \text{AND} \\ \quad \ldots & \text{AND} & \begin{bmatrix} x(13,k) \text{ is} \\ \text{"very small"-} \\ \text{"very large"} \end{bmatrix} & \end{cases} \tag{5.25}$$

$$\text{THEN} \quad y(k) \text{ is } 1 \rightarrow \text{Wine type \#1}$$

5.6.2 Comparison and Discussion

Table XII shows the results of the proposed evolving fuzzy classifier compared with other related evolving fuzzy classifiers in literature.

For this dataset, the accuracy of the proposed classifier #1 is second only to classifier #3. This may be due to the complexity of the dataset which favours more clusters for better representation of the underlying data.

Though classifier #2 has the lowest average processing times due to having the just one cluster on average, this cluster cannot sufficiently represent all the classes and as a result, does not have a fully transparent fuzzy rule base for decision making. Likewise, classifier #4 has similar lack of class representation. This clearly demonstrates the advantages and limitations of an overly-strict clustering scheme.

Likewise, the proposed classifier #1 outperforms the comparison classifiers #3 and #4, in terms of class representation of the clusters, with an advantage of having a more transparent rule base. In addition, classifier #1 has lower processing times than #3 and #4 due to having less clusters.

In summary, the proposed classifier #1 demonstrates limitations in handling very complex data accurately, yet demonstrates improvement in terms of processing time and class representation of the clusters.

Table XII. Summary of results for the wine dataset over 100 trials, with 36 test samples per trial, expressed in terms of average and standard deviation (std) respectively.

Evolving Fuzzy Classifier variant	**Dataset**	Wine Average (*std*)
#1 Proposed (loose clustering)	Accuracy (%)	**94.92 (*3.21*)**
	No. of clusters	**2.95 (*0.26*)**
	Percentage of classes represented (%)	**98.33 (*8.70*)**
	Time/Sample (us)	**91.74 (*27.74*)**
#2 Comparison (strict clustering)	Accuracy (%)	90.89 (*2.13*)
	No. of clusters	1.27 (*0.45*)
	Percentage of classes represented (%)	42.33 (*14.87*)
	Time/Sample (us)	84.78 (*25.20*)
#3 Comparison publications [50,89] (loose clustering)	Accuracy (%)	97.25 (*3.12*)
	No. of clusters	18.81 (*7.84*)
	Percentage of classes represented (%)	95.67 (*15.47*)
	Time/Sample (us)	127.79 (*38.61*)
#4 Comparison publications [49,90] (strict clustering)	Accuracy (%)	91.06 (*1.66*)
	No. of clusters	3.66 (*1.02*)
	Percentage of classes represented (%)	41.00 (*14.10*)
	Time/Sample (us)	95.58 (*24.94*)

5.7 Performance Evaluation, Health Condition Monitoring of IM Rotor Bar Faults (Implementation)

The developed evolving fuzzy classifier is implemented for rotor bar health condition monitoring. The input data used for the classifier are derived from the experiments as described in Section 4.1.

5.7.1 Clustering and Identified Fuzzy Model

The inputs and expected outputs of the 50 Hz and 60 Hz rotor bar datasets are as follows:

- ***Inputs*:** Three monitoring indices consisting of: rotor speed (corresponding to slip and load condition), $2sf_L$-based fault index (Eq. (4.3)), and sideband-based fault index from Eq. (4.1), corresponding to the system inputs of $x(1,k)$, $x(2,k)$, and $x(3,k)$, respectively
- ***Outputs*:** Five different motor classifications, representing: healthy (motor #1), healthy (motor #2, with differences due to manufacturing tolerances), 1-bar fault (motor #3), 2-bar fault (motor #4), and 3-bar fault (motor #5), corresponding to the system outputs of 1, 2, 3, 4, and 5 respectively.

The data and clustering across all attributes in one representative trial with the 50 Hz and 60 Hz broken rotor bar dataset are shown in Fig. 5.9 and Fig. 5.10. It can be seen that the clusters closely correspond to the original data, showing clear distinctions between the different classes. Based on these clustering results, the corresponding recognized fuzzy models for the 50 Hz and 60 Hz datasets are shown in Fig. 5.11 and Fig. 5.12, respectively.

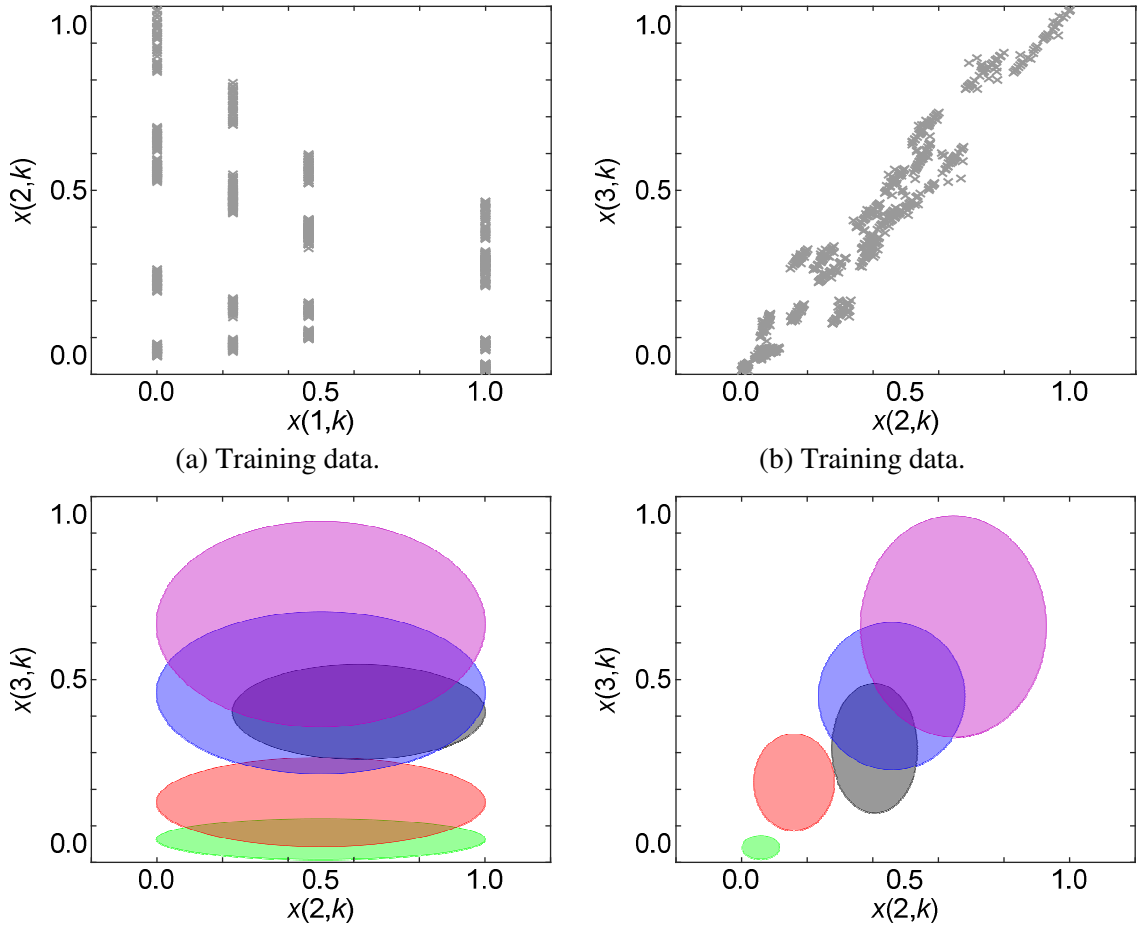

(a) Training data. (b) Training data.

(c) Resultant clusters. (d) Resultant clusters.

Fig. 5.9. Training data (a-b) and clustering results (c-d) of 50 Hz rotor bar faulted data, where green, red, black, blue, and purple correspond to healthy #1, healthy #2, 1-bar, 2-bar, and 3-bar faults, respectively. $x(1,k)$, $x(2,k)$, and $x(3,k)$ represent motor's speed (i.e., loading condition), $2sf_L$-based fault index (Eq. (4.3)), and sideband-based fault index (Eq. (4.1)) respectively.

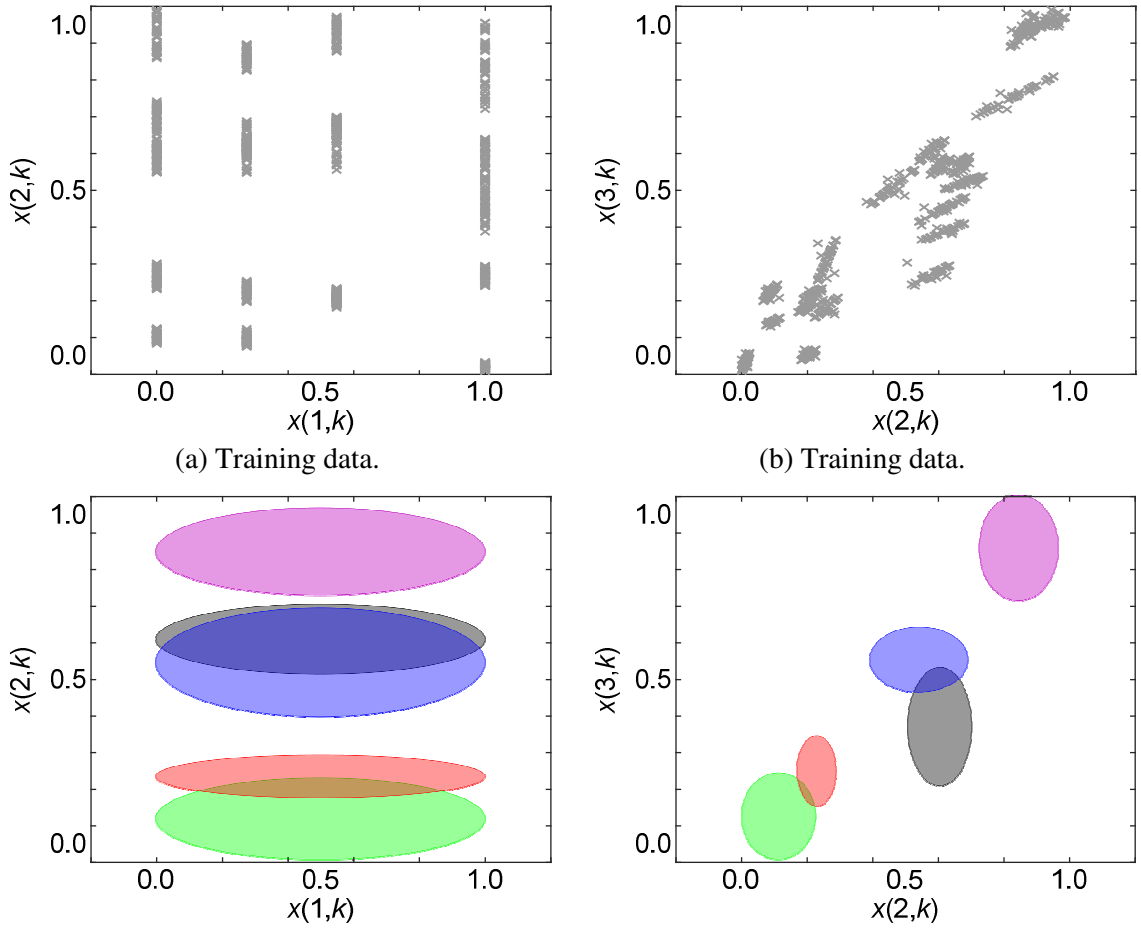

(a) Training data. (b) Training data.

(c) Resultant clusters. (d) Resultant clusters.

Fig. 5.10. Training data (a-b) and clustering results (c-d) of 60 Hz rotor bar faulted data, where green, red, black, blue, and purple correspond to healthy #1, healthy #2, 1-bar, 2-bar, and 3-bar faults, respectively. $x(1,k)$, $x(2,k)$, and $x(3,k)$ represent motor's speed (i.e., loading condition), $2sf_L$-based fault index (Eq. (4.3)), and sideband-based fault index (Eq. (4.1)) respectively.

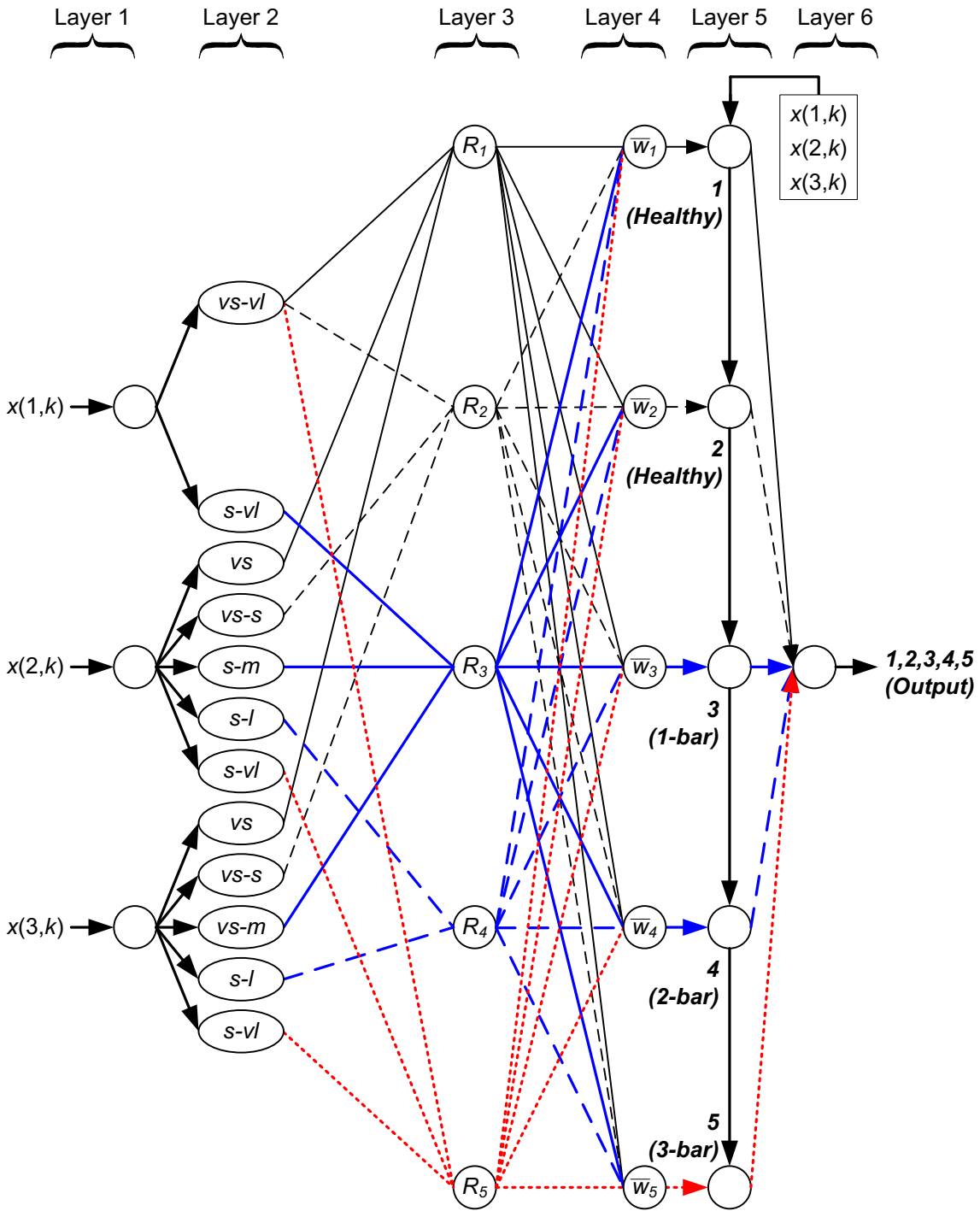

Fig. 5.11. Recognized fuzzy reasoning model of the 50 Hz faulted rotor bar dataset. All inputs are normalized from [0.0,1.0]. Approximations of membership functions are represented by "vs" (very small), "s" (small), "m" (medium), "l" (large), and "vl" (very large), denoting input ranges of [0.0,0.2), (0.2, 0.4], (0.4, 0.6], (0.6, 0.8], (0.8, 1.0], respectively.

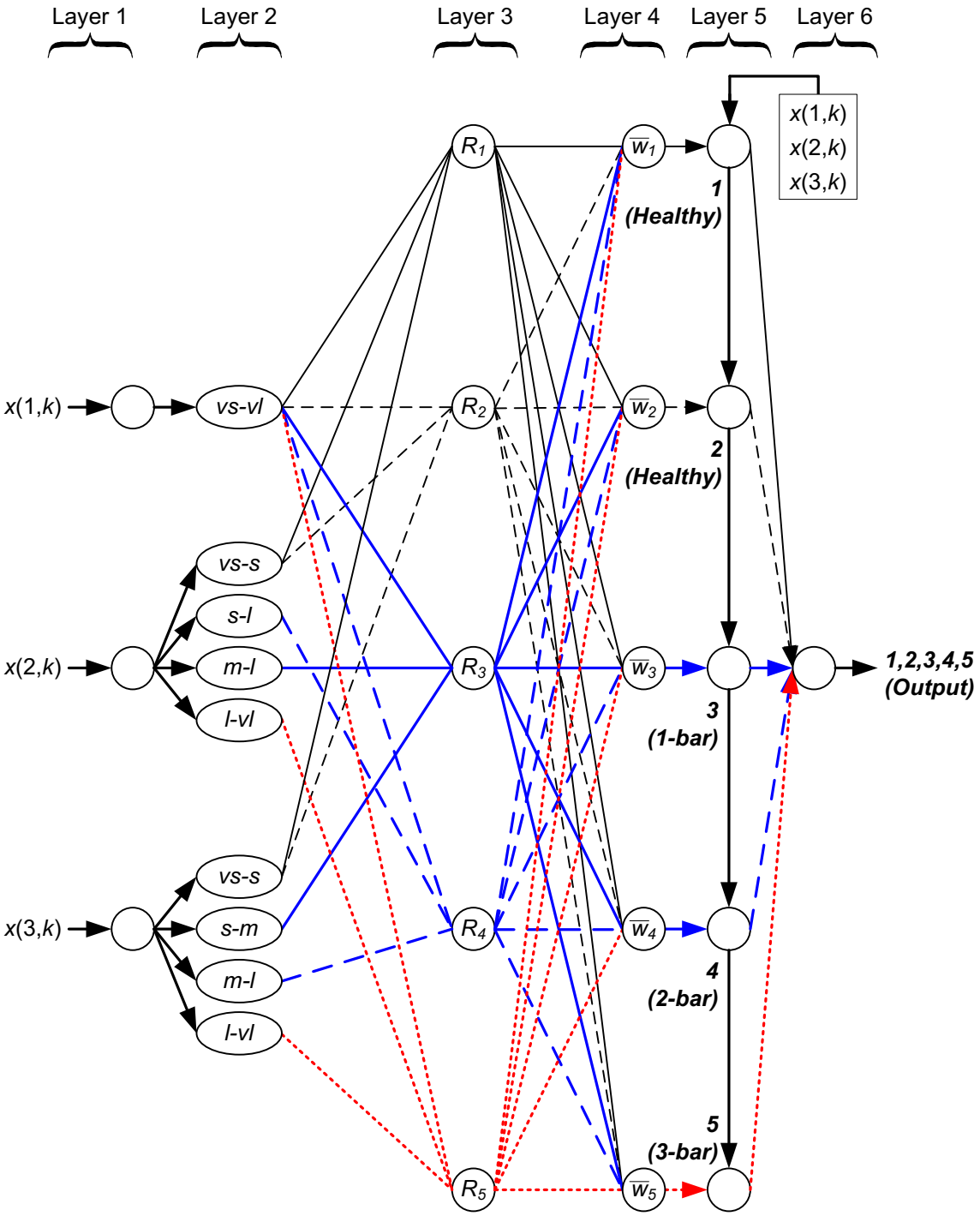

Fig. 5.12. Recognized fuzzy reasoning model of the 60 Hz faulted rotor bar dataset. All inputs are normalized from [0.0,1.0]. Approximations of membership functions are represented by "vs" (very small), "s" (small), "m" (medium), "l" (large), and "vl" (very large), denoting input ranges of [0.0,0.2), (0.2, 0.4], (0.4, 0.6], (0.6, 0.8], (0.8, 1.0], respectively.

With such a fuzzy reasoning model, the fuzzy rules for a 60Hz healthy condition can be described as follows:

$$R_1: \quad \text{IF} \quad \begin{bmatrix} x(1,k)\,\text{is} \\ \text{"very small"} - \\ \text{"very large"} \end{bmatrix} \quad \text{AND} \quad \begin{bmatrix} x(2,k)\,\text{is} \\ \text{"very small"} \\ -\text{"small"} \end{bmatrix} \quad \text{AND} \quad \begin{bmatrix} x(3,k)\,\text{is} \\ \text{"very small"} \\ -\text{"small"} \end{bmatrix} \tag{5.26}$$

$$\text{THEN} \quad y(k)\,\text{is}\,1 \rightarrow \text{Healthy Condition (motor \#1)}$$

$$R_2: \quad \text{IF} \quad \begin{bmatrix} x(1,k)\,\text{is} \\ \text{"very small"} - \\ \text{"very large"} \end{bmatrix} \quad \text{AND} \quad \begin{bmatrix} x(2,k)\,\text{is} \\ \text{"very small"} \\ -\text{"small"} \end{bmatrix} \quad \text{AND} \quad \begin{bmatrix} x(3,k)\,\text{is} \\ \text{"very small"} \\ -\text{"small"} \end{bmatrix} \tag{5.27}$$

$$\text{THEN} \quad y(k)\,\text{is}\,1 \rightarrow \text{Healthy Condition (motor \#2)}$$

$$R_3: \quad \text{IF} \quad \begin{bmatrix} x(1,k)\,\text{is} \\ \text{"very small"} - \\ \text{"very large"} \end{bmatrix} \quad \text{AND} \quad \begin{bmatrix} x(2,k)\,\text{is} \\ \text{"medium"} \\ -\text{"large"} \end{bmatrix} \quad \text{AND} \quad \begin{bmatrix} x(3,k)\,\text{is} \\ \text{"small"} \\ -\text{"medium"} \end{bmatrix} \tag{5.28}$$

$$\text{THEN} \quad y(k)\,\text{is}\,1 \rightarrow 1\text{-bar Faulted Condition (motor \#3)}$$

$$R_4: \quad \text{IF} \quad \begin{bmatrix} x(1,k)\,\text{is} \\ \text{"very small"} - \\ \text{"very large"} \end{bmatrix} \quad \text{AND} \quad \begin{bmatrix} x(2,k)\,\text{is} \\ \text{"small"} \\ -\text{"large"} \end{bmatrix} \quad \text{AND} \quad \begin{bmatrix} x(3,k)\,\text{is} \\ \text{"medium"} \\ -\text{"large"} \end{bmatrix} \tag{5.29}$$

$$\text{THEN} \quad y(k)\,\text{is}\,1 \rightarrow 2\text{-bar Faulted Condition (motor \#4)}$$

$$R_5: \quad \text{IF} \quad \begin{bmatrix} x(1,k)\,\text{is} \\ \text{"very small"} - \\ \text{"very large"} \end{bmatrix} \quad \text{AND} \quad \begin{bmatrix} x(2,k)\,\text{is} \\ \text{"large"} \\ -\text{"very large"} \end{bmatrix} \quad \text{AND} \quad \begin{bmatrix} x(3,k)\,\text{is} \\ \text{"large"} \\ -\text{"very large"} \end{bmatrix} \tag{5.30}$$

$$\text{THEN} \quad y(k)\,\text{is}\,1 \rightarrow 3\text{-bar Faulted Condition (motor \#5)}$$

5.7.2 Comparison and Discussion

Table XIII and Table XIV shows the results of the proposed evolving fuzzy classifier compared with other related evolving fuzzy classifiers in literature.

For these datasets, the accuracy of the proposed classifier #1 is the highest, though only by a small margin over classifier #3.

Though classifier #2 has the lowest average processing times due to having the least clusters. However, these clusters do not sufficiently represent all the classes and as a result, does not have a fully transparent fuzzy rule base for decision making. Likewise, the proposed classifier #1 outperforms the comparison classifiers #3 and #4, in terms of class representation of the clusters, with an advantage of having a more transparent rule base. In addition, classifier #1 has lower processing times than #3 and #4 due to having less clusters.

In summary, the proposed classifier #1 demonstrates competence in handling moderately complex rotor bar fault data most accurately, and in addition, demonstrates improvement in terms of processing time and class representation of the clusters.

Table XIII. Summary of results for the 50 Hz rotor bar dataset, averaged over 100 trials, with 250 test samples per trial, expressed in terms of average and standard deviation (std) respectively.

Evolving Fuzzy Classifier variant	**Dataset**	Rotor bar, 50 Hz Average (*std*)
#1 Proposed (loose clustering)	Accuracy (%)	**99.37 (*0.91*)**
	No. of clusters	**5.00 (*0.00*)**
	Percentage of classes represented (%)	**100.00 (*0.00*)**
	Time/Sample (us)	**19.79 (*12.22*)**
#2 Comparison (strict clustering)	Accuracy (%)	92.30 (*3.99*)
	No. of clusters	2.86 (*0.35*)
	Percentage of classes represented (%)	57.20 (*6.97*)
	Time/Sample (us)	14.20 (*5.34*)
#3 Comparison publications [50,89] (loose clustering)	Accuracy (%)	98.90 (*1.16*)
	No. of clusters	115.02 (*53.69*)
	Percentage of classes represented (%)	100.00 (*0.00*)
	Time/Sample (us)	148.93 (*65.42*)
#4 Comparison publications [49,90] (strict clustering)	Accuracy (%)	94.44 (*2.70*)
	No. of clusters	9.13 (*2.03*)
	Percentage of classes represented (%)	58.40 (*5.45*)
	Time/Sample (us)	23.54 (*6.33*)

Table XIV. Summary of results for the 60 Hz rotor bar dataset, averaged over 100 trials, with 250 test samples per trial, expressed in terms of average and standard deviation (std) respectively.

Evolving Fuzzy Classifier variant	**Dataset**	Rotor bar, 60 Hz Average (*std*)
#1 Proposed (loose clustering)	Accuracy (%)	**99.45 (*2.21*)**
	No. of clusters	**4.75 (*0.63*)**
	Percentage of classes represented (%)	**95.00 (*12.51*)**
	Time/Sample (us)	**16.80 (*3.16*)**
#2 Comparison (strict clustering)	Accuracy (%)	88.47 (*3.82*)
	No. of clusters	2.00 (*0.00*)
	Percentage of classes represented (%)	40.00 (*0.00*)
	Time/Sample (us)	13.18 (*4.23*)
#3 Comparison publications [50,89] (loose clustering)	Accuracy (%)	98.90 (*2.89*)
	No. of clusters	106.99 (*63.41*)
	Percentage of classes represented (%)	87.60 (*17.00*)
	Time/Sample (us)	126.73 (*72.96*)
#4 Comparison publications [49,90] (strict clustering)	Accuracy (%)	86.25 (*1.77*)
	No. of clusters	8.47 (*2.25*)
	Percentage of classes represented (%)	40.00 (*0.00*)
	Time/Sample (us)	21.59 (*5.61*)

5.8 Performance Evaluation, Overall

For all datasets overall, the accuracy of this classifier approaches or exceeds that of comparison classifiers. In addition, the proposed classifier is more efficient while its clusters generated by the proposed evolving algorithm represent all classes most consistently. Due to this better representation of all the classes, the rule base is also more complete, where the classifier more consistently generates unique fuzzy rules describing every output class

In having unique rules, missed and false alarms in a diagnostic application can be investigated upon, where it is possible to track the monitoring indices responsible for an incorrect classifier output.

The processing times for each sample across all datasets are in the order of tens of microseconds. This is significantly faster than the generation of monitoring indices, which require relatively length data acquisition and signal processing to create it. Hence, this classifier demonstrates suitability for use in a condition monitoring application.

CHAPTER 6
Conclusions and Future Work

6.1 Conclusions

IMs are the powerhouse of industrial applications. In light of projected trends pertaining to Industry 4.0 [91], one major issue is related to how to improve production quality and operational safety, while reducing costs. One solution is related to the new predictive maintenance strategy. The challenges facing the implementation of predictive maintenance in industrial applications are related to efficient DAQ using smart sensor networks, more reliable IM fault detection techniques, and more accurate diagnostic pattern classification.

The objective of this work is the development of a wireless smart sensor-based IM condition monitoring system, focusing on IM rotor bar fault detection. Specifically, research and development contributions achieved include: (1) develop of wireless smart current and vibration sensor DAQ, (2) a synergistic feature analysis technique for rotor bar fault detection, (3) a post-processing technique for a monitoring index formulation, and (4) an evolving fuzzy classifier for automated IM diagnosis. These aspects are summarized as follows:

4) **Wireless Smart Sensor DAQ:** The non-invasive nature of the wireless smart sensor DAQ allows for simpler, lower cost installation in real industrial monitoring applications, without modifications to existing infrastructure. Specific contributions include:
   5) A new strategy to design for signal conditioning circuits with respect to noise, bandwidth, and desired signal-to-noise ratios.
   6) A new design method to ensure correctly-timed data samples.
   7) A new design strategy for noise and reliable wireless transmissions.
8) **Signal Processing for Rotor Bar Fault Detection:** The fault feature extraction is based on the analysis of the slip-related frequencies at higher harmonics of the current spectrum. Vibration signals are used to estimate the rotor speed used to determine the slip which is in turn, used for fault detection. Specific contributions include:

9) A new strategy of fault feature extraction, based on even multiples of a slip-based frequency.
10) A synergistic feature analysis technique for accurate fault detection.
11) A means to verify consistent rotor frequency to ensure correct fault feature extraction.
12) A post-processing method to formulate a signal-to-noise-ratio-based fault index based from the extracted features.

13) **Diagnostic Classifier for IM Condition Monitoring:** An evolving fuzzy classifier has been developed with an updated evolutionary clustering algorithm and fuzzy inference rule structure accounting for multiple clusters belonging to different motor fault conditions. Specific contributions include:
14) A revised clustering algorithm to more accurately create clusters based on more representative data information.
15) An adaptation of an evolving fuzzy classification system with rotor bar condition monitoring.

The effectiveness of the aforementioned contributions has been verified by experiments or simulation tests. Test results have shown that the analysis, indexing, and classification methods have advantages over the related conventional methods. For example, in:

16) **DAQ:** Due in a large part to the SNR and timing design considerations involved in the smart sensor DAQ, this work achieved a unique merit of being able to detect rotor bar faults in IMs under a zero-load decoupled condition:
17) **Fault detection:** Surpasses conventional techniques in terms of differentiating between a healthy and faulty motor while also differentiating fault severity under different operating conditions.
18) **Classifier:** With rotor bar fault condition monitoring, the developed classifier demonstrates improved accuracy, processing efficiency, and ability to produce distinct fuzzy rules to clearly indicate the reasoning process behind every classification output.

Due to the successful validation of technologies listed above, the developed intelligent IM monitoring system has a potential to be used in real industrial predictive maintenance applications.

6.2 Future Work

Based on the results of this work, advanced research can be undertaken to further improve the reliability and applicability of the developed IM monitoring systems.

6.2.1 Wireless Smart Sensors

- More efficient wireless networking topologies can be achieved, such as a mesh network.
- Industry-standard wireless deterministic sequential communications methods such as the Master-Slave Token-Passing (MS/TP) protocol [92] can be implemented for wireless communications.
- To reduce power consumption, sleep functionality can be implemented, where wireless smart sensors can be in a sleep mode, and periodically wake up to detect any commands from the receiver.
- Depending on the signal processing requirements, a different MCU supporting a higher operating frequency can be used for applications requiring a higher sampling frequency; an external ADC with a corresponding noise-resistant PCB design can be used to optimize the SNR of the collected signal.
- To increase the operational lifespan of a wireless smart sensor, energy harvesting of vibration and/or electromagnetic fields can be used to charge the sensor's battery. Energy harvesting may be more viable in the future when costs of related components decrease due to manufacturing standardization and mass production.
- Brownout detection can be implemented to detect when power supplies are insufficient for correct DAQ operations [93], with subsequent wireless communications notifying the receiver of this insufficient power supply condition.

6.2.2 Signal Processing and Fault Detection

- For rotor bar fault detection, it has been shown that fault severity is influenced by the location of the rotor bar faults [82,83]. More investigation can be undertaken to theoretically model and experimentally validate the influence of rotor bar fault location on a corresponding fault severity index.

- The results of the fault indices in this work are largely based on a measure of the SNR as per Eq. (3.28), which is in turn based on a noise estimation of Eq. (3.29). There are more accurate means to estimate noise, such as the use of subspace decompositions [94], which would in turn produce more accurate fault indices for fault detection.
- More efficient signal processing techniques can be proposed for the fault detection of other IM components (e.g., bearings, rotors, stator windings, and electrical systems) for different types/sizes of IMs under different operating conditions with different system dynamics.

6.2.3 Diagnostic Classifiers for IM Condition Monitoring

Additional strategies for use in an evolving classifier can be proposed to improve fuzzy classification reliability, efficiency, and decision-making transparency. For instance, the principal component analysis can be used to identify the eigenvectors of the data that have the most significant variation [18]; the state vector machine can be used to identify a curve/surface of best fit for different groups of data [41]. Advanced research can be undertaken to integrate the advantages of these two techniques while still achieving transparency in the decision-making of an evolving fuzzy classifier.

6.2.4 Overall Strategic Industrial Implementation

The industrial implementation of the technologies developed in this work, by descending order of priority, is as follows:

- DAQ for fault feature extraction.
- Fault feature extraction with signal processing for use with classifiers.
- Classifiers using machine learning techniques for use with condition monitoring.

A classifier for condition monitoring cannot be achieved without effective fault feature extraction, which in turn, cannot be achieved without the correct DAQ of data.

To adapt the technologies developed in this work for industrial applications, collaborations with related industrial partners should be undertaken to collect data using wireless smart sensor networks. The smart sensors can be validated and improved based on the requirements of real applications, such as bandwidth, noise, and SNR.

Based on real data, the effectiveness and robustness of fault feature extraction techniques (i.e., clarity in fault detection and fault severity differentiation) can be further validated and developed.

Contingent on first obtaining reliable data and fault feature extraction methods, machine learning techniques can then be used to further validate and improve the robustness of the diagnostic classifier, in terms of its ability to accommodate different types of motors, operating conditions, and system dynamics associated with actual industrial systems.

APPENDIX A

Smart Sensor Design Schematics

Shown in Fig. 6.1-Fig. 6.4 are schematics developed for the transmitting smart sensors and receivers for this work, with Fig. 6.5 and Fig. 6.6 being the final printed circuit board (PCB) designs for the transmitters and receivers respectively.

The design was made with the Kicad Electronics Design Automation Suite [95]; initial 2-layer PCB prototypes were fabricated with a Bantam Tools Desktop Milling Machine [96], with a finalized 4-layer PCB design fabricated by Sunbest Technology Co. Ltd.[97] through an academic-industrial partnership between Lakehead University and eMechsys Inc. [98]

Subsequent soldering / assembly, testing, and programming were accomplished by the author. Programming was completed with the Arduino Integrated Development Environment [99] .

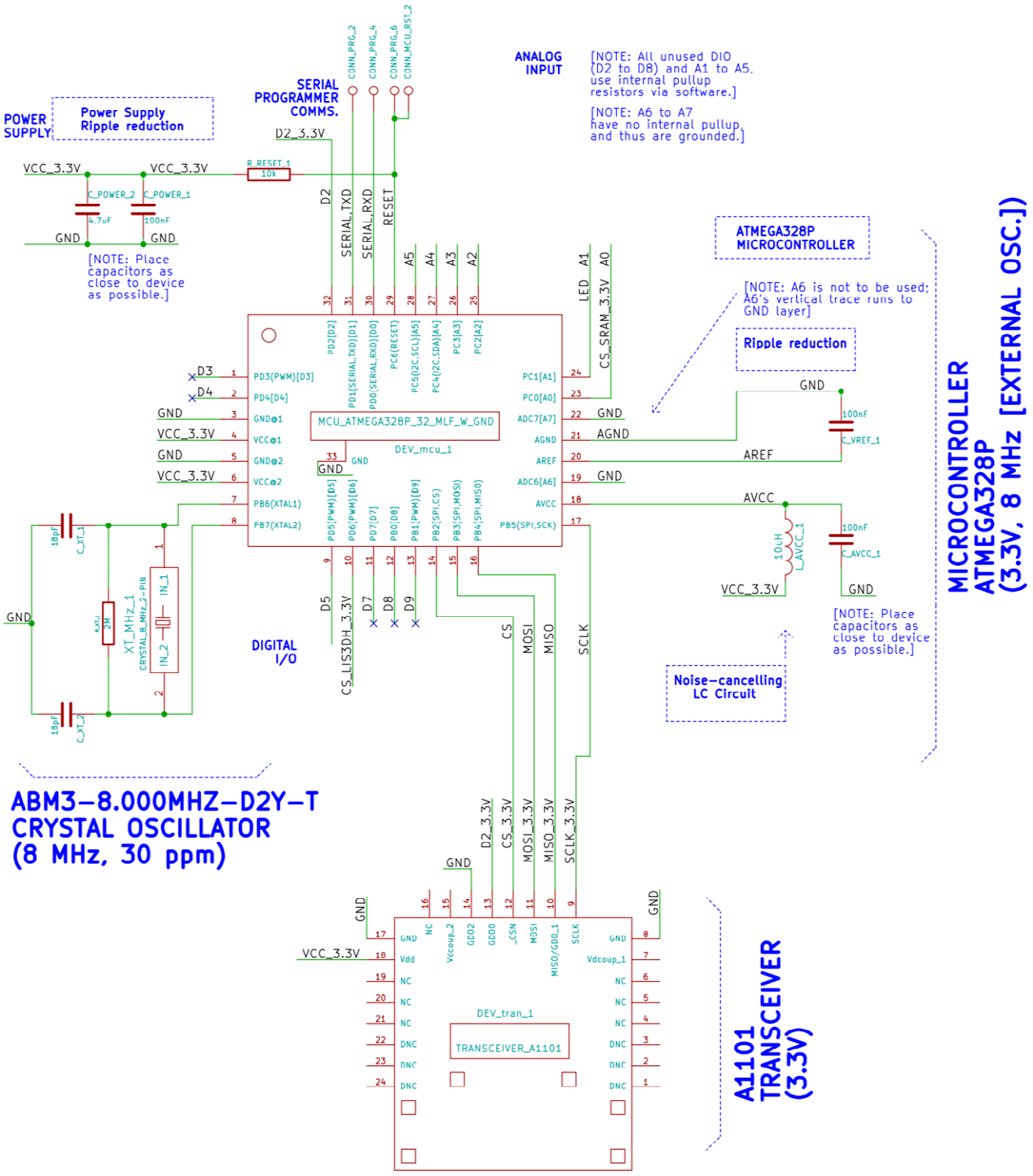

Fig. 6.1. Smart sensor transmitter design schematic, main components.

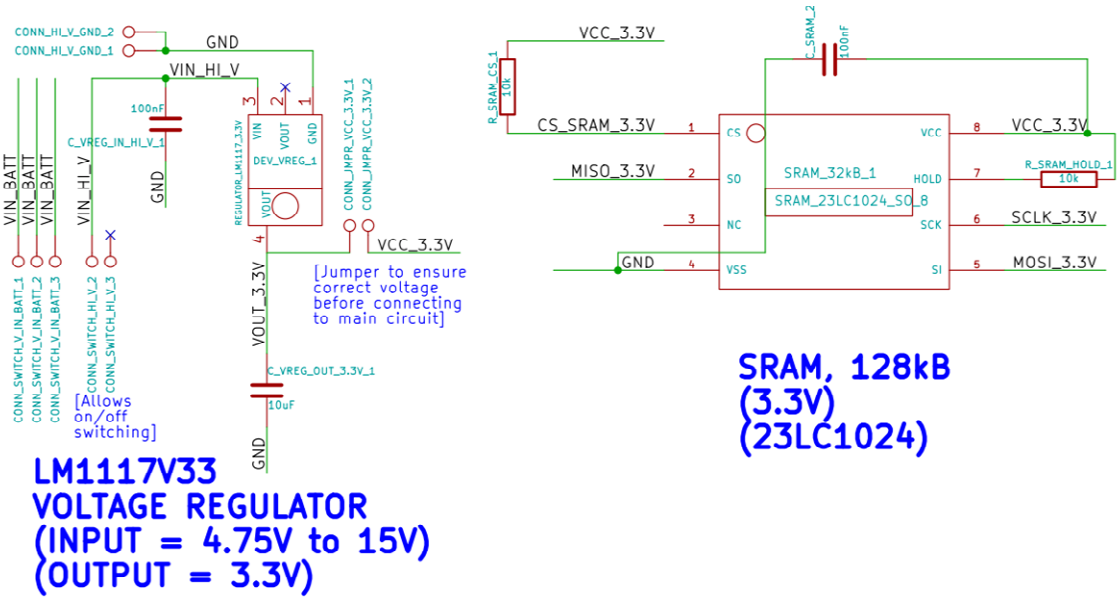

Fig. 6.2. Smart sensor transmitter design schematic, supplementary components.

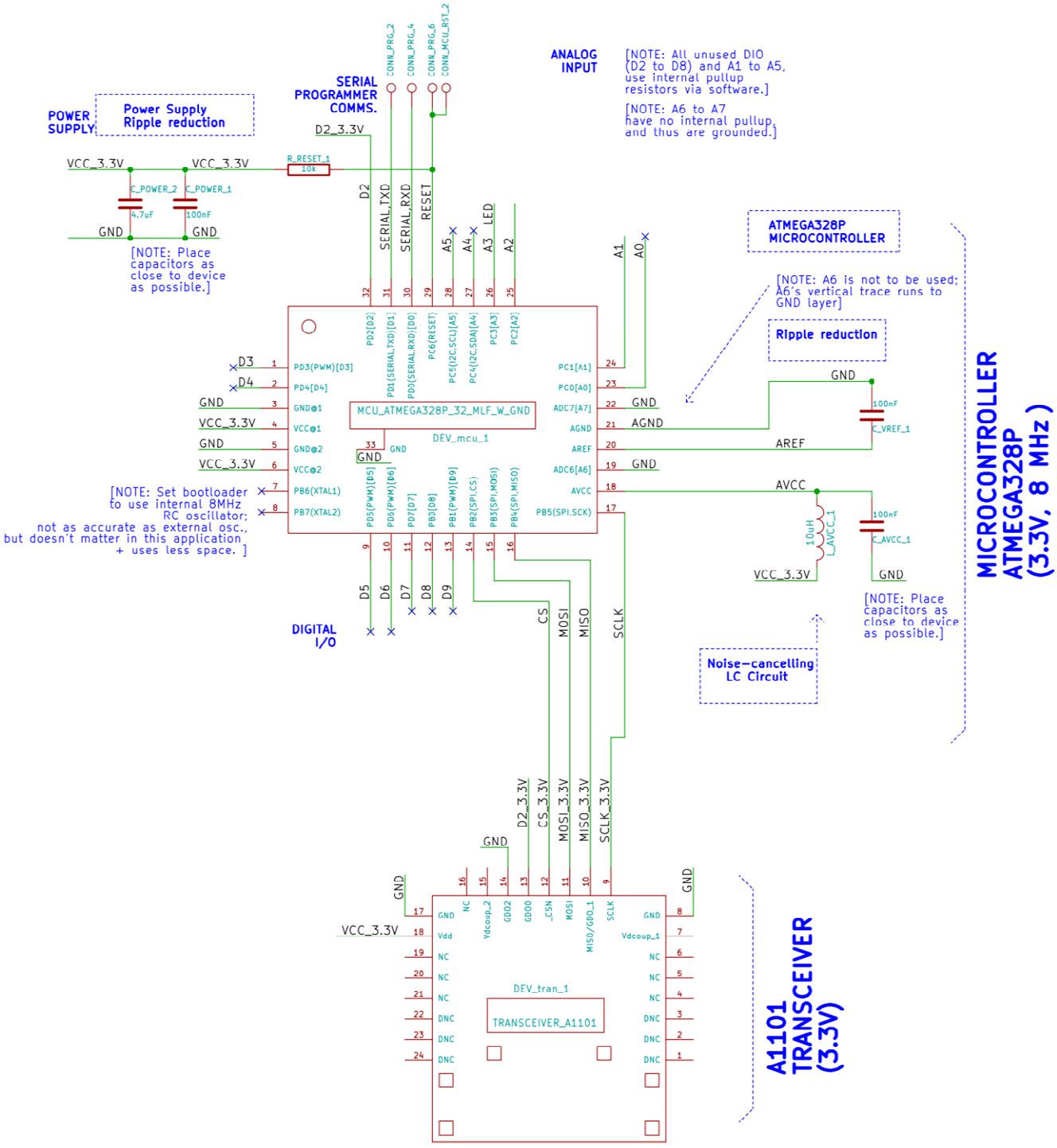

Fig. 6.3. Smart sensor receiver design schematic, main components.

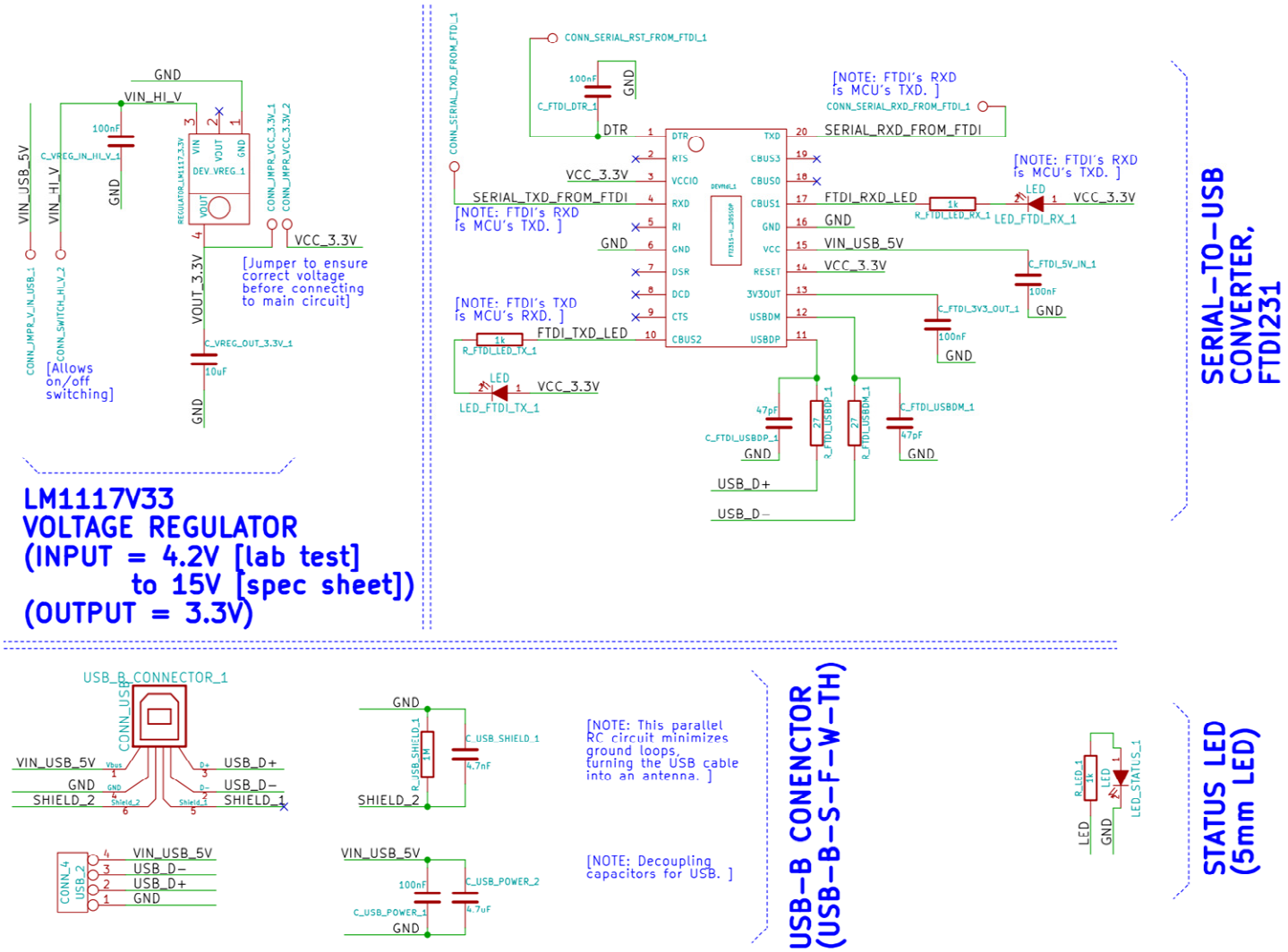

Fig. 6.4. Smart sensor receiver design schematic, supplementary components.

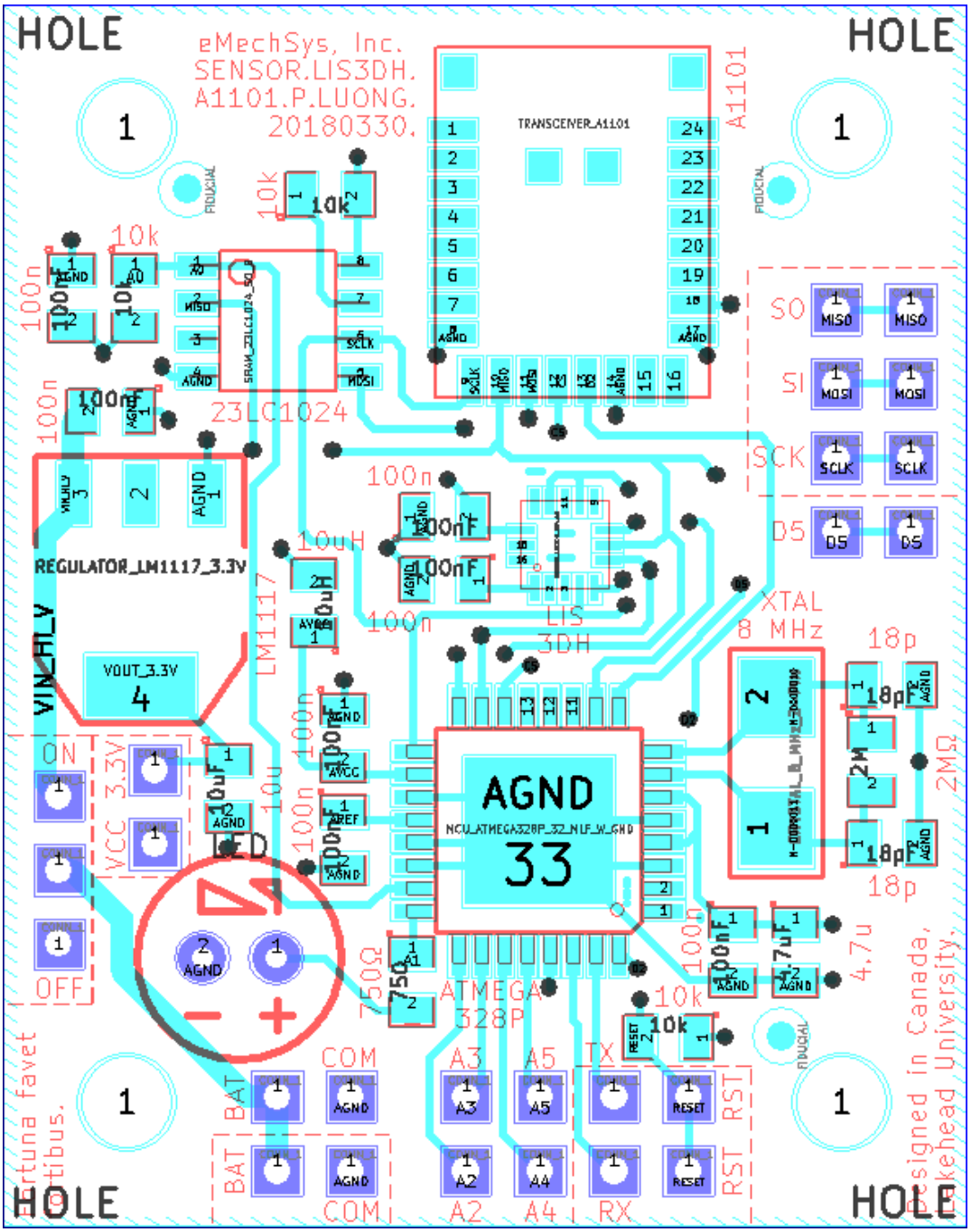

Fig. 6.5. Smart sensor transmitter PCB schematic.

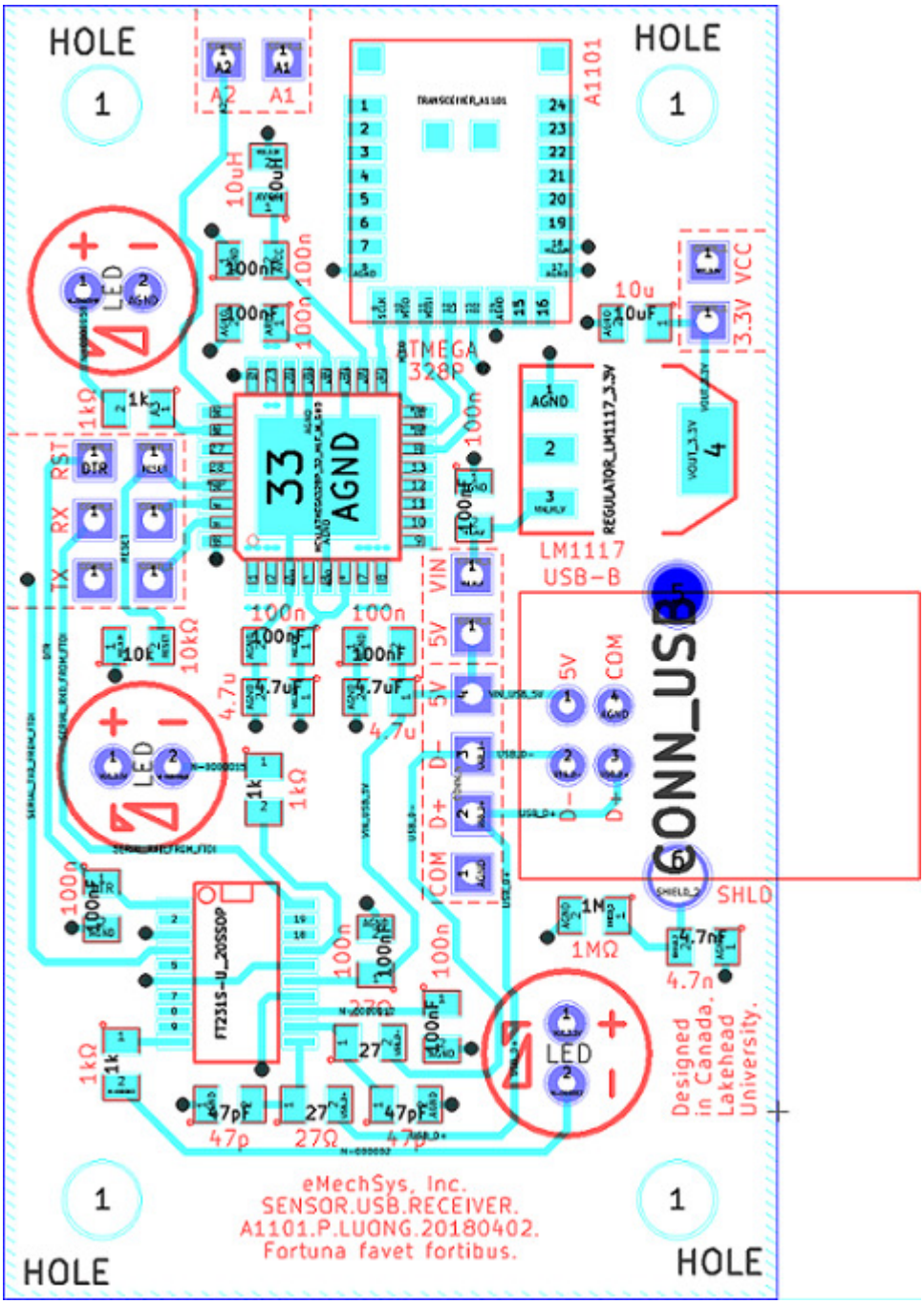

Fig. 6.6. Smart sensor receiver PCB schematic.

APPENDIX B
Initial Rotor Fault Investigation

6.3 Preface

The work described in this Appendix was from an initial investigation into the rotor bar faults. The results were not used in this work due to multiple fundamental issues related to the creation of the rotor bar faults, overloaded test conditions, and achieving an appropriate SNR. These issues were subsequently corrected as a consequence of this investigation.

As these issues are currently not comprehensively indicated in any available literature, the purpose of this Appendix is to provide reference to future researchers to ensure test conditions have been more thoroughly considered and to prevent a repetition of similar erroneous procedures.

6.4 Overview

For a quick validation of the underlying theories, an initial investigation into broken rotor bars was conducted with conventional DAQ equipment. At the time of this initial investigation, only certain faulted rotors were available, where holes were drilled into the rotor end caps as shown in Fig. 6.7.

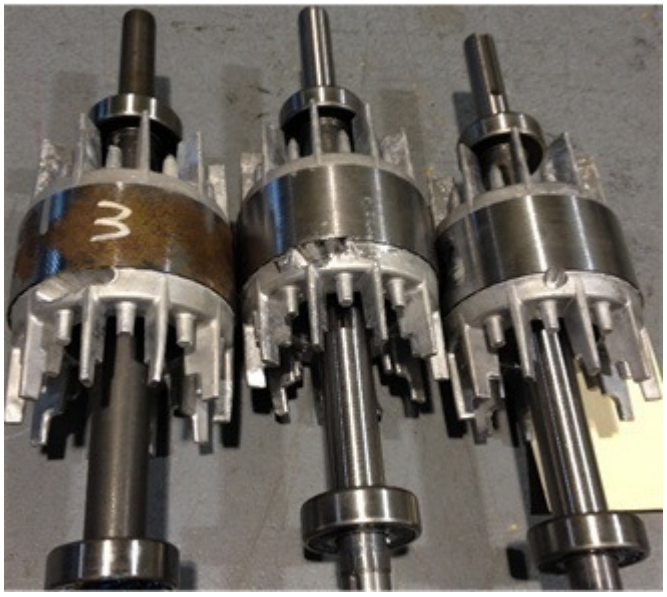

Fig. 6.7. Rotors with simulated defects drilled at the rotor end caps.

6.5 Experimental Setup

The experimental setup is shown in Fig. 6.8.

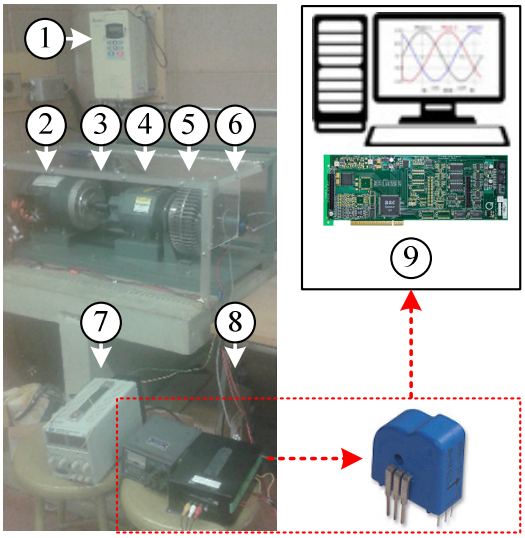

Fig. 6.8. Experimental setup: (1) power source and VFD, (2) IM under test, (3) coupling, (4) speed-reduction gearbox, (5) magnetic clutch, (7) DC power source, (8) current transformers and signal conditioning apparatus, (9) conventional DAQ board and computing device.

The setup is largely the same as that described in Section 4.1, with differences listed as follows:

1) A solid core current transformer (*LTS6NP* from LEM) monitors every phase of the IM, with a separate 5V lab power supply and first-order low pass filters used as signal conditioning.
2) A conventional DAQ board (*Q4* from Quanser) was installed into a PCI slot of the desktop computer and used for data collection. The DAQ board has an ADC resolution of 14 bits and a sensing range of +/-10V.
3) A digital shaft rotation encoder (*NSN-1024* from Cui Inc.) was used to monitor the output of the speed-reduction gearbox, of which the IM shaft rotation speed can be derived from.

The tested motor specifications and the test conditions are summarized in Table II and Table XV, respectively.

Table XV. Summary of test conditions with conventional DAQ system.

VFD Frequency	50 Hz
Motor Conditions	Healthy, 1-,2-,3-bar defects
Load Levels and approximate torque (N•m)	Minimum, medium, full 0.796, 0.810, 0.830
f_R **(@ 50 Hz)**	49.6 Hz, 48.7 Hz, 47.6 Hz
N	163,840
f_s **(Current)**	16,384 Hz

6.6 Results

Fig. 6.9 and Fig. 6.10 illustrate representative processing results from one phase of the current at 50 Hz, depicting features of a motor with three broken rotor bars (3B) and a healthy motor (H1), under minimum and full load, respectively; the results are around f_L and the corresponding 5th and 7th harmonics. The arrows indicate the predicted fault characteristic frequencies, as per Eq. (3.5)-(3.6), Eq. (3.8)-(3.9), and Eq. (3.10). The red dashed line indicates the estimated noise floor, as per Eq. (3.29).

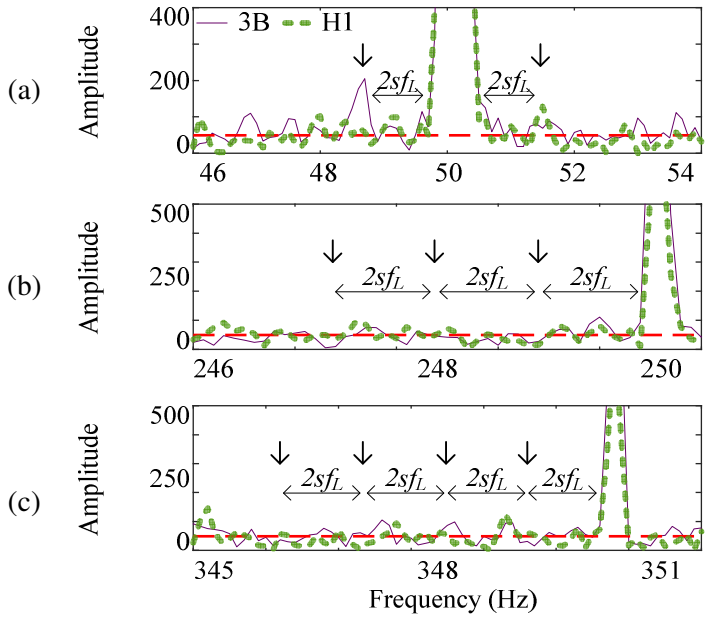

Fig. 6.9. Current results at 50 Hz under a minimum load condition for an IM with three broken rotor bars (purple, solid), and a healthy motor (green, dashed) at: (a) fundamental line frequency; (b) 5th harmonic; (c) 7th harmonic.

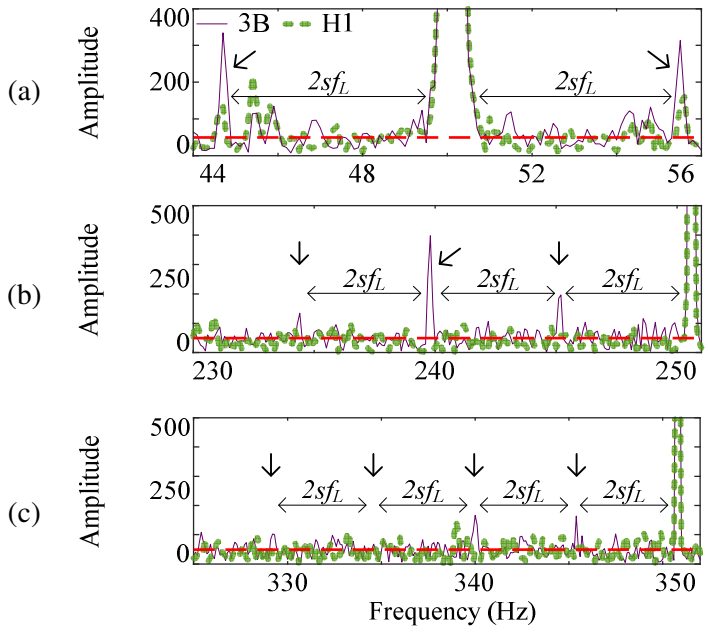

Fig. 6.10. Current results at 50 Hz under a full load condition for an IM with three broken rotor bars (purple, solid), and a healthy motor (green, dashed) at: (a) fundamental line frequency; (b) 5th harmonic; (c) 7th harmonic.

6.7 Results Discussion

It can be observed from Fig. 6.9 and Fig. 6.10 that the fault features are clearer under a full-load but become less clear under a minimum load condition. Possible reasons for such unclear fault feature extraction may be due to the following:

1) The means to introduce the fault as shown in Fig. 6.7 may not be correct. The holes at the end caps may not fully disrupt the current flow in a similar manner to a broken rotor bar. Subsequent investigations revealed that most other literature on broken rotor bars show the fault introduced based on directly drilling through the rotors [38,39,41] as shown in Fig. 4.6.
2) It was assumed that the full load was simply based solely on the full-load nameplate shaft speed. However, due to the connected load, the motor was subsequently found to have reached its full load condition based on the measurement of the average 3-phase RMS current, prior to reaching the full-load nameplate shaft speed [79]. Hence, these tests introduced possible defects related to an overloaded condition, which may skew fault feature extraction results.
3) There were limited considerations on the choice of sensor and signal conditioning to attain a higher SNR. As a result, potential fault features may have been buried in noise, reducing the clarity of the fault feature extraction.

Due to the aforementioned factors, the results of this initial investigation were not used in this work. However, issues related to the creation of the rotor bar faults, preventing overloaded conditions, and achieving an appropriate SNR were subsequently corrected as a consequence of this investigation.

REFERENCES

[1] N. Tesla, "A new system of alternate current motors and transformers," *Transactions of the American Institute of Electrical Engineers*, vol. 5, no. 10, pp. 308-327, July 1888.

[2] M. Zeraoulia, M.E.H. Benbouzid, and D. Diallo, "Electric motor drive selection issues for HEV propulsion systems: a comparative study," *IEEE Transactions on Vehicular Technology*, vol. 55, no. 6, pp. 1756-1764, Nov. 2006.

[3] P. Waide and C.U. Brunner, "Energy-efficiency policy opportunities for electric motor-drive systems," International Energy Agency, Paris, France, Working Paper 2011.

[4] R. Saidur, "A review on electrical motors energy use and energy savings," *Renewable and Sustainable Energy Reviews*, vol. 14, no. 3, pp. 877-898, 2010.

[5] M.F. Cabanas, F. Pedrayes, C.H. Rojas, M.G. Melero, J.G. Norniella, G.A. Orcajo, J.M. Cano, F. Nuño, and D.R. Fuentes, "A new portable, self-powered, and wireless instrument for early detection of broken rotor bars in induction motors," *IEEE Transactions on Industrial Electronics*, vol. 58, no. 10, pp. 4917-4930, Oct. 2011.

[6] H. Kim, S.B. Lee, S. Park, S.H. Kia, and G. Capolino, "Reliable detection of rotor faults under the influence of low-frequency load torque oscillations for applications with speed reduction coupling," *IEEE Transactions on Industry Applications*, vol. 52, no. 2, pp. 1460-1468, Mar./Apr. 2016.

[7] Siemens. (2019) "Grinding to the core – with pinion mill drives". [Online]. https://new.siemens.com/global/en/markets/mining-industry/mining-beneficiation/horizontal-mill-pinion-drives.html

[8] R.B. Randall, *Vibration-based Condition Monitoring*. United Kingdom: Wiley, 2011.

[9] P. Tavner, L. Ran, J. Penman, and H. Sedding, *Condition Monitoring of Rotating Electrical Machines*. United Kingdom: The Institution of Engineering and Technology, 2008.

[10] W. Wang, "An intelligent system for machinery condition monitoring," *IEEE Transactions on Fuzzy Systems*, vol. 16, no. 1, pp. 110-122, Feb. 2008.

[11] (2019) "Induction Motor - Types & Advantages," Electronics | Projects | Focus. [Online]. https://www.elprocus.com/induction-motor-types-advantages/

[12] Electric4U. (2019, July) "Induction Motor: Working Principle, Types, & Definition," Electric 4 U. [Online]. https://www.electrical4u.com/induction-motor-types-of-induction-motor/

[13] pnpntransistor. (2018, Oct.) "Slip ring Induction Motor Fundamentals," PnPn Transistor. [Online]. https://pnpntransistor.com/slip-ring-induction-motor/

[14] A. Huges and B. Drury, *Electric Motors and Drives: Fundamentals, Types, and Applications*, 4th ed. Massachusetts, USA: Newnes, 2013.

[15] J.H. Huijsing, "Smart sensor systems: why? where? how?," in *Smart Sensor Systems*, G.C.M. Meijer, Ed. U.K.: John Wiley & Sons Ltd., 2008, pp. 1-21.

[16] F.J.A. Cardoso, S.P.S. Faria, and J.E.G. Oliveira, "A smart sensor for the condition

monitoring of industrial rotating machinery," in *Proceedings of IEEE Sensors*, Taipei, Taiwan, 2012, pp. 1-4.
[17] F. Philipp, J. Martinez, M. Glesner, and A. Arkkio, "A smart wireless sensor for the diagnosis of broken bars in induction motors," in *Proceedings of the 2012 13th Biennial Baltic Electronics Conference*, Tallinn, Estonia, 2012, pp. 119-122.
[18] E.T. Esfahani, S. Wang, and V. Sundararajan, "Multisensor wireless system for eccentricity and bearing fault detection in induction motors," *IEEE Transactions on Mechatronics*, vol. 19, no. 3, pp. 818-826, June 2014.
[19] M.G. S. and V. Hedge, "Application of MEMS accelerometer for detection and diagnosis of multiple faults in the roller element bearings of three phase induction motor," *IEEE Sensors Journal*, vol. 16, no. 1, pp. 145-152, Jan. 2016.
[20] MOTOR RELIABILITY WORKING GROUP, "Report of large motor reliability survey of industrial and commercial installations, part I," *IEEE Transactions on Industry Applications*, vol. IA-21, no. 4, pp. 853-864, Jul./Aug. 1985.
[21] P.F. Albrecht, J.C. Appiarius, R.M. McCoy, E.L. Owen, and D.K. Sharma, "Assessment of reliability of motors in utility applications," *IEEE Transactions on Energy Conversion*, vol. EC-1, no. 1, pp. 39-46, Mar. 1986.
[22] O.V. Thorsen and M. Dalva, "Failure identification and analysis for high voltage induction motors in petrochemical industry," *IEEE Transactions on Industry Applications*, vol. 31, no. 5, pp. 1186-1196, Sept./Oct. 1995.
[23] O.V. Thorsen and M. Dalva, "A survey of faults on induction motors in offshore oil industry petrochemical industry, gas terminals, and oil refineries," *IEEE Transactions on Industry Applications*, vol. 35, no. 4, pp. 810-818, Jul./Aug. 1999.
[24] A.H. Bonnett and G.C. Soukup, "Rotor failures in squirrel cage induction motors," *IEEE Transactions on Industry Applications*, vol. IA-22, no. 6, pp. 1165-1173, Nov./Dec. 1986.
[25] A.H. Bonnett and T. Albers, "Squirrel-cage rotor options for AC induction motors," *IEEE Transactions on Industry Applications*, vol. 37, no. 4, pp. 1197-1209, Jul./Aug. 2001.
[26] M.E.H. Benbouzid and G.B. Kliman, "What stator current processing-based technique to use for induction motor rotor faults diagnosis?," *IEEE Transactions on Energy Conversion*, vol. 18, no. 2, pp. 238-244, June 2003.
[27] S. Nandi, H.A. Toliya, and X. Li, "Condition monitoring and fault diagnosis of electric motors - a review," *IEEE Transactions on Energy Conversion*, vol. 20, no. 4, pp. 719-729, Dec. 2005.
[28] G.B. Kliman and R.A. Koegl, "Noninvasive detection of broken rotor bars in operating induction motors," *IEEE Transactions on Energy Conversion*, vol. 3, no. 4, pp. 873-879, Dec. 1988.
[29] X. Ying, "Performance evaluation and thermal fields analysis of induction motor with broken rotor bars located at different relative positions," *IEEE Transactions on Magnetics*, vol. 46, no. 5, pp. 1243-1250, May 2010.
[30] N.K. Verma, R.K. Sevakula, S. Dixit, and A. Salour, "Intelligent condition based monitoring using acoustic signals for air compressors," *IEEE Transactions on*

Reliability, vol. 65, no. 1, pp. 291-309, Mar. 2016.
[31] W. Sui, S. Osman, and W. Wang, "An adaptive envelope spectrum technique for bearing fault detection," *Measurement Science and Technology*, vol. 25, pp. 1-9, July 2014.
[32] W. Zhou, T.G. Habetler, and R.G. Harley, "Bearing condition monitoring methods for electric machines: a general review," in *Proceedings of the 2007 IEEE Symposium on Diagnostics for Electric Machines, Power Electronics and Drives*, Cracow, Poland, 2007, pp. 3-6.
[33] C. Morales-Perez, J. Rangel-Magdaleno, H. Peregrina-Barreto, J.P. Amezquita-Sanchez, and M. Valtierra-Rodriguez, "Incipient broken rotor bar detection in induction motors using vibration signals and the orthogonal matching pursuit algorithm," *IEEE Transactions on Instrumentation and Measurement*, vol. 67, no. 9, pp. 2058-2068, Sept. 2018.
[34] J. Kim, S. Shin, S.B. Lee, K.N. Gyftakis, M. Drif, and A.J.M. Cardoso, "Power spectrum-based detection of induction motor rotor faults for immunity to false alarms," *IEEE Transactions on Energy Conversion*, vol. 30, no. 3, pp. 1123-1132, Sept. 2015.
[35] G.B. Kliman and J. Stein, "Methods of motor current signature analysis," *Electric Machines and Power Systems*, vol. 20, no. 5, pp. 463-474, Sep. 1992.
[36] D.Z. Li, W. Wang, and F. Ismail, "A Spectrum Synch Technique for Induction Motor Health Condition Monitoring," *IEEE Transactions on Energy Conversion*, vol. 30, no. 4, pp. 1348-1355, Dec. 2015.
[37] F. Filippetti, G. Franceschini, and C. Tassoni, "AI techniques in induction machines diagnosis including the speed ripple effect," *IEEE Transactions on Industry Applications*, vol. 34, no. 1, pp. 98-108, Jan./Feb. 1998.
[38] A. Naha, A.K. Samanta, A. Routray, and A.K. Deb, "A method for detect half-broken rotor bar in lightly loaded induction motors using current," *IEEE Transactions on Instrumentation and Measurement*, vol. 65, no. 7, pp. 1614-1625, July 2016.
[39] R.A. Lizarraga-Morales, C. Rodriguez-Donate, E. Cabal-Yepez, M. Lopez-Ramirez, L.M. Ledesma-Carrillo, and E.R. Ferrucho-Alvarez, "Novel FPGA-based methodology for early broken rotor bar detection and classification through homogeneuity estimation," *IEEE Transactions on Instrumentation and Measurement*, vol. 66, no. 7, pp. 1760-1769, July 2017.
[40] D. Morinigo-Sotelo, R.J. Romero-Troncoso, P.A. Panagiotou, J.A. Antonio-Daviu, and K.N. Gyftakis, "Reliable detection of rotor bars breakage in induction motors via MUSIC and ZSC," *IEEE Transactions on Industry Applications*, vol. 54, no. 2, pp. 1224-1234, Mar./Apr. 2018.
[41] D. Matic, F. Kulic, M. Pineda-Sánchez, and I. Kamenko, "Support vector machine classifier for diagnosis in electrical machines: Application to broken bar," *Expert Systems with Applications*, vol. 39, pp. 8681-8689, 2012.
[42] A. Moosavian, H. Ahmadi, A. Tabatabaeefar, and M. Khazaee, "Comparison of two classifiers; K-nearest neighbor and artificial neural network, for fault diagnosis

on a main engine journal-bearing," *Shock and Vibration*, vol. 20, pp. 263-272, 2013.
[43] R.J. Romero-Troncoso, R. Saucedo-Gallaga, E. Cabal-Yepez, A. Garcia-Perez, R.A. Osornio-Rios, R. Alvarez-Salas, H. Miranda-Vidales, and N. Huber, "FPGA-based online detection of multiple combined faults in induction motors through information entropy and fuzzy inference," *IEEE Transactions on Industrial Electronics*, vol. 58, no. 11, pp. 5263-5270, Nov. 2011.
[44] J.R. Jang, "ANFIS: Adaptive-network-based fuzzy inference system," *IEEE Transactions on Systems, Man, and Cybernetics*, vol. 23, no. 3, pp. 665-685, May/Jun. 1993.
[45] I. Attoui, N. Boutasseta, N. Fergani, B. Oudjani, and A. Deliou, "Vibration-based bearing fault diagnosis by an integrated DWT-FFT approach and an adaptive neuro-fuzzy inference system," in *Proceedings of the 2015 3rd International Conference on Control, Engineering & Information Technology*, Tlemcen, Algeria, 2015, pp. 1-6.
[46] F.O. Karray, and C. de Silva, *Soft Computing and Intelligent Systems Design*. Essex, England: Pearson Education Limited, 2004.
[47] T. Gupta. (2017) "Deep learning: overfitting", Towards Data Science. [Online]. https://towardsdatascience.com/deep-learning-overfitting-846bf5b35e24
[48] P. Angelov, X. Zhou, and F. Klawonn, "Evolving fuzzy rule-based classifiers," in *Proceedings of the 2007 IEEE Symposium on Computational Intelligence in Image and Signal Processing*, Honolulu, USA, 2007.
[49] P. Angelov, "An approach for fuzzy rule-base adaptation using on-line clustering," *International Journal of Approximate Reasoning*, no. 35, pp. 275-289, Mar. 2004.
[50] P.P. Angelov and X. Zhou, "Evolving fuzzy-rule-based classifiers from data streams," *IEEE Transactions on Fuzzy Systems*, vol. 16, no. 6, pp. 1462-1475, Dec. 2008.
[51] O.A. Jianu, "An Evolving Neural Fuzzy Classifier for Machinery Diagnostics," Lakehead University, Thunder Bay, Ontario, Canada, M. Sc. Thesis. 2010.
[52] W. Wang and J. Vrbanek Jr., "An evolving fuzzy predictor for industrial applications," *IEEE Transcations on Fuzzy Systems*, vol. 16, no. 6, pp. 1439-1449, Dec. 2008.
[53] Y. Lu, R. Xie, and S.Y. Liang, "Bearing fault diagnosis with nonlinear adaptive dictionary learning," *The International Journal of Advanced Manufacturing Technology*, pp. 1-13, Mar. 2019.
[54] L.A. Trujillo-Guarjardo, J. Rodriguez-Maldonado, M.A. Moonem, and M.A. Platas-Garza, "A multiresolution Taylor–Kalman approach for broken rotor bar detection in cage induction motors," *IEEE Transactions on Instrumentation and Measurement*, vol. 67, no. 6, pp. 1317-1328, June 2018.
[55] Nidec Copal Electronics Corporation. (2019) Series: AC current sensors C-CT (All series). [Online]. https://www.nidec-copal-electronics.com/e/product/list/009001/
[56] STMicroelectronics. (2019) LIS3DH. [Online]. https://www.st.com/content/st_com/en/products/mems-and-

sensors/accelerometers/lis3dh.html
[57] W. Kester, W. Jung, and J. Bryant, "Op Amp Specifications," in *Op Amp Applications Handbook*, W. Jung, Ed. Massachusetts: Newnes / Elsevier, 2005, ch. 1.4, pp. 51-88.
[58] (2014) "Equivalent Noise Bandwidth," IntgCkts: A RFIC designer's notes. [Online]. http://analog.intgckts.com/equivalent-noise-bandwidth/2014
[59] Microchip. (2019) ATmega328P. [Online]. https://www.microchip.com/wwwproducts/en/ATmega328p
[60] Microchip. (2019) 23LC1024: 2.5-5.5V 1Mb SPI Serial SRAM. [Online]. https://www.microchip.com/wwwproducts/en/23LC1024
[61] Anaren. (2019) Wireless Transceivers: Air for Proprietary RF. [Online]. https://www.anaren.com/catalog/wireless-transceivers/proprietary-rf
[62] Government of Canada. (2018) Canadian Table of Frequency Allocations. [Online]. http://www.ic.gc.ca/eic/site/smt-gst.nsf/eng/sf10759.html
[63] D. Berenguer. (2014) Simple Wireless Abstract Protocol. [Online]. https://github.com/panStamp/panstamp/wiki/Simple%20Wireless%20Abstract%20Protocol
[64] A. On. (2018) "Difference between I2C and SPI (I2C vs SPI), you should know," Aticleworld. [Online]. https://aticleworld.com/difference-between-i2c-and-spi/
[65] Future Technology Devices International Ltd. (2019) FT231X – Full Speed USB to Full Handshake UART. [Online]. https://www.ftdichip.com/Products/ICs/FT231X.html
[66] "High-Speed DSP Systems Design," Texas Instruments, Literature Number: SPRU889, 2005.
[67] O. Lathrop. (2011) "Decoupling caps, PCB Layout," StackExchange - Electrical Engineering. [Online]. https://electronics.stackexchange.com/a/15143/40812
[68] "PCB Design Guidelines For Reduced EMI," Texas Instruments, Literature Number: SZZA009, 1999.
[69] (2017) "TechTip: Digital I/O Techniques," Measurement Computing. [Online]. https://www.mccdaq.com/TechTips/TechTip-2.aspx
[70] "An overview of oscillator jitter," Statek Corporation, California, USA., Technical Note 35, 2006.
[71] R. Cerda, "Pierce-Gate crystal oscillator, an introduction," *Microwave Product Digest*, pp. 1-3, Mar. 2008.
[72] S. Thornton. (2017) "Watchdog Timer: what is it?," Microcontroller Tips. [Online]. https://www.microcontrollertips.com/whats-watch-dog-timer-wdt-faq/
[73] (2015) "Harmonics," Electronics Tutorials. [Online]. https://www.electronics-tutorials.ws/accircuits/harmonics.html
[74] K. Vasuvedan, G.R. Rao, and P.S. Rao. (2009) "Harmonics in induction machines", NPTEL: Electrical Engineering - Electrical Machines II (IIT Madras). [Online]. http://nptel.ac.in/courses/108106072/9
[75] N.E. Huang, Z. Shen, S.R. Long, H.H. Shih, Q. Zheng, N. Yen, C.C. Tung, and H.H. Liu, "The empirical mode decomposition and the Hilbert spectrum for

nonlinear and non-stationary time series analysis," *Proceedings of the Royal Society of London. Series A, Mathematical and Physical Sciences*, vol. 454, pp. 903-995, 1998.
[76] B. Boashash, "Estimating and interpreting the instantaneous frequency of a signal," *Proceedings of the IEEE*, vol. 80, no. 4, pp. 520-538, Apr. 1992.
[77] A.D. Poularikas, "The Hilbert Transform," in *The Handbook of Formulas and Tables for Signal Processing*, A.D. Poularikas, Ed.: CRC Press, 1999, ch. 15.
[78] S.L. Marple Jr., "Computing the discrete-time "analytic" signal via FFT," *IEEE Transactions on Signal Processing*, vol. 47, no. 9, pp. 2600-2603, Sep. 1999.
[79] "Determining electric motor load and efficiency," US Department of Energy, 1997.
[80] (2019) "Quanser Q4," Quanser Real-Time Control (QUARC). [Online]. http://quanser-update.azurewebsites.net/quarc/documentation/q4.html
[81] (2019) "MODEL: 603C01", PCB Piezotronics. [Online]. https://www.pcb.com/products?m=603C01
[82] J. Faiz, B.M. Ebrahimi, H.A. Toliyat, and W.S. Abu-Elhaija, "Mixed-fault diagnosis in induction motors considering varying load and broken bars location," *Energy Conversion and Management*, vol. 51, pp. 1432-1441, 2010.
[83] N. Halem, S.E. Zouzou, K. Srairi, and S. Guedidi, "Influence of broken rotor bars location in the squirrel cage induction motor using finite element method," *Journal of Fundamental and Applied Sciences*, vol. 5, no. 1, pp. 110-119, June 2013.
[84] J. Vrbanek Jr, "Evolving Neuro-Fuzzy Tools for System Classification and Prediction," Lakehead University, Thunder Bay, Ontario, Canada, M. Sc. Thesis. 2008.
[85] X. Zhou and P. Angelov, "Evolving fuzzy systems from data streams in real-time," in *Proceedings of the 2006 International Symposium on Evolving Fuzzy Systems*, Ambleside, UK, 2006.
[86] J.R. Jang, C. Sun, and E. Mizutani, *Neuro-Fuzzy and Soft Computing: A Computational Approach to Learning and Machine Intelligence*. New Jersey, USA: Prentice-Hall, Inc., 1997.
[87] J. Hadrien. (2018) Deep Learning Book Series · 2.9 The Moore Penrose Pseudoinverse. [Online]. https://hadrienj.github.io/posts/Deep-Learning-Book-Series-2.9-The-Moore-Penrose-Pseudoinverse/
[88] D. Dua and C. Graff. (2019) "UCI Machine Learning Repository," University of California, School of Information and Computer Science. [Online]. http://archive.ics.uci.edu/ml
[89] W. Wang, D.Z. Li, and J. Vrbanek, "An evolving neuro-fuzzy technique for system state forecasting," *Neurocomputing*, vol. 87, pp. 111-119, 2012.
[90] O. Jianu and W. Wang, "A self-evolving fuzzy classifier for gear fault diagnosis," *International Journal of Mechanical & Mechatronics Engineering*, vol. 14, no. 5, pp. 90-96, Oct. 2014.
[91] L. Bassi, "Industry 4.0: hope, hype or revolution?," in *Proceedings of the 2017 IEEE 3rd International Forum on Research and Technologies for Society and Industry (RTSI)*, Modena, Italy, 2017, pp. 1-5.

[92] "MS/TP Communications Bus Technical Bulletin," Johnson Controls International, Technical Bulletin LIT-12011034, 2018.
[93] (2006) "Microcontroller Brown-out detection," ScienceProg. [Online]. https://scienceprog.com/microcontroller-brown-out-detection/
[94] R.C. Hendriks, J. Jensen, and R. Heusdens, "Noise tracking using DFT domain subspace decompositions," *IEEE Transactions on Audio, Speech, and Language Processing*, vol. 16, no. 3, pp. 541-553, Mar. 2008.
[95] (2019) KiCad EDA, A Cross Platform and Open Source Electronics Design Automation Suite. [Online]. http://kicad-pcb.org/
[96] (2019) Bantam Tools Desktop Milling Machines. [Online]. https://www.bantamtools.com/
[97] (2017) Qingdao University Sunbest Technology Co. Ltd. [Online]. http://www.sbkj.net/, https://cn.kompass.com/c/qingdao-university-sunbest-technology-co-ltd/cn222069/
[98] (2013) eMech Systems Inc. [Online]. http://emechsys.com/
[99] (2019) Arduino. [Online]. https://www.arduino.cc/en/Main/Software

This page is intentionally left blank.